Spring 4-14-2019

Direct numerical simulation of incompressible spatially developing turbulent mixing layers

Juan Diego Colmenares Fernandez
Doctoral Student, Mechanical Engineering

Juan Diego Colmenares Fernández

Candidate

Mechanical Engineering

Department

This dissertation is approved, and it is acceptable in quality and form for publication:

Approved by the Dissertation Committee:

Dr. Svetlana V. Poroseva, Chair

Prof. Peter Vorobieff

Prof. C. Randall Truman

Prof. Edl Schamiloglu

Direct numerical simulation of incompressible spatially developing turbulent mixing layers

by

Juan D. Colmenares F.

B.S., Mechanical Engineering, Universidad de los Andes, 2012
M.S., Mechanical Engineering, Universidad de los Andes, 2014

DISSERTATION

Submitted in Partial Fulfillment of the
Requirements for the Degree of

Doctor of Philosophy
Engineering

The University of New Mexico

Albuquerque, New Mexico

May, 2019

Dedication

To my parents, who inspire me to achieve great things.

To my wife and my daughter, who make my life so wonderful.

Acknowledgments

I would like to thank my advisor, Dr. Svetlana V. Poroseva, for the opportunity to work with her and for being an example of academic and professional excellence.

Thanks to Dr. Scott Murman for his feedback on this work and for providing access to the NASA's supercomputers. Thanks to our collaborator Dr. Yulia Peet and to her students, Philip Sakievich and Tanmoy Chatterjee, for providing insightful input which made this work possible.

Special thanks to the committee members, Prof. Peter Vorobieff, Prof. Randy Truman and Prof. Edl Schamiloglu, for taking the time to be in my committee and for your support.

Thanks to the NASA High-End Computing Program for providing HPC resources and to Intelligent Light for providing academic license for the Fieldview visualization software.

Thanks to Prof. Paul Fischer, Prof. Philipp Schlatter and Dr. Ricardo Vinuesa for answering my questions about the code Nek5000.

I would like to thank my parents for their support at every stage of my education, which made this achievement possible. Thanks to my brother for all he has done for the family. Finally, I would like to thank my wife for supporting me throughout this process and for her love.

Direct numerical simulation of incompressible spatially developing turbulent mixing layers

by

Juan D. Colmenares F.

B.S., Mechanical Engineering, Universidad de los Andes, 2012
M.S., Mechanical Engineering, Universidad de los Andes, 2014

Ph.D., Engineering, University of New Mexico, 2019

Abstract

Turbulent mixing layers are a canonical free shear flow in which two parallel fluid streams of different velocities mix at their interface. Understanding spatial development of a turbulent mixing layer is essential for various engineering applications. However, multiple factors affect physics of this flow, making it difficult to reproduce results in experiments and simulations. The current study investigates sensitivity of direct numerical simulation (DNS) of such a flow to computational parameters. In particular, effects of the computational domain dimensions, grid refinement, thickness of the splitter plate, and the laminar boundary layer characteristics at the splitter plate trailing edge are considered. Flow conditions used in DNS are close to those from the experiments by Bell & Mehta (1990), where untripped boundary layers co-flowing on both sides of a splitter plate mix downstream of the plate. No artificial perturbations are used in simulations to trigger the flow transition to turbulence. DNS were conducted using the spectral-element method implemented in

the open-source code Nek5000. Mean flow statistics are presented for the spatially developing self-similar flow, including high-order velocity moments. Such statistics will be used for validation of high-order Reynolds-Averaged Navier-Stokes (RANS) closure models.

Contents

List of Figures

List of Tables

Glossary

h	Trailing edge thickness.
h_i^N	N-th order Legendre interpolant.
K, K_x, K_y, K_z	Integral of turbulent kinetic energy across the mixing layer and contributions from velocity components in each direction.
N	Polynomial order of Legendre interpolants.
U_1, U_2	High-speed and low-speed free-stream velocities respectively.
$\boldsymbol{U}$	Instantaneous velocity vector field.
$\tilde{\boldsymbol{U}}$	Velocity vector field in initial-boundary value problem.
U, V, W	Streamwise, transverse and spanwise components of instantaneous velocity.
u, v, w	Streamwise, transverse and spanwise components of velocity fluctuations.
u_{rms}	Root-mean square of velocity fluctuations.
$\boldsymbol{x}$	Position vector.
x, y, z	Streamwise, transverse and spanwise coordinates.
Re	Reynolds number.

ΔU	Velocity difference
$\Delta x, \Delta y, \Delta z$	Spectral element size in streamwise, transverse and spanwise directions.
$\Delta_x, \Delta_y, \Delta_z$	Average grid spacing based on quadrature points.
$\Delta t, \Delta s$	Time step size.
δ_1, δ_2	High-speed and low-speed boundary layer thicknesses respectively.
δ_{ML}	Mixing layer thickness from best-fit to error function profile.
δ_ω	Vorticity thickness.
η	Normalized transverse coordinate.
η_K	Kolmogorov length scale
ε	Viscous dissipation of turbulent kinetic energy
ν	Kinematic viscosity
θ^{BL}	Boundary layer momentum thickness.
θ	Mixing layer momentum thickness.
$\langle ... \rangle_E$	Ensemble average.
$\langle ... \rangle$	Ensemble and spanwise average.
$\langle ... \rangle_V$	Volume average.

Chapter 1

Introduction

1.1 Motivation

Free shear flows develop away from boundaries or walls, where mean velocity gradients occur [64]. One type of free shear flows is a mixing layer, which occurs at the interface of two parallel fluid streams that have different free-stream velocities.

In most applications, the two streams that form the mixing layer are initially separated by an impermeable body, for example, a flat plate. A schematic of this configuration is shown in Figure. 1.1, where U_1 and U_2 are the free-stream velocities, x is the streamwise direction, y is the transverse direction and z is the spanwise direction. Boundary layer velocity profiles have developed on each side of the plate. Downstream of the trailing edge of the plate, waves of Kelvin-Helmholtz instabilities appear due to the velocity difference between the free-streams [20, 32]. Large vortex structures of spanwise vorticity, or vortex roll-ups, form from the initial instabilities which interact and grow in diameter as more non-rotating fluid from the free-streams is entrained or engulfed into the mixing layer, causing the mixing layer thicknes, δ, to grow with streamwise location. Such vortex structures are present in both laminar and turbulent flow, and persist at high Reynolds numbers. Figure 1.2 shows a shadowgraph image of a turbulent mixing layer, where one can observe the small-

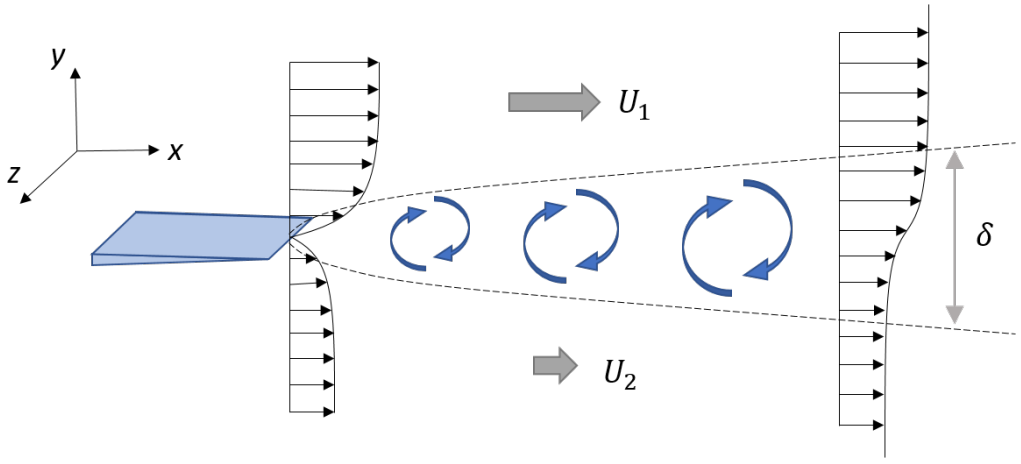

Figure 1.1: Schematic of a typical mixing layer configuration.

scale turbulent structures riding the large-scale vortex structures.

Turbulent mixing layers are present in many engineering applications, where they play a crucial role in the transport of momentum, heat and chemical species. They occur inside spark ignition engines [2, 46], where the mixing of air and fuel in the shear layer affects the rate of combustion and overall efficiency. In the design of gas turbines, understanding the flow dynamics and heat release in the mixing layer is one of the main challenges for controlling the combustion process [44].

The level of noise produced at the nozzle of turbine engines in commercial aircraft has been linked to the level of turbulent kinetic energy in the shear layer formed by exhaust gases [84]. To reduce noise, it is necessary to control the turbulence characteristics in the mixing layer, which requires deep understanding the flow dynamics.

Mixing layers are also formed at the wake of wind turbines, where they interact with other turbines downstream, affecting the performance of the wind farm [8].

Because of the important role that mixing layers play in such applications, increasing the knowledge about the dynamics of turbulent mixing layers would potentially benefit the aeronautical, aerospace, automotive and energy industries by allowing engineers to improve the efficiency of combustion processes in engines and turbines, reduce noise from turbine engines and increase power output from wind farms.

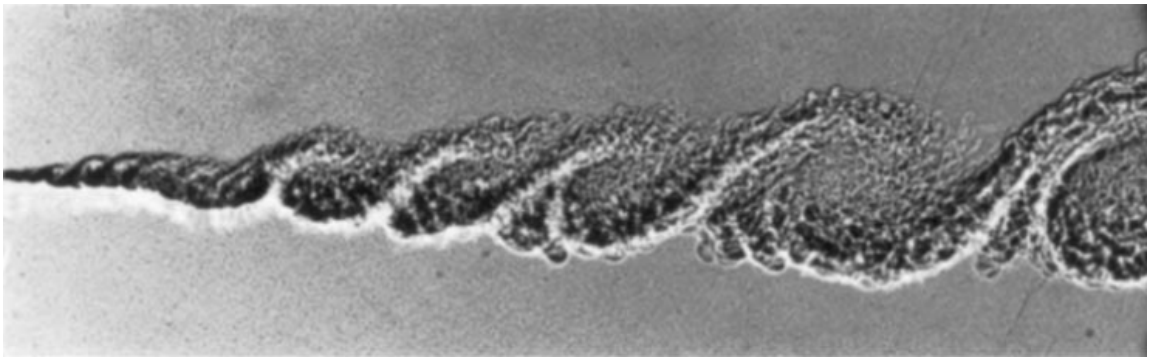

Figure 1.2: Shadowgraph image of vortex structures in turbulent mixing layers [17].

Turbulent mixing layers have been studied for more than half of a century [42]. However, the seemingly "simple" flow encompasses many complex physical processes which make it difficult to fully understand and predict the characteristics of the mean flow and turbulence statistics.

The focus of the current work is to understand physics of an incompressible spatially developing turbulent mixing layer flow, by using direct numerical simulations to provide detailed description of mean flow statistics. The following section provides a review of the state of art in the study of turbulent mixing layers.

1.2 State of the Art

In this section, a review of literature related to turbulent mixing layers is presented. The scope of the review is limited to studies of incompressible flows. Experimental results for such flows are reviewed first, followed by a review of numerical studies on the subject.

Experiments

Liepmann & Laufer [42] were among the first to measure the turbulence statistics in mixing layers, including mean velocity, velocity moments and turbulent kinetic energy balance, using hot-wire anemometry. Their results allowed to question the validity of turbulence models based on the assumption of a constant "mixing length" proposed by Prandtl [66], which had been used successfully to predict mean velocity distribution in different turbulent flows, since the experiment showed that the mixing length varied across the mixing layer. This highlighted the need for models based on turbulent fluctuations and their correlations, in order to capture the physics of the flow. In Wygnanski & Fiedler [82], mean velocity field and velocity moments up to fourth order were measured for a single-stream mixing layer ($U_1 > 0$, $U_2 = 0$) using improved hot-wire techniques. While the results shed some light on the validity of simple concepts, such as eddy viscosity and eddy diffusivity, data for velocity moments was only available at limited streamwise locations and was far from providing a full picture of the mean flow. Later studies have published profiles for third-order moments (Bell & Mehta [10]) and fourth-order moments (Delville *et al.* [22]), with such data often used as reference for developing and validating turbulence models [1]. These datasets, however, also fail to provide full and accurate description of the flow: only one third-order velocity moment is given in [10], while data in [22] is available at limited streamwise locations.

Turbulence statistics provide significant information about the mean flow characteristics. However, it is also important to understand the instantaneous behavior of the mixing layer. The seminal work by Brown & Roshko [17] was the first to identify coherent large-scale vortical structures of spanwise vorticity in the turbulent mixing layer using flow visualization techniques. The images showed that large-scale vortices, formed from the "roll-up" of initial Kelvin-Helmholtz instability waves predicted by linear stability analysis [53, 56, 32], persisted at high Reynolds numbers, where small-scale turbulent fluctuations would ride the large-scale coherent structures. Experiments at moderate Reynolds numbers conducted by Winant

& Browand [81] found that the coherent structures interacted in a "pairing" process in which neighboring vortices merged to form a single vortex of larger diameter. The "vortex pairing" was deemed by the authors to be the driving mechanism of growth of the mixing layer. A later study conducted by Konrad [37] would find that the entrainment process in mixing layers –the process through which surrounding non-rotating fluid is captured by the shear layer– occurs due to non-turbulent fluid becoming engulfed by the large-scale structures, confirming that the spreading of the shear layer is driven by the action of the large-scale vortices. However, the development of the mixing layer, in particular the transition to turbulence and the evolution of turbulence intensities, cannot be explained solely in terms of the spanwise structures.

Miksad [54] discovered the presence of three-dimensional longitudinal (streamwise) vortices which appeared during the non-linear stages of transition in the mixing layer. The structures were studied in depth by Bernal & Roshko [12]. They characterized the secondary instability that generated the streamwise structures and found that the mean normalized wavelength is independent of velocity ratio, density ratio and initial shear-layer profile. It was also found that these vortices appeared in pairs of counter-rotating structures. In a study conducted by Huang & Ho [33] on the small-scale transition in plane mixing layers, the authors argued that random small-scale eddies were produced by the merging interaction between streamwise and spanwise vortices. Therefore, once the flow becomes turbulent the streamwise vorticity decays due to the breakdown of the longitudinal structures into small-scale structures [41].

Different studies have tried to pinpoint the location where transition occurs in the mixing layer using different approaches. Konrad [37] used schlieren images of different gas-phase mixing layers to observe the patterns in the flow, and noted that three-dimensional behavior (appearance of streamwise lines) was generally observed at a local Reynolds number of $Re \sim 10^4$. Later studies used reactive and non-reactive chemicals [15, 38] to determine the level of mixing between the two streams

of the shear layer. Increased mixing of the transported chemicals was attributed to transition to turbulence. This "mixing transition" was found to occur at $Re \approx 10^4$. The same behavior was observed for liquid-phase and gas-phase shear-layers [11]. In experiments where velocity fluctuations where measured [36, 33], the power-law regime in the energy spectrum, with an exponent close to $-5/3$, which is indicative of turbulence, developed in the neighborhood of $3 \times 10^3 < Re < 10^4$. As Dimotakis [27] pointed out in his paper, different investigations support the notion that transition to turbulence occurs in mixing layers at a minimum local Reynolds number of $Re \approx 1 - 2 \times 10^4$.

In post-transition flows, theoretical studies show that at high-enough Reynolds numbers and at a far-enough downstream distance from the splitter plate, the governing equations and boundary conditions of planar turbulent mixing layers yield self-similar solutions [77]. Conditions for self-similarity far from the inlet boundary are that the mean flow and its turbulence statistics become independent of streamwise location when normalized with respect to local length scale, δ, and ΔU, and that shear layer thickness grows linearly with as a function of streamwise coordinate, i.e. $\partial\delta/\partial x = constant$. Even though more rigorous conditions have been proposed to define when a flow has reached self-similarity [18], it is generally accepted that, after a sufficient development distance, all mixing layers achieve a self-similar condition. Therefore, it is convenient to analyze the mean flow statistics of the self-similar flow since they represent the asymptotic behavior of the turbulent mixing layer.

Although mixing layers under different flow conditions share features like the ones mentioned above, there are inconsistencies in measured mean flow statistics from different data sources [17], which were obtained in different experimental setups. This is due to the high sensitivity of the mixing layer flow to inflow conditions, making it difficult to obtain a general characterization of the flow.

The self-similar solution presented by Townsend [77] highlights the importance of velocity ratio between the two free-streams, U_2/U_1, in determining growth rates and maximum levels of turbulence intensity in mixing layers. This has been confirmed

several times through experiments [56, 51, 52]. However, experiments conducted under similar velocity ratios have produced significantly different mixing layer growth rates. For example, the experiments from Liepmann & Laufer [42] and Wygnanski & Fiedler [82], which were conducted for single-stream mixing layers under similar conditoins, yielded significantly different growth rates. The same behavior can be observed for two-stream mixing layers [17].

Flow regime (turbulent or laminar) of the incoming boundary layers at the trailing edge of the splitter plate has been found to have significant effect on mixing layer development. Experiments from Browand & Latigo [16] and Bell & Mehta [10] showed that mixing layers formed from turbulent (tripped) boundary layers tend to grow at slower rates than those formed from laminar (untripped) boundary layers, with normalized turbulence statistics achieving the same form in both cases after a certain streamwise location. In Ref. [10] asymptotic behavior was achieved faster with turbulent inflow conditions than with laminar inflow conditions. Furthermore, the study found that profiles of mean velocity and second-order velocity moments are not sufficient to determine whether the flow had achieved self-similar behavior, since profiles of third-order moments do not achieve asymptotic behavior until later in the flow compared to lower-order statistics. Slessor *et al.* [70] further investigated the effect of inflow conditions in perturbed and unperturbed shear layers using parallel streams of non-reacting and reacting chemicals. Not only did they confirm that even small variations in inflow conditions had an influence on the large-scale structure an development of the flow, which had been previously documented, but also on the level of molecular mixing, i.e. on the small-scale structure of the flow.

Patel [62] studied the effects of free-stream turbulence on free shear flows. He found that turbulence in the free-streams has negligible effect on the flow when it is below 0.6%, but has significant effect at higher intensity levels, particularly on growth rate.

Dziomba & Fiedler [29] found that the influence of trailing-edge thickness, h, on the shear-layer development becomes significant when it exceeds 50% of the sum of

boundary-layer displacement thickness, $\delta_1^* + \delta_2^*$, at the point of separation, where the displacement thickness is defined as:

$$\delta^* = \int_0^\infty (1 - U/U_\infty)\, dy.$$

The most affected flow variable is the location where self-similarity is observed, which is shifted farther downstream as the plate becomes thicker. For plates with thicknesses below the specified threshold, the effect of thickness on the flow development is negligible. Braud *et al.* [14] studied how the splitter plate thickness affects the development of the mixing layer by comparing the flow produced by a thick splitter plate, i.e. $h > 0.5(\delta_1^* + \delta_2^*)$, with a blunt trailing edge and a beveled (thin) trailing edge. In both cases, turbulent inflow conditions were used. They found significant differences in flow structure organization due to the strong effect of the wake from the blunt trailing edge. Therefore, the shape of the splitter plate trailing edge affected flow structure and mixing layer growth rate.

Dimotakis & Brown [28] argue that extent of the experimental apparatus might also affect development of the flow due to a coupling mechanism between large structures by the end of the test section and smaller structures upstream by the action of vorticity. A study conducted by Narayanan & Hussain [58] on forced plane mixing layers supports this idea. They observed feedback-sustained states of large spatial extents which indicate spatial coupling between the Kelvin-Helmholtz instabilities and the downstream pairing processes. Therefore, it is possible that the development of the flow is a global response to inflow/outflow/confinement-geometry conditions [26].

Given the high sensitivity of mixing layers to multiple factors, experimental results are dependent on the experimental apparatus, leading to inconsistencies among in experimental data. Therefore, it is beneficial to study turbulent mixing layers in an environment where the sources of uncertainty could be controlled. This is where numerical simulations, in theory, have an advantage over experiments, since they provide complete control over inflow and boundary conditions, as well as other flow parameters which could be replicated exactly in different simulations.

Numerical Simulations

Numerical simulations of turbulent flows can be categorized into three groups depending on the level of modeling used to represent the turbulent flow field. In Reynolds-Averaged Navier-Stokes (RANS) based models, the transport equation for mean velocity vector and velocity correlations are derived from the governing equations of fluid dynamics, the Navier-Stokes equations. However, such derivation results in a system of infinite number of equations. To have a viable solution to the problem, the system of equations must be "closed" by approximating certain terms. The approximated terms are often accompanied by arbitrary coefficients, which must be fine-tuned for the specific flow being simulated for the approximation to work [64], with most standard models being calibrated for idealized shear flows or boundary layer flows [31, 84]. RANS turbulence models are attractive because the approximation allows to solve the mean flow without having to resolve the smaller scales of motion, thus reducing the computational power required to achieve a solution. Furthermore, if the flow is statistically stationary, a "steady-state" solution can be found using RANS-models without having to solve the unsteady flow. However, because of the high level of approximation, many sources of uncertainty are included in the solution of the mean flow and, therefore, existing RANS-based models cannot be used to provide an accurate prediction of the turbulent mixing layer.

A second approach to simulating turbulent mixing layers is using large-eddy simulations (LES). In LES, a filtering operation is applied to the Navier-Stokes equations to decompose the velocity field into the sum of a filtered component and a residual (or subgrid-scale, SGS) component [64]. The filtered component represents the large-scale motions of the flow, while the SGS component represents the motions with scales smaller than the cutoff length of the applied filter. This procedure introduces a residual-stress tensor (or SGS-stress tensor) into the governing equations, which needs to be modeled. By modeling the small-scale turbulence, the cost is increased compared to RANS-based models, but it is still significantly less than resolving all of the scales of turbulent motions, making it an attractive alternative for researchers.

Large eddy simulations were proposed by Smargorinsky [71] and Lilly [43] to solve the large-scale motions of turbulent flows in meteorological applications. Nevertheless, LES have been applied successfully to a variety of applications including free-shear flows and wall-bounded flows. A collection of works can be found in Ref. [30]. One of the first studies to use LES on a three-dimensional mixing layer was Mansour *et al.* [47]. The authors simulated a temporarily evolving mixing layer, where the flow evolves in time but is statistically homogeneous in the streamwise direction. In such flows, the time coordinate is analogue to the streamwise coordinate in a spatially developing mixing layer, and is generally represented by parallel streams of opposite direction. They were able to reproduce certain features of the flow, like the spanwise vortex structures and the vortex pairing mechanism observed in experiments, showing the applicability of LES for this type of flow. Later studies were also able reproduce streamwise vortices for temporarily evolving mixing layers [19], which are a necessary flow feature to trigger transition to turbulence [33].

As in experiments, numerical solution of mixing layers are also sensitive to initial/inflow conditions. The effect of initial conditions on the development of temporarily evolving mixing layers were studied by Balaras *et al.* [7]. They used two types of initial conditions: shear layer velocity field formed from two flow realizations from turbulent boundary layers with free-streams moving in opposite directions, and imposing a mean velocity profile based on the hyperbolic tangent function with superimposed random perturbations. They found that the development of large-scale structures, was different depending on the initial condition: if strong rollers were formed early (as in the cases initialized by random noise), a well-organized pattern persisted throughout turbulent state. The presence of boundary layer turbulence, on the other hand, inhibited the growth of the inviscid instability, and delayed the formation of the rollerbraid patterns. This difference in flow features was also clear through the mean flow statistics. Flow initialized with superimposed random noise had a slower growth rate than the flow initialized from boundary-layer flow realizations. Turbulence intensities varied as well among simulations.

Similar studies have been conducted for LES of spatially developing mixing layers. Tenaud *et. al* [75] found that the turbulence intensity of superimposed perturbations affected growth rate of the mixing layer. McMullan & Garret [50] used laminar inflow boundary layers with superimposed perturbations as inflow conditions. Two methods were used to impose perturbations: pseudo-random noise imposed as velocity fluctuations and physically correlated perturbations generated using a Recycling-Rescaling method (RRM) [83]. Results showed that even though both methods produced the same profiles of the root-mean-square (r.m.s) of velocity fluctuations at the trailing edge of the splitter plate, the characteristics of the mixing layers produced by such methods were significantly different in terms of the large-scale unsteady vortex structures: inflow conditions with random noise seemed to suppress the formation of streamwise vortices, while the RRM produced well organized streamwise and spanwise vortex structures, with the mean flow being in better agreement with experimental data. The effect of the mean velocity profile imposed as inflow condition was studied by McMullan *et al.* [49]. Results showed that using laminar boundary layers as inflow conditions instead of hyperbolic tangent mean velocity profile was beneficial trigger transition at a streamwise location which agreed with experimental data, which was obtained under similar flow conditions. Therefore, the sensitivity of mixing layers to inflow conditions observed in experiments is also present in numerical simulations, with the added complexity of being dependent on the choice of perturbation method and shape of inflow mean velocity profile.

Large-eddy simulations have also been used to study how the size of the computational domain affects the flow. In their simulations, Balaras *et al.* [7] found that a larger computational box resulted in increased three-dimensionality, represented by spanwise fluctuations, when compared to a smaller box, which suggests that the flow is not independent of domain size. Results from Biancofiore [13] conducted on a spatially developing mixing layer supported this idea, having observed a more "two-dimensional" behavior of the mixing layer in a confined domain, with an almost fully two-dimensional flow observed when the momentum thickness is of the same order of magnitude as the confining scale. A study conducted for a spatially developing

mixing layer [48] analyzed how spanwise domain size affected the development of the flow, and suggested that a minimum ratio between spanwise domain length and mixing layer thickness of $A \equiv L_z/\theta > 10$ is required to obtain results that are independent of spanwise domain size, where L_z is the domain size in spanwise direction and θ is the shear layer momentum thickness. While this criterion is a good starting point for estimating domain sizes for subsequent studies, the study only considered one type of inflow condition and it is not clear how other flow parameters would affect its validity, given the high sensitivity of the flow to inflow conditions.

By definition, the small-scale turbulence is modeled in LES, and therefore, such simulations are not free of model-form uncertainty. A comparative study using different SGS models, done by Vreman *et al.* [79], showed that LES results for mixing layers are model-dependent. Since the accuracy of results depends on *ad hoc* SGS models, it is not possible to make definitive conclusions from this type of simulations. Therefore, to understand the fundamentals of the flow it is important to eliminate model-form uncertainty in simulations, which can only be done through direct numerical simulations.

In direct numerical simulations (DNS) numerical solutions for the Navier-Stokes equations are computed without modeling any terms. These simulations can be considered as "numerical experiments" [55] due to their high level of accuracy in representing the turbulent flows. The main drawback of DNS is its high computational cost, since all the scales of motion in the flow, from smallest to largest, need to be accurately resolved, resulting in very fine grids (solution with high number of degrees of freedom). However, the accuracy of results provide important insight into the flow physics of flows, making it an ideal tool for the fundamental research.

Comte *et al.* [19] conducted DNS of a three-dimensional temporarily developing mixing layer from perturbed laminar initial conditions. The perturbations triggered instabilities which turned into spanwise and streamwise vortices, as observed in experiments. They found that transition happened at the second pairing of vortex structures, in agreement with experimental observations from Huang & Ho [33].

Rogers & Moser conducted an extensive investigation on the roll-up of Kelvin-Helmholtz instabilities [67], transition and pairing process [57] and statistics of fully turbulent, self similar shear layers [68] using temporarily developing mixing layers. Results in Ref. [67] showed that simulations of mixing layers started from laminar initial conditions but with perturbations of different amplitudes and wave numbers produced significantly different flows in terms of the development and growth rate of vortex roll-ups, as well as the three-dimensionality of the flow. Ref. [57], the authors identified several mechanisms of transition in mixing layers. A pairing-induced transition was observed in agreement with experiments from Huang & Ho [33], where small-scale are more significant at the roller core portion of the "rib plane", that is, where spanwise and streamwise vortices interact. Another mechanism occurs when extremely large three-dimensional perturbations are present in the flow, triggering non-linear behavior even before the initial vortex roll-up. In a more recent paper, Rogers & Moser [68] extracted turbulence statistics in a "self-similar" turbulent mixing layer. Because their case was temporarily evolving, they argued that self-similarity was achieved when the normalized profiles of flow statistics, resulting from spanwise and streamwise averaging, became independent of time and when linear growth of the mixing layer thickness in time was observed. The simulations were initialized using two independent realizations from DNS of turbulent boundary layers [72], and joining them at the point where the wall would be, so that the free-streams are moving in opposite directions. Three simulations were conducted: two with two-dimensional disturbances of varying strengths added to the initial boundary layer turbulence, and one without additional disturbances. Profiles of Reynolds stresses from simulation without added disturbances were in good agreement with experimental data from Bell & Mehta [10], while differences between numerical and experimental data became more significant as the strength of the added disturbances was increased. They also calculated budget terms (or balances) for the different Reynolds stresses, which were not previously available. However, their data showed a "breakdown" of self-similarity, meaning that towards the end of the simulation the Reynolds stress profiles were no longer independent of time. The

question arises whether the flow was still in an initial-transient state when statistics where gathered. Furthermore, it is impossible to make a direct comparison between the simulated temporarily evolving flow and the experimental spatially developing flow in terms of the growth rate. For this reason, recent studies have focused on modeling the spatially developing case.

Simulations of a spatially developing mixing layer were conducted by Wang *et al.* [80] from laminar inflow conditions modeled by a hyperbolic tangent mean velocity profile. They used sinusoidal velocity perturbations with a defined range of frequencies to trigger transition to turbulence by exciting the most unstable wavelength from linear stability analysis for the selected inflow profile [53]. They conducted a detailed analysis on coherent small-scale structures by using an axis-tracing method to identify eddies. They found that the large-scale vortex structures did not disappear in the transition process, but were composed by many coherent fine-scale eddies. This study provided significant insight on the anisotropy and energy dissipation rate in the small-scale motions, and was an important step towards showing the feasibility of DNS on spatially developing mixing layers at high enough Reynolds numbers to produce turbulence. The study, however, did not include profiles of Reynolds stresses or other turbulence statistics of the mean flow to assess whether the flow had achieved self-similarity.

Attili & Bisetti [4] conducted simulations using similar inflow conditions as Wang *et al.* [80], but on a much larger domain, reaching high Reynolds numbers that have not been achieved in other DNS studies of mixing layers to this date. They used white-noise velocity perturbations to trigger transition, but did not disclose details on how the white noise was imposed. Flow statistics in their simulations showed evidence of asymptotic behavior, indicative of self-similarity. Profiles of Reynolds stresses and mean velocity were presented, which were in good agreement with experimental data from Bell & Mehta [10] and DNS data from Rogers & Moser [68], but budget terms and higher-order moments were not included in their analysis. Other studies from these authors looked at the fluctuations of a passive scalar in a

turbulent mixing layer [5] and intermittency at the turbulente/non-turbulent edges of the mixing layer [6].

The studies Wang *et al.* [80] and Attili & Bisetti [4] were conducted using modeled inflow conditions (hyperbolic tangent function for mean velocity) which are a useful approximation for the shear flow, but do not resemble how mixing layers occur in experimental setups, making it difficult compare mixing layer development between numerical results and experiments since, as LES studies have shown [49], the shape if incoming flow influences the development of the flow downstream.

Laminar boundary layers separated by a thick splitter plate were used as inflow conditions by Laizet *et al.* [40]. The simulations modeled the trailing edge geometries studied experimentally in Braud *et al.* [14]. Numerical results showed that a thick splitter plate with a blunt trailing edge, as those found in experiments, produce a more three-dimensional mixing layer flow than a plate with thin trailing edge. In an earlier study [39] they had found that the thin trailing edge produced a nominally two-dimensional flow if no perturbations were added, which is why simulations in Ref. [40] used white-noise perturbations to excite the flow. Their simulations, however, were conducted at much lower Reynolds numbers than the referenced experiment [14], thus there was no quantitative comparison of numerical results against experimental data. Self-similarity was not achieved in the simulations.

A recent study by Takamure *et al.* [73] used laminar boundary layers mean velocity profiles as inflow conditions assuming an infinitely thin splitter plate to analyze the driving mechanisms of counter-gradient momentum transport (CGMT) which occurs during during the transition stage due to vortical structures. White-noise velocity perturbations were imposed at the inlet to trigger transition in the mixing layer. Simulations were conducted at lower Reynolds numbers than experiments and previous DNS studies [4, 68, 80]. Mixing layer growh rate and profiles Reynolds stresses showed signs of asymptotic behavior, however, it is not possible to say whether the flow achieved self-similarity since higher-order statistics were not presented. Budget terms from simulations showed that the mechanisms driving CGMT varied depend-

ing on the location in the mixing layer. However, turbulence statistics were not compared against experimental or numerical data available in the literature.

It is important to conduct simulations with flow parameters (velocity ratio, inflow conditions, Reynolds numbers) which are comparable to experimental ones so that direct comparison can be made between experiment and numerical results for validation purposes. However, such simulations are not found in published literature: those that achieve Reynolds numbers comparable to experiments use inflow conditions which neglect the effects of the splitter plate, which Laizet *et al.* [40] showed has significant effect on flow development. Those that use co-flowing boundary layers, like those used in many experiments, were conducted at relatively low Reynolds numbers and statistics were not compared against experiments. Furthermore, all simulations are dependent on the selection of perturbation method which was used to trigger transition, which is usually not described in detail and thus cannot be replicated. Finally, to the best of the author's knowledge, a detailed statistical description of the mixing layer produced by DNS has not been provided since there are no published values for high-order velocity moments and budget terms from a single simulation.

1.3 Objectives

The current work intends to fill a gap in present knowledge by conducting direct numerical simulations of an incompressible turbulent mixing layer which develops from inflow conditions that resemble experimental ones, such as laminar boundary layers separated by a splitter plate, and that can be replicated in later works. Flow parameters were chosen to make the Reynolds numbers in the simulations comparable to those found in the experiments of Bell & Mehta [10].

The main objective of this work is to understand the flow physics of the spatially developing planar turbulent mixing layer. To achieve this goal, a comprehensive statistical description of the flow is provided by gathering data for mean velocity,

Reynolds stresses and budget terms in the transport equation of Reynolds stresses, and present profiles for higher-order moments, making this the first numerical study to present such data for turbulent mixing layers.

For an exact representation of the turbulent flow, an infinite number of velocity moments would be required. Since obtaining an infinite moments is not a realistic task, for this study velocity moments up to fifth order are computed. These provide enough information for accurate description of the flow by using the truncated Gram-Charlier series expansions [21] that represent the probability density function (PDF) of the non-Gaussian turbulent velocity field. Truncation of the series to the fourth order allows to model moments of fifth order and higher in terms of lower-order ones with minor loss of accuracy [65].

Direct numerical simulations have been used successfully in the past to validate the truncated Gram-Charlier series expansion in shear flows such as turbulent channel flows [35] and turbulent boundary layers [65]. However, such validation has not been performed in free-shear layer flows, like the turbulent mixing layer. Therefore, a secondary objective of the current work is to validate the Gram-Charlier series expansion in a mixing layer flow using computed statistics.

The third objective of the this work is to analyze the sensitivity of DNS of turbulent mixing layers to different geometrical and numerical parameters, in order to identify the effect of different sources of uncertainty on numerical simulations of turbulent mixing layers. Such parameters are varied while using fixed flow conditions. Among the varied parameters are: domain size, thickness of the splitter plate, inflow boundary layer conditions and grid resolution.

The document is structured as follows: Chapter 2 presents an overview of direct numerical simulations and the numerical method used to solve the governing equations for the incompressible flow. Chapter 3 describes the wind tunnel and flow conditions of the experimental mixing layer used as reference for the numerical study. Chapter 4 presents the computational setup for the different simulations conducted in this study. Sensitivity of numerical results to different computational parameters

is analyzed in Chapter 5. Finally, mean flow statistics of the turbulent mixing layer, including high-order moments and second-order transport equation budget terms, are shown in Chapter 6.

Chapter 2

Methodology

2.1 Direct numerical simulations

Direct numerical simulations (DNS) are used in this work to study the flow physics of turbulent mixing layers. In DNS, the unsteady Navier-Stokes (N-S) equations are solved using numerical methods. No model-form uncertainty is introduced to the flow field, therefore, DNS are considered to be the most accurate representation of a fluid flow attainable through computations.

The non-dimensional Navier-Stokes equations for incompressible flows are:

$$\begin{aligned} \frac{\partial \boldsymbol{U}}{\partial t} + (\boldsymbol{U} \cdot \nabla \boldsymbol{U}) &= -\nabla P + \frac{1}{Re} \nabla^2 \boldsymbol{U} && \text{in } \Omega \\ \nabla \cdot \boldsymbol{U} &= 0 && \text{in } \Omega, \end{aligned} \tag{2.1}$$

where $\boldsymbol{U} = (U, V, W)$ is the velocity vector, P is the scalar pressure, and Ω is the flow domain. Variables and coordinates in Eq. (2.1) have been normalized with respect to a characteristic velocity, U, and a characteristic length scale, δ_c, so that the non-dimensional values are given by:

$$\boldsymbol{U} = \boldsymbol{U}^*/U; \quad x = x^*/\delta_c; \quad P = P^*/(\rho U^2); \quad t = t^* U/\delta_c; \quad Re = U\delta_c/\nu$$

where the $(^*)$ indicates a dimensional quantity and ν is the kinematic viscosity of

the fluid. The equations have associated initial and boundary conditions

$$\boldsymbol{U}(\mathbf{x}, t=0) = \boldsymbol{U}^0(\mathbf{x}),\ \boldsymbol{U} = \boldsymbol{U}_v \text{ on } \partial\Omega_v,\ \nabla U_i \cdot \hat{\mathbf{n}} = 0 \text{ on } \partial\Omega_o, \tag{2.2}$$

where $\hat{\mathbf{n}}$ is the outward facing unit normal vector at the boundary, $\partial\Omega_v$ is the region of the boundary where velocity is imposed (Dirichlet boundary condition) and $\partial\Omega_o$ is where "outflow" condition is imposed (Neumann b.c.).

It is not possible to obtain an analytical solution of Eq. (2.1) [74], but an approximate solution may be obtained using numerical methods. Different approaches to numerically solve the N-S equations include finite difference, finite element, finite volume, global spectral methods and spectral element methods. Finite difference and global spectral methods generally require structured computational grids, where the solution nodes must be ordered and positioned in a specific manner for the method to be applicable. Therefore, their use is generally restricted to very simple flow configurations. Finite element and finite volume methods can be applied on unstructured grids, which provide greater adaptability to complex flow geometries. However, these methods are inefficient for DNS since they require a high number of elements or nodes to achieve the required level of accuracy. The spectral element method, developed by Patera [63], combines the exponential rate of convergence of global spectral methods with the flexibility of finite element/volume methods [24]. In this study, the numerical solution to the N-S equations is obtained using the spectral element method, implemented in the open source code Nek5000 [3], which has proven to be highly scalable on massively-parallel computers [60].

Independent "snapshots", or flow realizations, of an unsteady flow field obtained through DNS are used as statistical samples for computation of the mean flow statistics. Mean quantities are derived by decomposing the instantaneous fields into a mean (average) components, $\langle \boldsymbol{U} \rangle$ and $\langle P \rangle$, and fluctuating components, $\boldsymbol{u}$ and p:

$$\begin{aligned} \boldsymbol{U} &= \langle \boldsymbol{U} \rangle + \boldsymbol{u}, \\ P &= \langle P \rangle + p, \end{aligned} \tag{2.3}$$

where $\langle u \rangle = \langle p \rangle = 0$. Equation 2.3 is known as Reynolds decomposition. Mean

quantities are calculated using an ensemble averaging procedure:

$$\langle Q \rangle_E(x, y, z) = \frac{1}{N_S} \sum_{n=1}^{N_S} Q^{(n)}(x, y, z), \tag{2.4}$$

where N_S is the number of statistical samples or flow realizations, and $Q^{(n)}$ is the value of random variable Q at the n-th flow realization. Since the mixing layer flow is statistically homogeneous in the z-direction, spanwise averaging may be performed to obtain statistics of the planar flow:

$$\langle Q \rangle(x, y) = \frac{1}{L_z} \int_0^{L_z} \langle Q \rangle_E(x, y, z) dz. \tag{2.5}$$

In the current study, mean values are obtained by applying both ensemble and spanwise averaging, Eqs. (2.4) and (2.5) respectively.

2.2 Spectral Element Method

The Navier-Stokes equations in Eq. (2.1), along with the corresponding initial and boundary conditions, represent the strong formulation of the problem. In spectral element method (SEM), the N-S equations are cast into the weak formulation [24]:

$$\begin{aligned} \frac{\partial}{\partial t}(\boldsymbol{U}, \boldsymbol{v}) + (\boldsymbol{U} \cdot \nabla \boldsymbol{U}, \boldsymbol{v}) + \frac{1}{Re}(\nabla \boldsymbol{U}, \nabla \boldsymbol{v}) = (P, \nabla \cdot \boldsymbol{v}) \qquad & \forall \boldsymbol{v} \in \ X_0 \\ -(q, \nabla \cdot \boldsymbol{U}) = 0 \qquad & \forall q \in \ Y. \end{aligned} \tag{2.6}$$

where X_0 and Y are function spaces described below. The weak form is obtained by multiplying the equations by functions $\boldsymbol{v}$ and q and applying the inner product $(\cdot, \cdot)$ defined as

$$(\phi, \psi) \equiv \int_\Omega \phi(x)\psi(x) dx. \tag{2.7}$$

The problem consists in finding $\boldsymbol{U} \in X$ and $P \in Y$ such that Eq. (2.6) is satisfied, with X_0 being the subspace of X satisfying homogeneous boundary condition: $\boldsymbol{v} = 0$ at $\partial\Omega$.

The proper subspaces X and Y for $\boldsymbol{U},\ \boldsymbol{v}$ and $P,\ q$ are defined as:

$$\begin{aligned} X &= \{\boldsymbol{v} : v_i \in H^1(\Omega), i = 1, 2, 3,\ \boldsymbol{v} = \boldsymbol{U}_v \text{ on } \partial\Omega_v\} \\ X_0 &= \{\boldsymbol{v} : v_i \in H^1(\Omega), i = 1, 2, 3,\ \boldsymbol{v} = 0 \text{ on } \partial\Omega_v\} \\ Y &= \mathcal{L}^2(\Omega) \end{aligned} \tag{2.8}$$

The function space $\mathcal{L}^2(\Omega)$ is the space of square-integrable functions on Ω, meaning that if $\phi \in \mathcal{L}^2(\Omega)$, then $(\phi, \phi) = \int_\Omega \phi^2 dx < \infty$. The space $H^1(\Omega)$ consists of functions that are in $\mathcal{L}^2(\Omega)$ whose derivatives are also in $\mathcal{L}^2(\Omega)$.

The domain Ω is divided into E subdomains or spectral elements, Ω_e. Discrete analogs of spaces X and Y are chosen in the tensor product space of Nth-order Legendre polynomial interpolation expansions, $h_i^N(x)$, on Gauss-Lobatto-Legendre (GLL) quadrature points, ξ_i^N:

$$h_i^N(x) = -\frac{1}{N(N+1)} \frac{1}{L_N(\xi_i)} \frac{(1-x^2)L'_N(x)}{x - \xi_i} \tag{2.9}$$

where $L_N(x)$ is the Nth-order Legendre polynomial, given by:

$$\begin{aligned} L_0(x) &= 1, \\ L_1(x) &= x, \\ (k+1)L_{k+1} &= (2k+1)xL_k(x) - kL_{k-1}(x), \qquad k \geq 1. \end{aligned} \tag{2.10}$$

The polynomial interpolants satisfy $h_i^N(\xi_j^N) = \delta_{ij}$, where $\xi_j^N \in [-1, 1]$ denotes the location in elemental (local) coordinates of the j-th GLL quadrature point, where $i = 0, 1, ..., N$, and δ_{ij} is the Kronecker delta:

$$\delta_{ij} = \begin{cases} 1, & \text{if } i = j \\ 0, & \text{if } i \neq j. \end{cases}$$

Each element contains $(N+1)^d$ quadrature (or collocation) points, where d is the dimension of the problem. For a three-dimensional problem, the numerical solution

inside the element, $u^e(x, y, z, t)$, is expressed in terms of the interpolating functions:

$$u^e(x, y, z, t) = \sum_{i=0}^{N} \sum_{j=0}^{N} \sum_{k=0}^{N} u_{ijk}(t) h_i^N(x) h_j^N(y) h_k^N(z) \tag{2.11}$$

where the coefficients u_{ijk} are the values of the solution at collocation points. Note that interpolants in Eq. (2.11) are $C^0(\Omega)$ continuous, meaning that the velocity and pressure fields are continuous in the domain, but continuity is not enforced on their derivatives across element boundaries.

The approach which has been described is based on the $\mathbb{P}_N - \mathbb{P}_N$ formulation [24], where both velocity and pressure fields are computed on the same mesh based on GLL quadrature points with polynomial interpolants of order N. This is an alternative to the $\mathbb{P}_N - \mathbb{P}_{N-2}$ formulation [63], where pressure is computed on Gauss-Legendre quadrature points with polynomial interpolants of order $N-2$. The latter approach yields discontinuous pressure field at element boundaries. To ensure continuity of all variables, the $\mathbb{P}_N - \mathbb{P}_N$ formulation was chosen for the current study.

Discretization in time is done using a characteristics-based third-order time-stepping scheme which calculates the solution along the pathlines (or characteristics) associated with the convecting velocity field $\boldsymbol{U}$. In this method, the time derivative and the convection term are substituted by the material derivative:

$$\frac{D\boldsymbol{U}}{Dt} = \frac{\partial \boldsymbol{U}}{\partial t} + (\boldsymbol{U} \cdot \nabla \boldsymbol{U}) \tag{2.12}$$

For simplicity, the time-stepping scheme is explained in this section using the strong form of the N-S equations, Eq. (2.1). The contributions from non-linear convection term in the material derivative are treated explicitly, while the linear terms in on the right-hand side of the equation are treated implicitly. By applying third-order backwards finite difference (BDF3) to the material derivative, we obtain:

$$\frac{1}{\Delta t}\left(\frac{11}{6}\boldsymbol{U}^n - 3\tilde{\boldsymbol{U}}^{n-1} + \frac{3}{2}\tilde{\boldsymbol{U}}^{n-2} - \frac{1}{3}\tilde{\boldsymbol{U}}^{n-3}\right) = -\nabla P^n + \frac{1}{Re}\nabla^2 \boldsymbol{U}^n \tag{2.13}$$

where n is the current timestep, Δt is the time-step size and $\tilde{\boldsymbol{U}}^{n-q}$ is the value of $\boldsymbol{U}$ at an earlier point in time ($q = 1, 2, 3$) and at a point in space along the characteristics. The values of $\tilde{\boldsymbol{U}}^{n-q}$ can be calculated using a semi-Lagrangian formulation, which involves several off-grid interpolations of the velocity field over each time step, increasing computational cost. The issue is bypassed by the operator-integration factor scheme (OIFS) proposed by Maday, Patera and Rønquist [45]. The scheme computes $\tilde{\boldsymbol{U}}^{n-q}$ by solving the initial-boundary value (IBV) subproblem

$$\begin{aligned} &\frac{\partial \tilde{\boldsymbol{U}}}{\partial s} + \boldsymbol{U} \cdot \nabla \tilde{\boldsymbol{U}} = 0, && s \in [t^{n-q}, t^n], \\ &\tilde{\boldsymbol{U}}(\boldsymbol{x}, t^{n-q}) = \boldsymbol{U}(\boldsymbol{x}, t^{n-q}) && \tilde{\boldsymbol{U}}(\boldsymbol{x}, t) = \boldsymbol{U}(\boldsymbol{x}, t)\ \forall \boldsymbol{x} \in \partial\Omega_c, \end{aligned} \tag{2.14}$$

where $\partial\Omega_c$ is the subset of the boundary $\partial\Omega$ where $\boldsymbol{U} \cdot \hat{\boldsymbol{n}} < 0$, that is, the portion of the boundary having incoming characteristics. Equation (2.14) is a pure convection problem, and it has the effect of propagating the initial condition, $\tilde{\boldsymbol{U}}(\boldsymbol{x}, t^{n-q})$, forward along the characteristics of the convecting field $\boldsymbol{U}$. The IBV problem can be solved using an inexpensive explicit time-stepping scheme such as fourth-order Runge-Kutta (RK4), with step size $\Delta s \leq \Delta t$. More details on the OIFS scheme are found in Refs. [45, 24].

An alternative time-stepping scheme would be a high-order time-splitting method [76], which treats differently linear and non-linear terms in Eq. (2.6). Specifically, the non-linear part of the equation (convective term) is treated explicitly by third-order extrapolation (EXT3), while all other terms are treated implicitly by third-order backwards finite difference scheme (BDF3). In the BDF3/EXT3 method, the Courant-Friedrichs-Levy (CFL) number must satisfy the condition,

$$CFL = |\boldsymbol{U}|\Delta t/\Delta_x < 0.5 \tag{2.15}$$

throughout the domain to maintain stability of the solution, where Δ_x is the grid spacing based on GLL quadrature points. This constraint is relaxed when using the OIFS scheme, since it is stable for $CFL > 0.5$ and allows for much larger time steps than the BDF3/EXT3 scheme. Because of the increased stability of the BDF3/OIFS method, this scheme was chosen for the current work.

2.3 Computations

Simulations were conducted on the Pleiades supercomputer, which is part of NASA's High-End Computing Program [59]. It contains a total of 11,440 nodes, or 245,539 CPU cores, consisting of different types of Intel Xeon processors (Skylake, Broadwell, Haswell, Ivy Bridge, Sandi Bridge). The cluster has a theoretical peak capacity of 7.24 Pflop/s and 935 TB of total memory.

Approximately 6 million CPU hours were used on computations presented in this work. The cost of computations was about 3.24×10^{-05} CPU seconds/time-step/grid point when using Broadwell processors. Computations were conducted using between 2000-5800 CPUs at a time, depending on the size of the computational grid. To have a better understanding of the size of the simulations, it would take about 26 days of wall-time to produce current data for the largest domain computation used in this study, using 5800 CPUs.

About 30 Terabytes of raw data (velocity/pressure fields) were produced from the simulation with the largest domain. Raw data from other simulations summed up to 25 TB approximately, for a total of 55 TB of raw data. The data files are stored on NASA's Lou long-term storage system.

Chapter 3

Experiment

Data from the wind tunnel experiments of Bell and Mehta [10] are used as a reference for our simulations. The design and calibration of the wind tunnel for this experiment is explained in Ref. [9].

In the experiments, two co-flowing boundary layers were developed on both sides of a tapered splitter plate and then, mixed downstream the sharp trailing edge of the plate. The two streams were driven by individual centrifugal blowers, where one has three times the flow capacity of the other. Downstream components of the wide-angle diffusers were identical for the streams. A schematic of the mixing-layer wind tunnel is shown in Fig. 3.1. The test section was 36 cm in the transverse direction, 91 cm in the spanwise direction, and 366 cm in streamwise length. A flexible wall on the low-speed stream side was adjusted to give a nominally zero streamwise pressure gradient.

Both turbulent and laminar inflow conditions were used in the experiment. Turbulent inflow conditions were achieved by perturbing the boundary layers using a round wire trip. Laminar inflow conditions correspond to untripped boundary layers. The high-speed stream had a free-stream velocity of $U_1 = 15m/s$, while the low-speed stream had a free-stream velocity of $U_2 = 9m/s$, for a velocity ratio of $U_1/U_2 = 0.6$. Free-stream values were constant to within 1% of the set velocities,

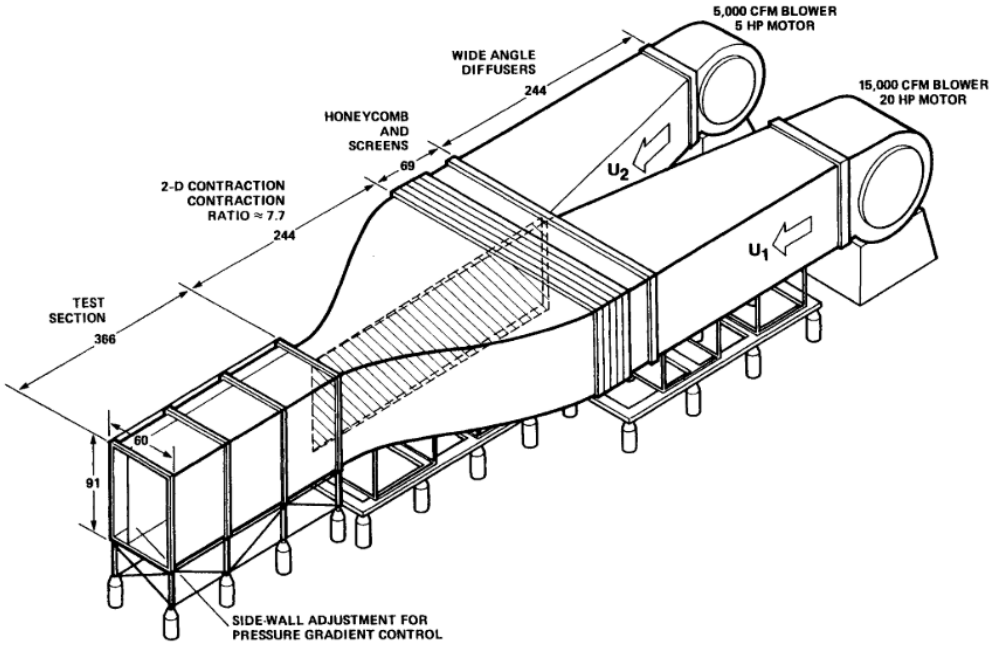

Figure 3.1: Schematic of the mixing-layer wind tunnel, taken from Bell & Mehta [9].

with free-stream turbulence intensity being below $u/U_\infty = 0.15\%$.

Simulations seek to reproduce conditions of untripped boundary layers in vicinity of the splitter plate trailing edge, shown in Table 3.1. By reproducing velocity ratio and inflow conditions, mean flow statistics and shear layer growth rate will be close to experimental values. Therefore, experimental data will be used to validate current numerical results. Untripped inflow conditions were selected for simulations over the tripped case to avoid introducing uncertainty and complexity associated with modeling the turbulent boundary layers.

Table 3.1: Experimental laminar boundary layer parameters at the splitter plate trailing edge [10].

Condition	$\boldsymbol{U_\infty}$ **(m/s)**	$\boldsymbol{\delta_{99}}$ **(cm)**	$\boldsymbol{\theta^{(BL)}}$ **(cm)**	$\mathbf{Re}_\delta$	$\mathbf{Re}_\theta$
High-speed side	15.0	0.40	0.053	3962	525
Low-speed side	9.0	0.44	0.061	2611	362

Statistics from numerical simulations are usually compared with those from experiments to validate the simulation results. In the current study, experimental

data are used only as a reference due to differences in the settings of physical and numerical experiments, which will be discussed in the following chapters.

Chapter 4

Computational Setup

Flow conditions from the untripped case from the wind tunnel experiment performed by Bell & Mehta [10] were described in Chapter 3, as well as inflow boundary layer conditions near the trailing edge of the splitter plate. This chapter discusses the setup of the numerical simulations conducted in this work, which attempt to mimic experimental inflow boundary layer parameters at the trailing edge of the splitter plate and nominally zero mean streamwise pressure gradient.

4.1 Dimensions of computational domains

Seven different computational domains (Cases I-VII in Table 4.1) were used in the simulations. The computational domains have a similar cross-section in the (x,y)-plane shown in Figure 4.1. In the figure, the thick black line represents the splitter plate and thin lines indicate other boundaries of the domain.

Dimensions of the different domains are presented in Table 4.1. Hereafter, all length scales are normalized using $\delta_1 = \delta_{99} = 0.4\ cm$ at the high-speed flow side of the splitter plate. Dimensions L_1 and L_2 are the development lengths of the high-speed and low-speed boundary layers, respectively. The development region of length $L_3/\delta_1 = 10$ is added upstream of the splitter plate to avoid the singularities in the

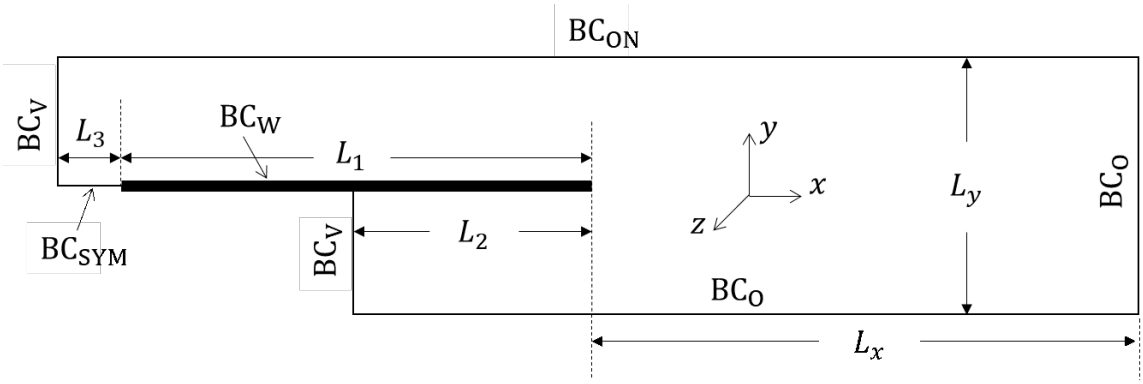

Figure 4.1: Computational domain geometry and the boundary conditions: BC_O **- outflow,** BC_{ON} **- outflow/normal,** BC_V **- uniform velocity,** BC_W **- wall (no-slip),** BC_{SYM} **- symmetry (free-slip).**

boundary conditions.

Table 4.1: Computational domain dimensions.

Case	Description	L_1/δ_1	L_2/δ_1	L_x/δ_1	L_y/δ_1	L_z/δ_1
I	Small domain	175	140	170	70	23.4
II	Small domain, reduced L_y	175	140	170	50	23.4
III	Small domain, increased L_y	175	140	170	90	23.4
IV	Large domain	175	140	350	90	40.0
V	Large domain, reduced L_x	175	140	170	90	40.0
VI	Large domain, reduced L_x and L_z	175	140	170	90	23.56
VII	Small domain, reduced L_1 and L_2	160	76	170	70	23.4

The trailing edge of the plate is located at $x = 0$. Positive x-values are in the region, where two boundary layers mix (thereafter, mixing region). The mixing region length, L_x, varies in the simulations between $170\delta_1$ and $350\delta_1$. To compare, the mixing region length of the test section in the experiments was $915\delta_1$, with self-similarity being observed in some flow characteristics by $L_x \sim 312.5\delta_1$.

The y-values are negative in the lower part of the domain and positive in its upper part, with $y = 0$ being located at the splitter plate bottom in Cases I-III and VII and at the middle of the splitter plate in Cases IV-VI due to different grids used in these cases (see discussion on grids in Section 4.4). Minimum and maximum y-values correspond to $\pm L_y/2$, where L_y is the domain dimension in the transverse direction. The z-values run from 0 to L_z between the domain boundaries, where L_z is

the domain dimension in the spanwise direction. In the simulations, both L_y and L_z vary as shown in Table 4.1. The largest value of L_y, $90\delta_1$, corresponds to the length of the experimental test section, 36 cm, in this direction. The largest dimension of the computational domain in the spanwise dimension is $40\delta_1$. The wind tunnel test section size in this direction was $227.5\delta_1$. A small difference in L_z in Cases III and VI is due to different grids used in these cases.

The sharp-ended splitter plate is uniform in simulations, with its thickness being $h = 0.25mm = 0.0625\delta_1$, which is the thickness of the experimental splitter plate at the trailing edge. In experiments, however, the plate has a 1 degree taper. The taper was not introduced in the simulated splitter plate, which allowed for easier control of boundary layer parameters at the plate's trailing edge.

4.2 Boundary conditions

In the Nek5000, boundary conditions are applied to the velocity field, while the pressure values at the boundaries are computed . Boundary conditions used in our simulations are shown in Figure 4.1 for all domain boundaries. They are the standard options in Nek5000. At the inlet, the following velocity profile is assigned:

$$U(y) = \begin{cases} U_1/U_\infty = 1.0, & \text{if } y > 0 \\ U_2/U_\infty = 0.6, & \text{if } y < 0, \end{cases} ; \qquad V = W = 0; \tag{4.1}$$

where velocities are normalized with respect to the free-stream velocity on the high-speed side, $U_\infty = 15$ m/s. The no-slip boundary condition are applied everywhere on the splitter plate. The symmetry condition are applied at the lower boundary of the region upstream of the splitter plate. The convective outflow condition, $[P\boldsymbol{I} + \nabla \boldsymbol{U}] \cdot \hat{\boldsymbol{n}} = 0$, are applied at the outlet. Here, $\boldsymbol{I}$ is the identity matrix, and $\hat{\boldsymbol{n}}$ is the unit vector normal to the boundary and directed outwards. The convective outflow condition is also applied at the lower boundary of the domain. The outflow-normal condition is applied at its upper boundary. This condition implies that the velocity

component normal to the boundary is free ($\partial V/\partial n = 0$), but the tangential velocity components are fixed: $U = U_1/U_\infty$ and $W = 0$. The outflow conditions ensure that mean pressure gradient is equal to zero in the streamwise direction. In the spanwise direction, the periodic boundary conditions are used.

4.3 Initial conditions

Velocity profiles in (4.1) are used in Cases I and IV-VII throughout the domain as initial conditions. Cases II and III use a single flow realization from Case I at the simulation time $t = 500$ for this purpose. (In the simulations, t is non-dimensional, normalized with respect to U_1 and δ_1: $t = (U_1 t^*)/\delta_1$, where t^* is the dimensional time.) A spectrally accurate interpolation of the flow field from Case I was obtained for Case II using Nek5000 tools. For Case III, the velocity field was interpolated from Case I, where data was available ($|y/\delta_1| < 35$), while uniform velocity profiles (4.1) were assigned at $|y/\delta_1| > 35$.

4.4 Grids

The base grid used in Cases I-III is shown in Figure 4.2 in terms of conforming meshing zones in the (x, y)-plane. Coordinates of the enlarged black points that indicate zones' end points in the figure are shown in Table 4.2. The grid parameters for each zone are given in Table 4.3. In the table, n_x and n_y are the number of elements in the x and y directions, r_x and r_y are the growth rates in each direction, and Δx and Δy are the element sizes in the respective directions. The growth rate $r_y = \Delta y^{i+1}/\Delta y^i$ is the ratio between the sizes of adjacent elements Δy^{i+1} and Δy^i, where the index i is increasing in the direction of $+y$. The rate r_x is similarly defined in the direction of $+x$. The description of zones M and N are omitted, since they are the mirror reflections of zones H and G with respect to $y = 0$.

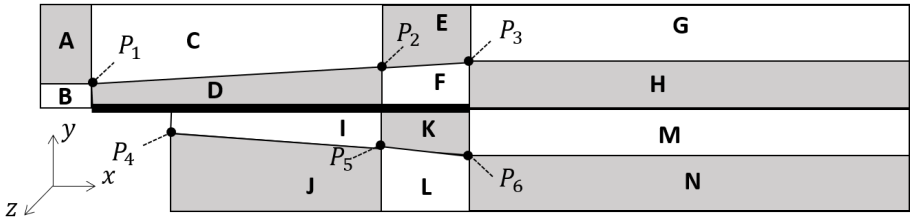

Figure 4.2: Meshing zones for the base grid of Cases I-III (figure not to scale).

Table 4.2: Coordinates of enlarged black points in Figure 4.2.

Point	P_1	P_2	P_3	P_4	P_5	P_6
x/δ_1	-175.	-50.	0.	-140.	-30.	0.
y/δ_1	4.	9.7	12.	-4.	-10.3	-12.

A row of rectilinear elements (not listed in the table) was added downstream of the thick plate in the region between zones H and M. In the y-direction, this is an additional element, which size is equal to the splitter plate thickness in order to maintain a conforming grid required by the solver. In the x-direction, the number and dimensions of these elements are the same as in the adjacent zones H and M.

The base grid as described above is used in the Case I simulations. For Case II, the base grid is modified by removing two elements (adjacent to the domain boundaries) in the y-direction from each of the outer regions (A, C, E, G, J, L, N).

In Case III, two elements are added to the base grid in the y-direction to each of the outer regions (A, C, E, G, J, L, N) of the base grid. Then, the grid is re-meshed within the new boundaries of the zones using the same vertical growth rates r_y shown in Table 4.3 for the corresponding zones. As a result, the min. Δy-value is decreased

Table 4.3: Parameters for the base grid for Cases I-III.

Zone:	**A**	**B**	**C**	**D**	**E**	**F**	**G**	**H**	**I**	**J**	**K**	**L**
n_x	5	5	25	25	15	15	110	110	21	21	9	9
n_y	6	8	6	8	6	8	6	8	8	6	8	6
r_x	0.87	0.87	1.041	1.041	0.89	0.89	1.004	1.004	1.05	1.05	0.92	0.92
r_y	1.15	1.06	1.15	1.06	1.15	1.06	1.15	1.06	0.943	0.87	0.943	0.87
Min. $\Delta x/\delta_1$	1.5	1.5	3.33	3.33	1.74	1.74	1.17	1.17	2.1	2.1	2.34	2.34
Max. $\Delta x/\delta_1$	2.6	2.6	8.4	8.4	5.6	5.6	1.75	1.75	4.58	4.58	4.55	4.55
Min. $\Delta y/\delta_1$	3.54	0.41	2.79	1.03	2.63	1.17	2.63	1.17	0.92	3.	1.17	2.63
Max. $\Delta y/\delta_1$	7.12	0.58	5.63	1.55	5.3	1.75	5.3	1.75	1.47	6.94	1.75	5.3

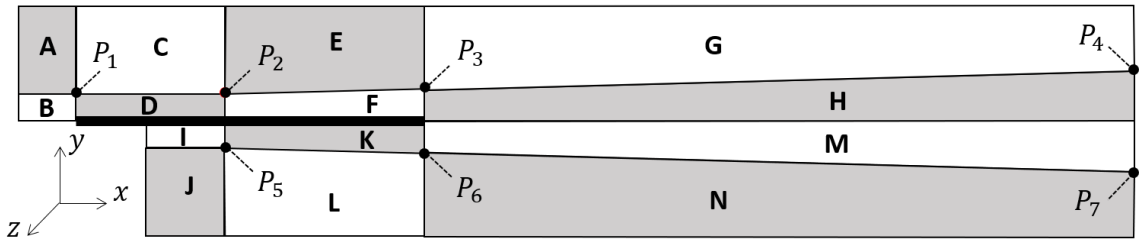

Figure 4.3: Meshing zones for the base grid of Cases IV-VI (figure not to scale).

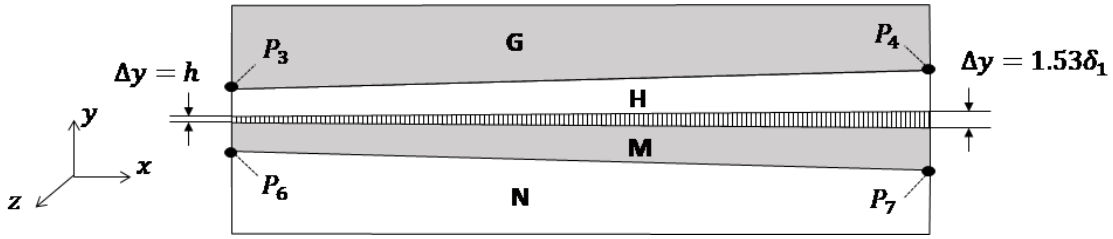

Figure 4.4: Schematic view of the single row of elements added in the region between zones H and M in the base grid for Cases IV-VI.

by 8.5% and the max. Δy-value is increased by 21% in each altered zone with respect to their values in different zones shown in Table 4.3. Dimensions of the elements in the x-direction are unchanged with respect to the base grid. Zones B, D, F, H, I, K, and M in the domain inner region remain the same in Cases I-III.

In the spanwise direction, the three grids used in Cases I-III have twenty (20) uniformly distributed elements of the size $\Delta z/\delta_1 = 1.17$.

The total numbers of grid elements in Cases I-III are: 84,800, 73,000 and 96,600, respectively.

The base grid used in Cases IV-VI is shown in Figure 4.3, with the zones end points and parameters listed in Tables 4.4 and 4.5, respectively. Zones M and N are the mirror reflections of zones H and G with respect to $y = 0$ and therefore, not described in the tables.

One row of elements is added downstream of the plate, in the region between zones H and M (Figure 4.4). The elements in this row adjacent to the trailing edge of the splitter plate at $x = 0$, have the same thickness as the plate: $h = 0.25mm = 0.0625\delta_1$.

Table 4.4: Coordinates of enlarged black points in Figure 4.3.

Point	P_1	P_2	P_3	P_4	P_5	P_6	P_7
x/δ_1	-175.	-140.	0.	350.	-140.	0.	350.
y/δ_1	4.	4.	7.69	21.	-4.	-7.69	-21.

Table 4.5: Parameters for the base grid for Cases IV-VI.

Zone:	**A**	**B**	**C**	**D**	**E**	**F**	**G**	**H**	**I**	**J**	**K**	**L**
n_x	5	5	17	17	27	27	299	299	10	10	25	25
n_y	7	9	7	9	7	9	7	9	9	7	9	7
r_x	0.87	0.87	1.05	1.05	0.926	0.93	1.005	1.005	1.05	1.05	0.931	0.931
r_y	1.1	1.06	1.1	1.06	1.1	1.06	1.1	1.06	0.943	0.909	0.943	0.909
Min. $\Delta x/\delta_1$	1.5	1.5	2.78	2.78	0.91	0.91	0.45	0.45	3.1	3.1	0.91	0.91
Max. $\Delta x/\delta_1$	2.6	2.6	6.06	6.06	6.66	6.66	1.53	1.53	4.8	4.8	5.04	5.04
Min. $\Delta y/\delta_1$	4.32	0.35	4.32	0.35	3.93	0.67	2.53	1.53	0.35	4.32	0.67	3.93
Max. $\Delta y/\delta_1$	7.66	0.55	7.66	0.55	6.97	1.07	4.50	2.44	0.55	7.66	1.07	6.97

Downstream, the element size Δy increases linearly with x until it becomes equal to the thickness $\Delta y/\delta_1 = 1.53$ of the elements in the neighboring zones H and M at the end of the computational domain ($x/\delta_1 = 350$). In the x-direction, the elements in this row have the same sizes and growth rates as those in the adjacent zones H and M (Table 4.5).

The grid has 34 uniformly distributed elements in the spanwise direction of size $\Delta z/\delta_1 = 1.178$.

Overall, the area downstream the splitter plate is more refined in the base grid for Cases IV-VI than in the base grid used in the Cases I-III simulations. The grid resolution near the splitter plate trailing edge is shown for both grids in Figure 4.5 for comparison.

The base grid used in the Case IV simulations is modified by cutting it off at $x/\delta_1 = 170$ to obtain the grid used in the Case V simulations. The total numbers of the grid elements in Cases IV and V are 381,174 and 233,070, respectively.

The grid for Case VI was obtained from the Case V grid by cutting it off at $z/\delta_1 = 23.56$, which is the closest point near the location of the grid boundary in Case I ($L_z = 23.4\delta_1$). This domain dimension corresponds to 20 uniformly distributed elements with $\Delta z/\delta_1 = 1.178$. The total number of grid elements in Case VI is

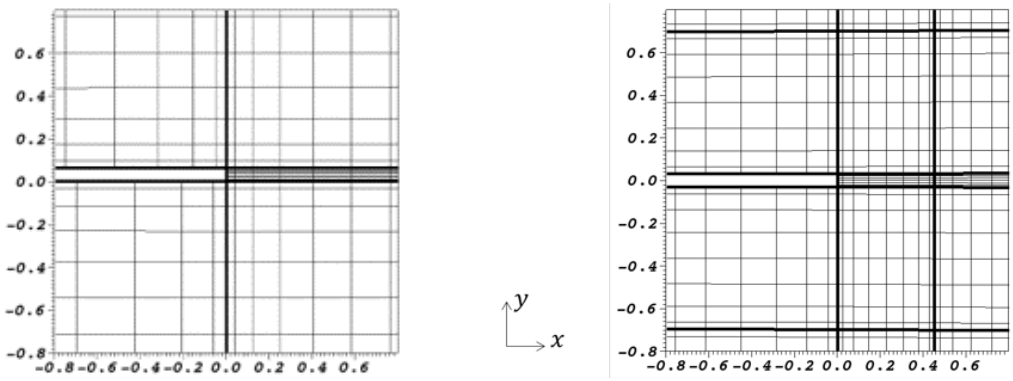

(a) **(b)**

Figure 4.5: Spectral element grid (thick lines) and quadrature points (intersection of thin lines) near the trailing edge of the plate in the base grids for a) Cases I-III,VII and b) Cases IV-VI.

137,100.

Finally, the grid used in Case VII is the same as in Case I but with shorter development lengths used in this case (Table 4.1), resulting in fewer elements over the plate: Zones C/D have $n_x = 24$, Zones E/F have $n_x = 11$, and Zones I/J have $n_x = 16$. Coordinates of grid points points were also relocated accordingly: $P_1 = (-160, 4)$, $P_2 = (-30, 10.5)$, $P_4 = (-76, 4)$ and $P_1 = (-30, 8.8)$.

Resolution in y and z-directions are left unchanged with respect to Case I. The total number of elements in Case VII was 82,000.

The base grids from Figures 4.2 and 4.3 that include only spectral elements without collocation points are shown in Figure . The number of quadrature points located inside each element is $(N+1)^3$, with the $N+1$ quadrature points being located in each direction based on the distribution of Gauss-Legendre-Lobatto quadrature points in local (elemental) coordinates. Polynomial interpolants of order $N = 11$ are used in all cases. Therefore, the total number of grid points is 142 million in the smallest grid (Case VII) and 659 million in the largest grid (Case IV).

All grids are designed to satisfy the requirement of $(\delta x \cdot \delta y \cdot \delta z)^{1/3} < 4\eta_K \div 8\eta_K$

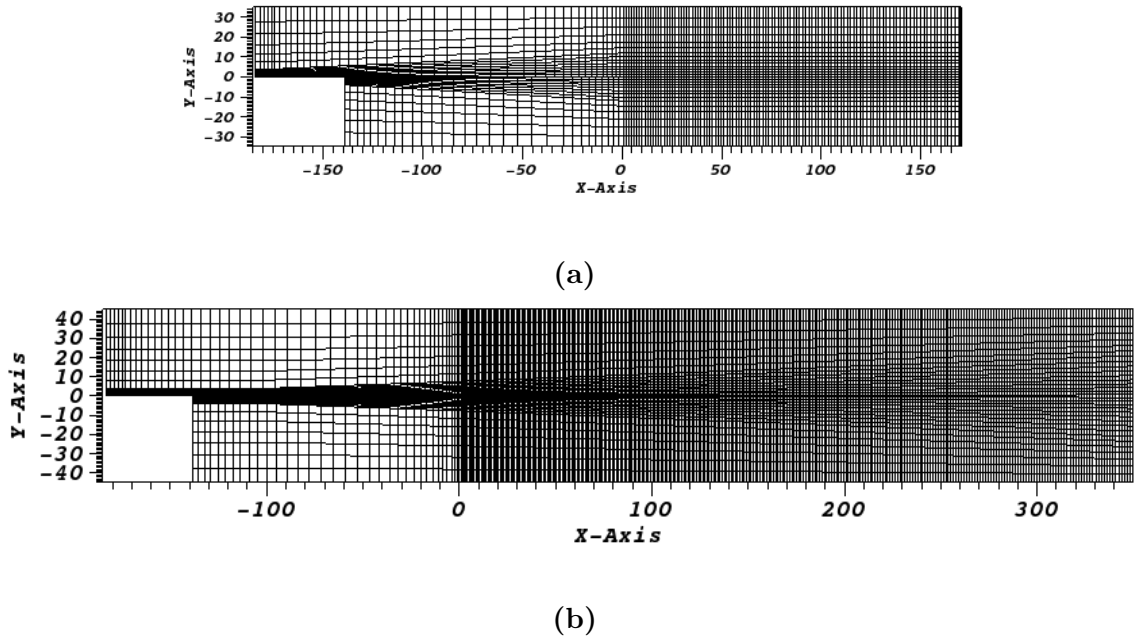

Figure 4.6: The base grids of spectral elements shown without internal collocation points for a) Cases I-III and b) Cases IV-VI.

[61, 78], where δx,δy, δz is the average spacing between quadrature points within elements in streamwise, transverse, and spanwise directions, η_K is the Kolmogorov length scale $\eta_K = (\nu^3/\varepsilon)^{1/4}$. Specifically, the grid resolution in Cases I III and VII is $(\delta x \cdot \delta y \cdot \delta z)^{1/3} < 5.33\eta_K$, while in Cases IV-VI, it is $(\delta x \cdot \delta y \cdot \delta z)^{1/3} < 4.9\eta_K$, everywhere in the flow.

4.5 Temporal resolution

Simulations were conducted using the BDF3-OIFS temporal discretization scheme described earlier. For Cases I-VI, a non-dimensional timestep of $\Delta t = 0.02$, where Δt is normalized with respect to U_1 and δ_1. In Cases I-III, this yields $CFL = 0.75$, and $CFL = 1.8$ in Cases IV-VI (due to a finer grid). The timestep size was selected to target $CFL < 2$, which is recommended when using BDF3/OIFS temporal discretization scheme for DNS [3]. Two different time steps were used in Case VII simulations, $\Delta t = 0.02$ and $\Delta t = 0.012$, resulting in $CFL = 075$ and 0.45

respectively.

Chapter 5

Sensitivity Analysis

Sensitivity of turbulence statistics in direct numerical simulations of mixing layers to specific computational parameters is analyzed in this chapter. The parameters that were varied in this study are the dimensions of the computational domain, the level of development of inflow boundary layers at the trailing edge of the splitter plate, computational grid refinement and splitter plate thickness.

5.1 Comparison of experimental and DNS data

Several differences between wind tunnel and numerical flow conditions were discussed in Chapters 4, for example, domain size and taper angle of the splitter plate. Because experimental flow conditions cannot be replicated exactly in the simulation, this leads to differences in the characteristics of the boundary layers at the trailing edge of the splitter plate.

Table 5.1 compares the shape factors and the skin friction coefficients of the experimental boundary layers at the trailing edge of the splitter plate with their values in the corresponding Blasius laminar boundary layers. Data in the table demonstrate that conditions of both boundary layers and particularly, the one at the low-speed side of the plate, are not laminar. There is also a difference in the

Table 5.1: Experimental boundary layer characteristics near the splitter plate trailing edge.

Stream	U_∞ **m/s**	**Shape factor,** H		**Skin friction coefficient,** $C_f \times 10^3$		
		Exp.	Blasius	Ref. [10]	Ref. [9]	Blasius
High-speed	15	2.52	2.59	0.72	0.87	0.84
Low-speed	9	2.24	2.59	0.91	1.56	1.22

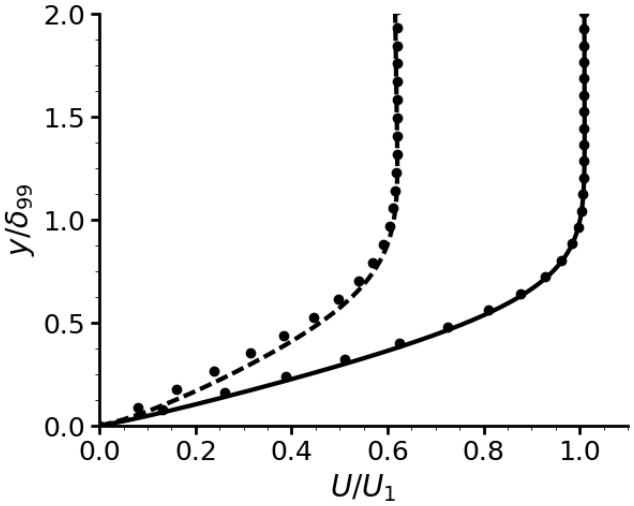

Figure 5.1: Velocity profiles of the boundary layers at the trailing edge of the splitter plate in the Case I simulations. Notations: lines DNS results, circles the Blasius solutions. Lines: solid at the high-speed side, dashed at the low-speed side of the splitter plate.

experimental skin friction coefficient values reported in different publications and the origin of this difference is unclear.

As discussed in [9], deviation of the experimental boundary layers from planar laminar conditions can be linked to constructional features of a wind tunnel such as screens. These features and upstream turbulence conditions cannot be accurately reproduced in numerical experiments. Figure 5.1 compares velocity profiles of the boundary layers at the splitter plate trailing edge obtained in the Case I simulations with the Blasius solutions.

Corresponding velocity profiles from other cases overlap with those in Case I. Calculated profiles are close to the theoretical ones in laminar boundary layers. All

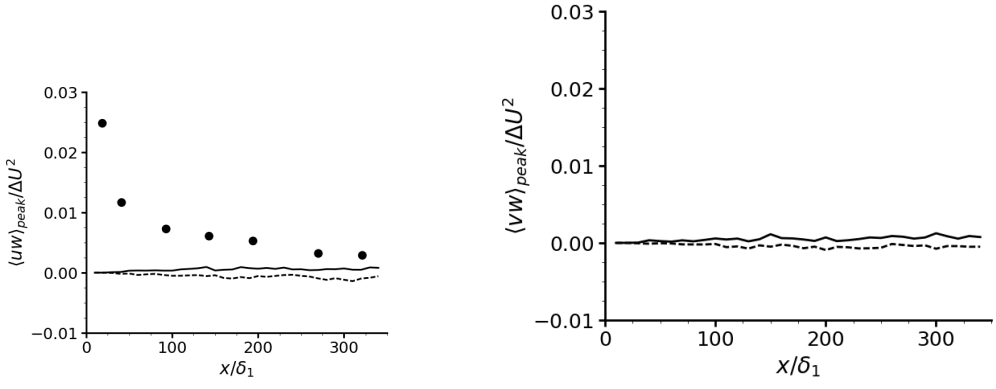

(a) **(b)**

Figure 5.2: Streamwise variations of experimental maximum and minimum values of the secondary shear stress a) $\langle uw \rangle$ and $\langle vw \rangle$. Notation: circles - maximum values from the experiments [10], lines - DNS data from Case IV. Solid lines - maximum values, dashed lines - minimum values.

Reynolds stresses are zero at this location in all simulations. As an example, the shear stresses $\langle uw \rangle$ and $\langle vw \rangle$ from Case IV are shown in Figure. 5.2. Both shear stresses are equal to zero when the boundary layers leave the splitter plate. In contrast, the boundary layers in the experiments are only "nominally laminar, meaning they have well-defined three dimensional (3D) structure and turbulence level between 0.05% and 0.15%, before they leave the splitter plate trailing edge. The 3D structure of the boundary layers is indicated, in particular, by streamwise variation of the maximum value of the shear stress, $\langle uw \rangle$, shown in Figure 5.2(a). The shear stress values presented in the figure by solid circles are averaged in the spanwise direction. The maximum peak value of $\langle uw \rangle$ is near the splitter plate trailing edge. In a planar laminar flow, this shear stress would disappear, as in current simulations. The three-dimensional structure of experimental boundary layers and their contamination with turbulence may be responsible for the virtual origin of the mixing layer being upstream from the trailing edge [10].

Table 5.2 lists conditions of the boundary layers at the splitter plate trailing edge in the simulations. The boundary layer thickness and momentum thickness in Cases I-VI are within 1.5% and 2.5% of corresponding experimental values provided in

Table 5.2: Laminar boundary layer parameters at the splitter plate trailing edge.

Case	**Condition**	U_∞/U_1	δ_{99}/δ_1	θ/δ_1	Re_δ	Re_θ	**Shape factor**, H	**Skin friction coefficient**, $C_f \times 10^3$
I-VI	High-speed side	1	0.99	0.143	3930	565	2.35	1.15
I-VI	Low-speed side	0.6	1.01	0.153	2412	364	2.22	2.48
VII	High-speed side	1	0.95	0.136	3746	540	2.34	1.25
VII	Low-speed side	0.6	0.74	0.118	1751	281	2.16	3.14

Table 5.1 on both sides of the splitter plate. Boundary layer parameters in Case VII

The Reynolds numbers are close to those in the experiments. The mixing layer thickness and the Reynolds numbers obtained in different simulations vary within 1% of their values shown in Table 5.2.

Interestingly, the shape factor, H, and the skin friction coefficient, C_f, obtained in the simulations deviate from the Blasius solutions. They show the evidence of a slightly favorable pressure gradient at the trailing edge of the plate, with all calculated shape factor values being even lower than in the experiments, whereas the skin friction coefficients being higher than the corresponding values from the experiments and the Blasius solutions. In preliminary simulations of a boundary layer developing over a flat plate without the mixing layer being present, the Blasius solution was reproduced exactly using the same grids and the flow conditions as in the current simulations. This suggests that the mixing layer development downstream from the splitter plate trailing edge affects the upstream flow. It also implies that the shape factor and the skin friction coefficient may not be a good choice of parameters to monitor for determining whether boundary layers are laminar in this particular flow geometry, because all examined flow statistics point to them being laminar at the trailing edge of the splitter plate.

Another difference between numerical and physical experiments is the way the streamwise pressure gradient is controlled: via a flexible wall on the low-speed side of the experimental test section vs. a choice of the boundary conditions in simulations described in Section 4.2.

Even though all listed differences between the simulations and the experiments affect the mixing layer development, comparison of numerical and experimental results is still beneficial for better understanding of those effects, and particularly, in the light that the numerical experiments generate the laminar planar boundary layers prior to their mixing, reproducible in different simulations conducted in this study.

5.2 Collection of statistical data

Statistics were collected after the flow became statistically stationary. The flow was deemed statistically stationary, when the volume-averaged statistics relevant to the flow kinetic energy: $\langle U^2 \rangle_V$, $\langle V^2 \rangle_V$ and $\langle W^2 \rangle_V$, were stabilized. Here, $\langle ... \rangle_V$ is the volume average, and U, V, W are components of the instantaneous flow velocity.

In the simulations started at $t = 0$ (Cases I, IV-VII), the initial transient period excluded from the data collection was $t_{trans} = 500$. Hereafter, all time intervals are non-dimensional, normalized by δ_1/U_1. The initial transient period corresponds to 2.4 flow-through times $\tau_f = L_x/U_c$ in Cases I and V-VII, and to $1.15\tau_f$ in Case IV. In the τ_f-definition, L_x is the mixing layer region length from Table 4.1 (it is longer in Case IV), and $U_c = (U_1 + U_2)/2$ is the centerline velocity.

Cases II and III were started from the Case I solution at $t = 500$. The initial transient was extended to $t = 1000$. The total simulation time for these two cases was also increased to compare with other cases, so that statistics for all cases, but Case IV, were collected during the same number of flow-through times, $7.05\tau_f$. This corresponds to the time interval $t = [500, 2000]$ in Cases I and V-VII, and to $t = [1000, 2500]$ in Cases II and III.

Case IV has the longest mixing layer region of all considered cases in the streamwise direction: $350\delta_1$ vs. $170\delta_1$ (Table 4.1). To obtain statistics that are sufficiently converged for the purposes of the current study, data were collected during $12.1\tau_f$ corresponding to the time interval $t = [500, 5780]$. This is about twice the flow-through

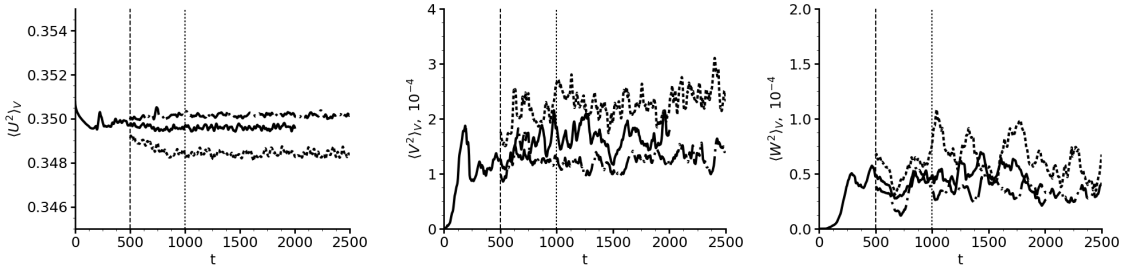

(a) **(b)** **(c)**

Figure 5.3: Time evolution of the volume-averaged statistics relevant to the flow kinetic energy, a) streamwise component, $\langle U^2 \rangle_V$, b) transverse component, $\langle V^2 \rangle_V$, c) spanwise component, $\langle W^2 \rangle_V$. Vertical lines mark the separation between transient and statistically stationary periods for Case I (dashed) and Cases II and III (dotted). Lines: solid Case I, dashed Case II, dash-dot Case III.

time used in the other cases.

Figures 5.3 and 5.4 demonstrate the convergence of $\langle U^2 \rangle_V$, $\langle V^2 \rangle_V$ and $\langle W^2 \rangle_V$ for Cases I-III and Case IV, respectively. Similar results were obtained for Cases V-VII, now shown here. In the figures, vertical dashed and dotted lines indicate the start times of collecting data. The dashed lines correspond to Cases I and IV, and the dotted lines are used for Cases II and III.

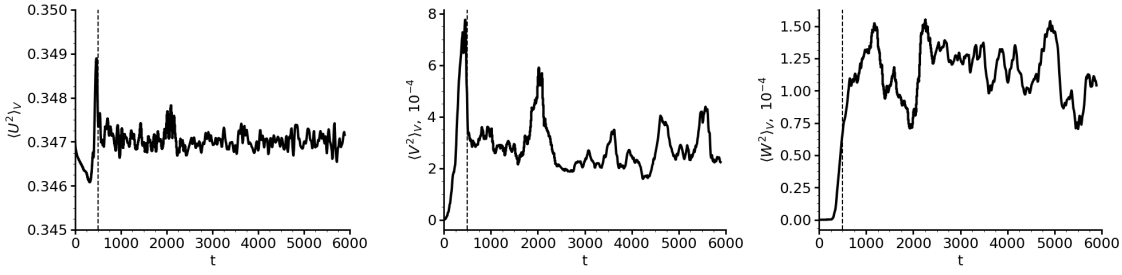

(a) **(b)** **(c)**

Figure 5.4: Time evolution of the volume-averaged statistics relevant to the flow kinetic energy in Case IV, a) streamwise component, $\langle U^2 \rangle_V$, b) transverse component, $\langle V^2 \rangle_V$, c) spanwise component, $\langle W^2 \rangle_V$. Vertical lines mark the separation between transient and statistically stationary periods.

In Cases I-III, and V-VII, $N_s = 376$ snapshots were analyzed when time step size $\Delta t = 0.02$ was used. In Case VII simulation with $\Delta t = 0.012$, $N_s = 419$ was used.

The number of snapshots used in Case IV was $N_s = 529$. That is, increasing the domain dimension in the streamwise direction has several associated penalties: longer averaging time and more statistical samples required for obtaining converged statistics and a larger size of the output data files, which lead to substantially increased demand for storage and computational resources.

Statistics where averaged using ensemble and spanwise averaging as explained in Section 2.1.

5.3 Statistical convergence of collected data

In this section, statistical convergence of numerical results for Cases III and IV is demonstrated. Case III is representative of Cases I,II and VII, as the domain for this case is larger or comparable in the three directions than the domains used in such cases. The three domains are discretized using the same base grid in the mixing layer region. Time and the number of flow realizations used to collect statistics were the same in most cases. When smaller time step was used in Case VII, the number of flow realizations was increased, which accelerates convergence of statistics.

In Cases IV-VI, the different base grid is used than in Cases I-III as described in Section 4.4. The Case IV domain is larger or comparable in different directions to those used in the other two cases. In Cases V and VI, statistics converged when collected for the same time using the same number of flow realizations as in Cases I-III. Case IV required a longer simulation time and more flow realizations to achieve similar convergence of statistics as in the other cases due to longer correlation times of large-scale eddies growing with the downstream distance in the mixing layer.

To analyze the statistics convergence in Case III, their profiles obtained by the

data averaging over three time intervals:

$$T_1^{(III)} = [1000, 2100], \qquad T_2^{(III)} = [1000, 2300], \qquad T_3^{(III)} = [1000, 2500],$$

are compared. The difference between consecutive intervals is about one flow-through time, τ_f. The number of flow realizations corresponding to each interval is: $N_{s1} = 276$, $N_{s2} = 326$, and $N_{s3} = 376$, respectively.

A similar approach is employed to present the statistics convergence in Case IV, with three intervals used to collect the statistics being:

$$T_1^{(IV)} = [500, 4900], \qquad T_2^{(IV)} = [500, 5340], \qquad T_3^{(IV)} = [500, 5780].$$

The difference between the consecutive intervals is also about one flow-through time for this case (defined based on the Case IV domain). The corresponding numbers of the flow realization used for the data averaging are: $N_{s1} = 441$, $N_{s2} = 485$, and $N_{s3} = 529$.

Statistics considered in the current paper are mixing layer thickness, momentum thickness, and the normal Reynolds stresses integrated across the mixing layer, all evolving in the streamwise direction. Also presented are profiles of four Reynolds stresses ($\langle u_i^2 \rangle$ and $\langle uv \rangle$) at different locations in the streamwise direction. The mixing layer thickness, δ_{ML}, is defined as in [10]:

$$\delta_{ML} = (y - y_0)/\eta, \tag{5.1}$$

where the normalized transverse coordinate η is obtained by computing the least-squares fit of the mean velocity profile to the error function profile shape:

$$(\langle U \rangle - U_2)/\Delta U \approx [1 + \mathtt{erf}(\eta)]/2. \tag{5.2}$$

In Eq. (5.1), y_0 is the centerline of the mixing layer calculated using the least-square fitting procedure. The momentum thickness is given by:

$$\theta = \frac{1}{\Delta U^2} \int_{-\infty}^{\infty} (U_1 - \langle U \rangle)(\langle U \rangle - U_2) dy. \tag{5.3}$$

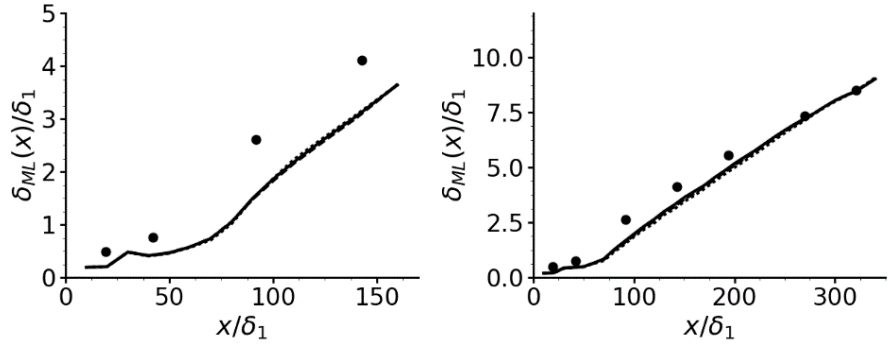

(a) **(b)**

Figure 5.5: Evolution of the mixing layer thickness: a) Case III, b) Case IV. Notations: dotted line - DNS data averaged over T_1, dashed line - DNS data averaged over T_2, solid line - DNS data averaged over T_3, circles - experimental data [10].

The normal Reynolds stresses integrated across the mixing layers are determined as

$$K_x(x) = (1/\Delta U^2) \int_{-Ly/2}^{Ly/2} \langle u^2 \rangle dy, \tag{5.4}$$

$$K_y(x) = (1/\Delta U^2) \int_{-Ly/2}^{Ly/2} \langle v^2 \rangle dy, \tag{5.5}$$

$$K_z(x) = (1/\Delta U^2) \int_{-Ly/2}^{Ly/2} \langle w^2 \rangle dy. \tag{5.6}$$

Evolution of the mixing layer thickness in the streamwise direction in Cases III and IV is shown in Figure 5.5. The figure demonstrates that this parameter is not affected by further increase in the averaging time in both cases. In this and following figures, experimental data are shown as well (solid circles) for comparison.

The normal Reynolds stresses integrated across the mixing layer show more sensitivity to the averaging time (Figures 5.6 and 5.7), with the most and the least affected being K_y and K_z, respectively. Nevertheless, these parameters have converged as well in both cases.

Convergence of the Reynolds stress profiles at $x/\delta_1 = 160$ (Cases III and IV) and

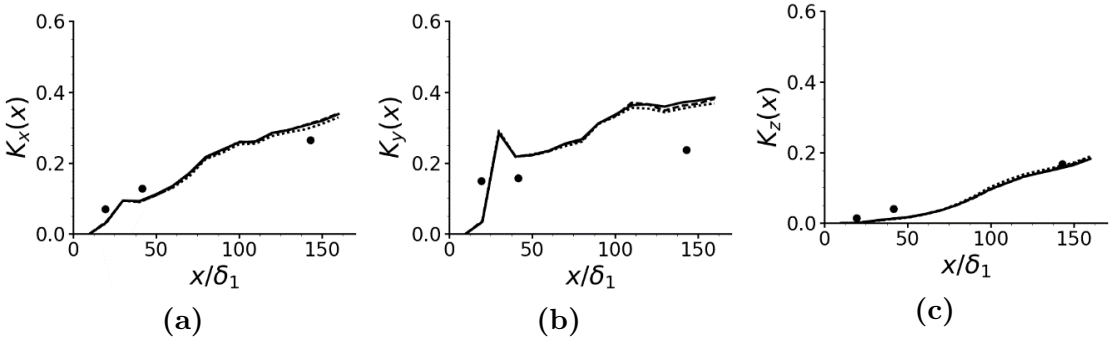

Figure 5.6: Streamwise evolution of the normal Reynolds stresses integrated across the mixing layer in Case III. a) K_x, b) K_y, c) K_z. Notations are the same as in Figure 5.5.

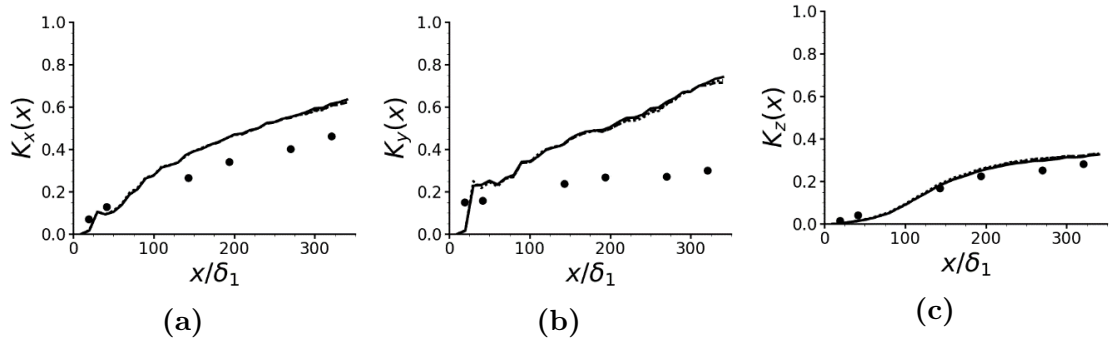

Figure 5.7: Streamwise evolution of the normal Reynolds stresses integrated across the mixing layer in Case IV. a) K_x, b) K_y, c) K_z. Notations are the same as in Figure 5.5

$x/\delta_1 = 320$ (Case IV), is shown in Figures 5.8-5.10. These locations are chosen for being close to the domain outlets in these cases. The figures demonstrate satisfactory convergence of the Reynolds stresses at $x/\delta_1 = 160$ in Case III and at both locations in Case IV. One of the observations from the data analysis is that convergence of the spatial evolution of K_y guarantees convergence of other considered statistics in this flow geometry.

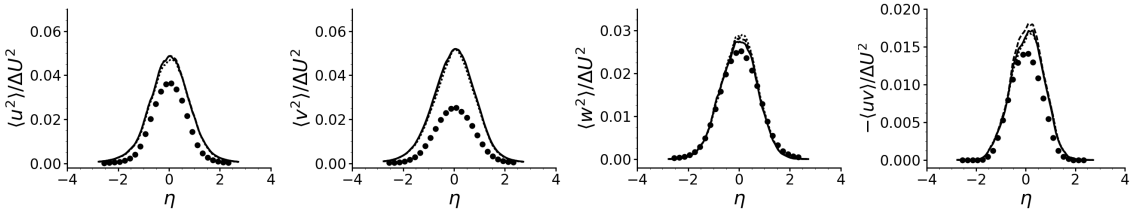

Figure 5.8: Reynolds stresses from Case III at $x/\delta_1 = 160$. Notations are the same as in Figure 5.5.

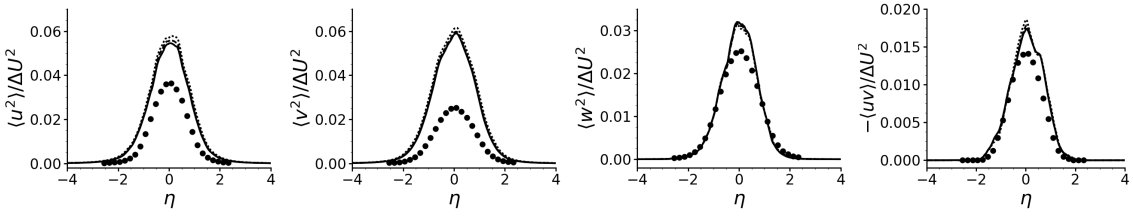

Figure 5.9: Reynolds stresses from Case IV at $x/\delta_1 = 160$. Notations are the same as in Figure 5.5.

5.4 Transverse dimension effects

To investigate influence of the domain transverse dimension on the flow solution, results of the Cases I-III simulations are compared in this subsection. In these cases, the domain dimension L_y increases from $50\delta_1$ in Case II to $90\delta_1$ in Case III, with $L_y = 70\delta_1$ in Case I being in the middle of the considered range The largest dimension, $90\delta_1$, corresponds to the size of the experimental test section in this direction., and to the L_y value in Cases IV-VI. The Cases II and III simulations started from the Case I solution at $t = 500$ as discussed in Section 4.3. The time of collecting statistics, the number of flow realizations used to compute them, and other

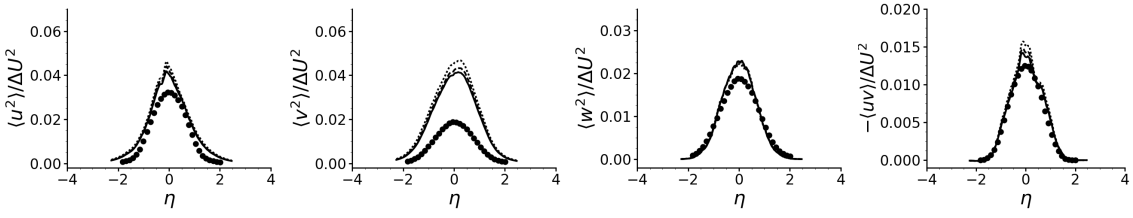

Figure 5.10: Reynolds stresses from Case IV at $x/\delta_1 = 320$. Notations are the same as in Figure 5.5.

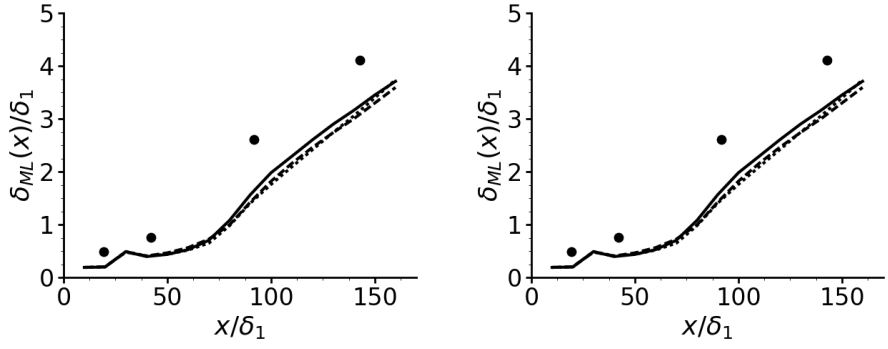

Figure 5.11: The mixing layer growth characterized by a) mixing layer thickness, b) momentum thickness. Notations: lines DNS data, circles experiment [10]. Line styles: Solid - Case I, dotted - Case II, dashed - Case III.

simulation parameters are the same in the three cases, including the other domain dimensions: $L_x = 170\delta_1$ and $L_z = 23.4\delta_1$.

The mixing layer growth obtained in the three cases is shown in Figure 5.11 by lines. Within the chosen range of L_y, the growth of the mixing layer appears to be unaffected by variations in the transverse dimension, demonstrated by overlapped dotted and dashed lines corresponding to the Cases II and III solutions. The difference between these two solutions and the Case I solution observed in Figure 5.11a indicates sensitivity of the simulation results to the difference in the initial conditions.

Profiles of the streamwise mean velocity at various locations in the streamwise direction: $x/\delta_1 = 10,\ 20,\ 30$, and 160, are unaffected by variation in the L_y-value and by the difference in initial conditions (Figure 5.12).

Streamwise evolution of the integrated normal Reynolds stresses is affected when the domain transverse dimension increases from $50\delta_1$(Case II) to $70\delta_1$ (Case I) (Figure 5.13). Their values are higher in the shorter domain of Case II. In the figure, $K = 0.5(K_x + K_y + K_z)$. Differences in the parameters obtained from different simulations appear when the mixing layer is already turbulent and they grow with x. The location of the flow transition to turbulent remains close to $x/\delta_1 = 15$ in the three cases. Further increase of L_y to $90\delta_1$ (Case III) has no effect on these statistics. Observed

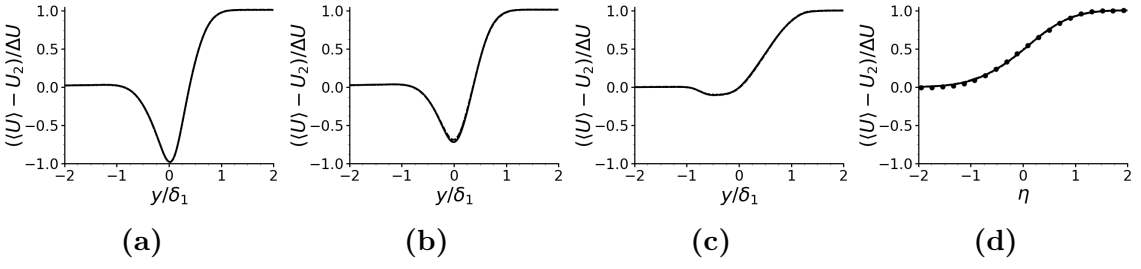

Figure 5.12: Mean velocity profiles at different streamwise locations: a) $x/\delta_1 = 10$**, b)** $x/\delta_1 = 20$**, c)** $x/\delta_1 = 30$**, d)** $x/\delta_1 = 160$ **(Cases I-III). Notations are the same as in Figure 5.11.**

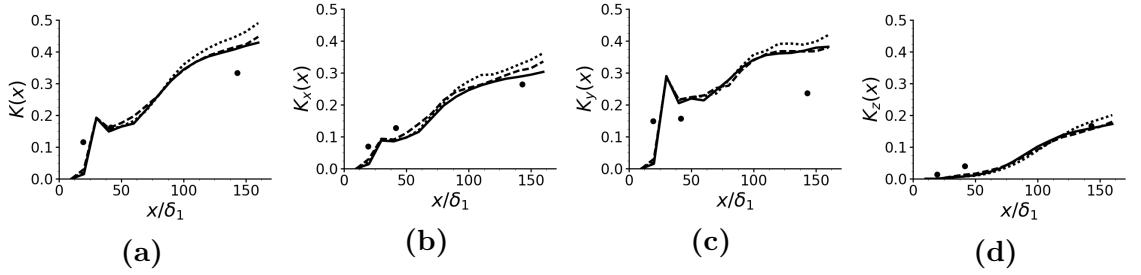

Figure 5.13: Streamwise evolution of the turbulent kinetic energy and the normal Reynolds stresses integrated across the mixing layer (Cases I-III). Notations are the same as in Figure 5.11.

changes in K_x can be attributed to the difference in the simulations initial conditions.

Comparison of the Reynolds stress profiles at various locations in the streamwise direction (Figure 5.14) confirms that the Case II domain dimension in the transverse direction in insufficient. All Reynolds stresses but $\langle v^2\rangle$ are affected within the range of $\pm 3\eta$ and particularly, closer to the domain exit at $x/\delta_1 \geq 143$. Comparing results for $\langle v^2\rangle$ on Figure 5.14 and K_y in Figure 5.13c, one can infer that there is more turbulent kinetic energy in the transverse direction outside the range $\pm 3\eta$ in the shorter domain.

The flow area near the splitter plate is mainly influenced by the difference in the simulations initial conditions. This is clear from comparing the Case I results with those from the other two cases. Instead of falling in between, results from Case I deviate from the group. The most affected Reynolds stress is $\langle u^2\rangle$, with the effect being noticeable through the entire mixing layer region. This is consistent with the

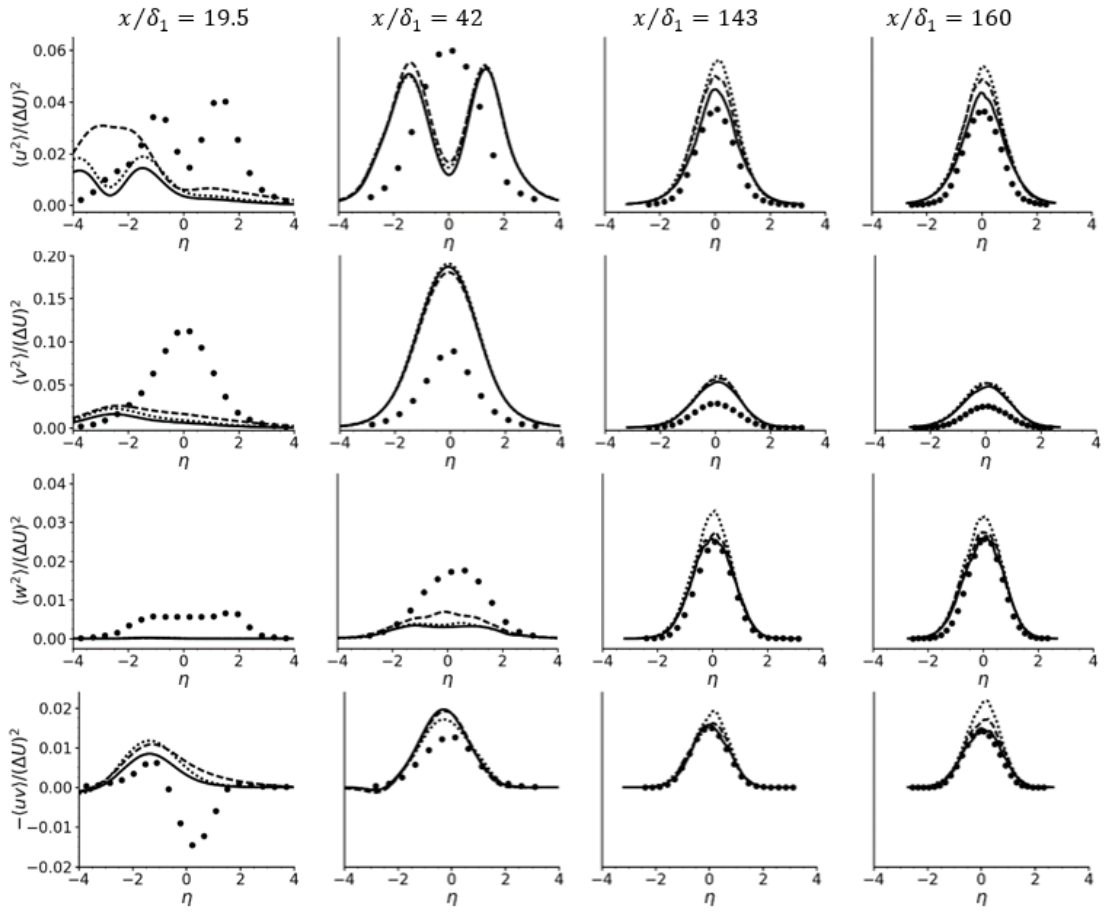

Figure 5.14: Profiles of the Reynolds stresses at different locations in the streamwise direction (Cases I-III). First row – $\langle u^2\rangle$, second row – $\langle v^2\rangle$, third row – $\langle w^2\rangle$, fourth row – $\langle uv\rangle$. Experimental data given for comparison with the simulation results at $x/\delta_1 = 160$ were obtained at the location of $x/\delta_1 = 195$. Notations are the same as in Figure 5.11.

results shown in Figure 5.13b for K_x.

In sum, results presented in this section show that for the given $L_x = 170\delta_1$ and $L_z = 23.4\delta_1$, the value $L_y = 50\delta_1$ is insufficient for the solution to be independent of the domain transverse dimension and has to be increased to $70\delta_1$. The insufficient domain dimension in this direction leads to increase in the maximum values of the Reynolds stresses, particularly of those in the plane normal to the transverse direction. As a result, one can expect the increased turbulence level when comparing with the solution independent from this domain dimension.

Table 5.3: Ratios used in criteria (5.7) and (5.8) to evaluate the domain transverse dimension.

	$L_y/\delta_{\omega,max}$	$\delta_{\omega,max}/\delta_1$	$L_y/\left(\delta_{ML}\right)_{max}$
Case I	11.25	6.22	18.85
Case II	8.03	6.05	14.23
Case III	14.75	6.14	25.02
Case IV ($x \leq 170\delta_1$)	13.84	6.55	23.9
Case IV ($x \leq 350\delta_1$)	5.91	15.34	10.47
Case V	11.73	7.73	21.7
Case VI	12.31	7.37	21.22
Case VII	12.69	5.84	21.31

When choosing the L_y-values for simulations, we followed recommendations from [4, 80]. In particular, this parameter is within the values used in such simulations:

$$6.96 < L_y/\delta_{\omega,max} < 8.3, \tag{5.7}$$

in Cases I-III (Table 5.3). It is also satisfied in Cases V-VII. In Case IV, with the longer streamwise direction, criterion (5.7) is only satisfied at $x/\delta_1 \leq 170$, but relaxed in the entire domain, which is unavoidable if one keeps the numerical domain dimensions within or equal to those of the experimental test section. However, results of our simulations show that criterion $x/\delta_1 \leq 170$ is not universal. From current results, a more reliable alternative is proposed:

$$L_y/\left(\delta_{ML}\right)_{max} \geq 17.5. \tag{5.8}$$

This criterion is violated in Case II, but is satisfied in Cases I and III (see Table 5.3). This criterion is again relaxed in Case IV, when applied to the entire domain.

Results from Cases I-III also show sensitivity of the Reynolds stress profiles (their maximum values) to the simulation initial conditions. The Reynolds stress $\langle u^2 \rangle$ is affected everywhere in the flow by the difference in the simulations initial conditions, whereas its effect on the other Reynolds stresses is mainly limited to the area near the splitter plate.

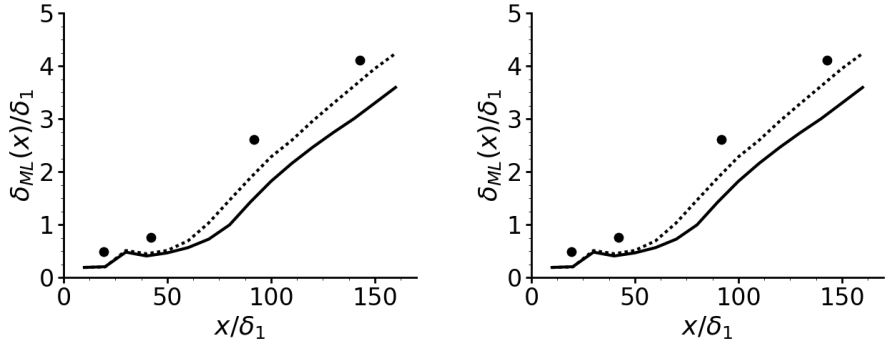

(a) **(b)**

Figure 5.15: The mixing layer growth characterized by a) mixing layer thickness, b) momentum thickness. Notations: lines DNS data, circles experiment [10]. Line styles: Solid - Case III, dotted - Case VI.

5.5 Grid effects

Results from the Cases III and VI simulations are used in this subsection to evaluate the grid effects. In these two cases, the domains are equivalent in the (x, y)-plane. In the spanwise direction, $L_z = 23.4\delta_1$ in Case III vs. $23.56\delta_1$ in Case VI. The Case VI grid is finer than the one used in Case III in the (x,y)-plane and particularly, in the splitter plate wake as described in Section 4.4. In the spanwise direction, the two domains have the same number of uniformly-distributed elements. The simulations run for the same time, and the same number of flow realization is used to collect statistics in both cases.

Figures 5.15-5.17 show that while the streamwise mean velocity profiles at various locations in the streamwise direction are essentially unaffected (Figure 5.16), the mixing layer growth and the integrated Reynolds stresses, with the exception of K_y, are influenced by changes in the grid. Differences become apparent at $x/\delta_1 \approx 50$ (Figures 5.15 and 5.17), after the flow becomes turbulent. At the same time, when analyzing the Reynolds stress profiles (Figure 5.18), the difference between the results obtained using different grids does not appear to be significant except for $\langle w^2 \rangle$ close to the domain exit.

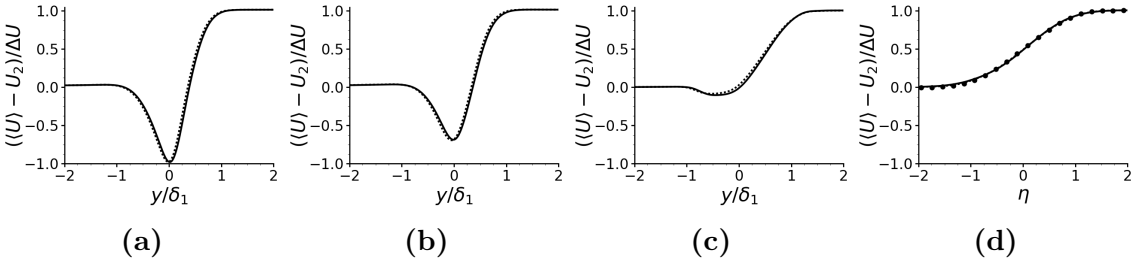

Figure 5.16: Mean velocity profiles at different streamwise locations: a) $x/\delta_1 = 10$, b) $x/\delta_1 = 20$, c) $x/\delta_1 = 30$, d) $x/\delta_1 = 160$ (Cases III and VI). Notations are the same as in Figure 5.15.

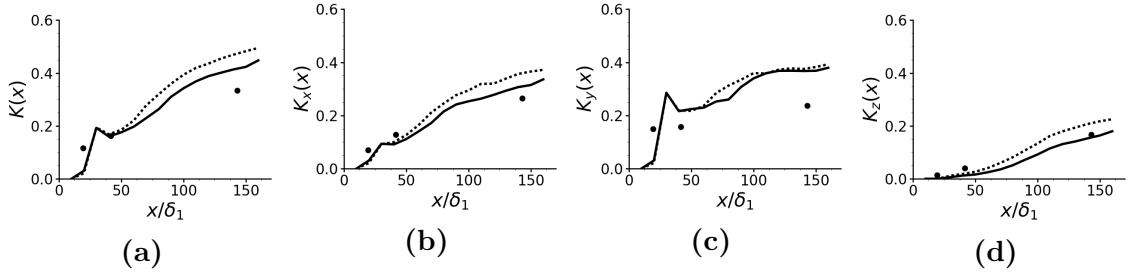

Figure 5.17: Streamwise evolution of the turbulent kinetic energy and the normal Reynolds stresses integrated across the mixing layer (Cases III and VI). Notations are the same as in Figure 5.15.

It is interesting to notice that simulations produce higher level of turbulence in the flow than in the experiment, but the mixing layer growth in Case VI agrees well with the experimental results. One of the possible reasons is that in the simulations, the Reynolds stresses in the stream- and spanwise directions are particularly high. Comparing Figures 5.17 and 5.18, one can also infer that the flow area outside the $\pm 3\eta$ range contributes substantially to the values of the integrated Reynolds stresses. This is an indication of the grid stretching in the transverse direction in particular, being a factor affecting the simulation results in both cases. Due to the current project time constraints, a comprehensive analysis of this and other grid effects is left for future studies.

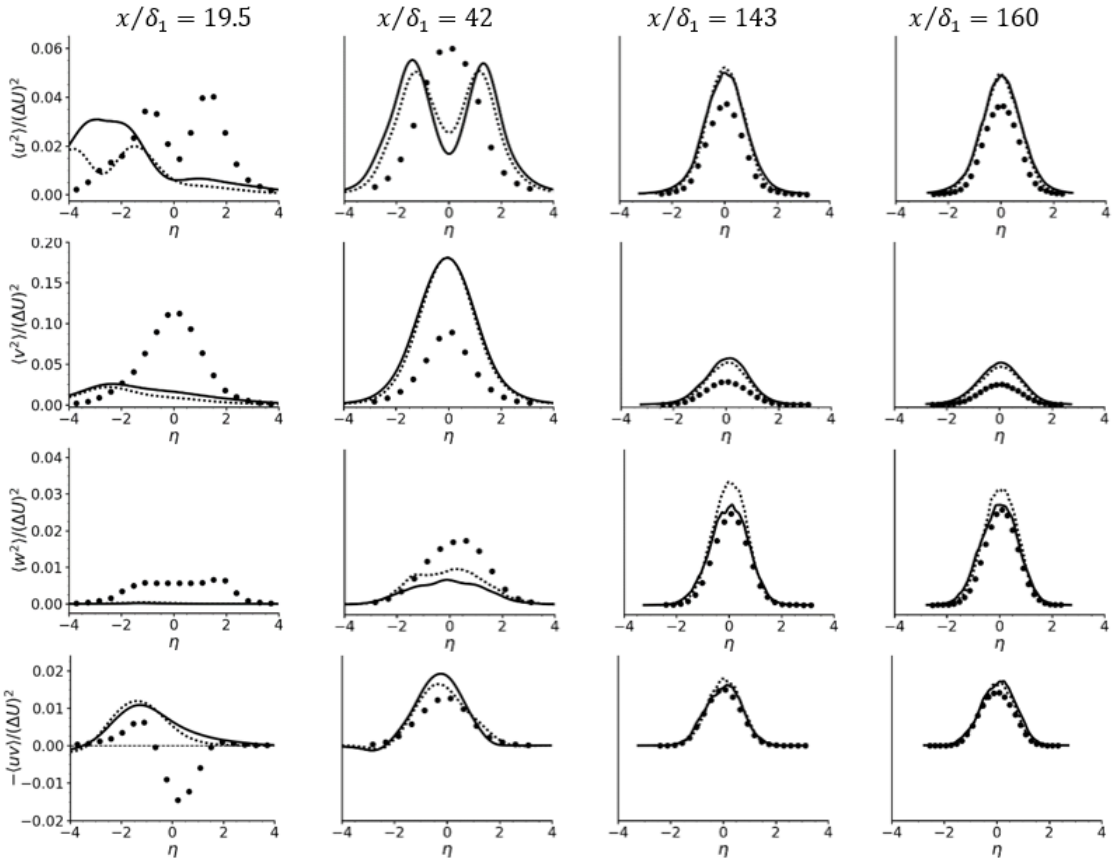

Figure 5.18: Profiles of the Reynolds stresses at different locations in the streamwise direction (Cases III and VI). First row – $\langle u^2\rangle$, second row – $\langle v^2\rangle$, third row – $\langle w^2\rangle$, fourth row – $\langle uv\rangle$. Experimental data given for comparison with the simulation results at $x/\delta_1 = 160$ were obtained at the location of $x/\delta_1 = 195$. Notations are the same as in Figure 5.15.

5.6 Spanwise dimension effects

In this subsection, results from the Cases V and VI simulations are used to analyze how the domain spanwise dimension affects the simulation results. The simulations parameters are the same in both cases except for L_z, which is $40\delta_1$ in Case V and $23.56\delta_1$ in Case VI. These values are about the order of magnitude smaller than in the experiments, where the test section dimension in this direction was $L_z = 227.5\delta_1$.

The mixing layer growth (Figure 5.19) and the streamwise mean velocity profiles (Figure 5.20) are unaffected by variation of the domain spanwise dimension. The

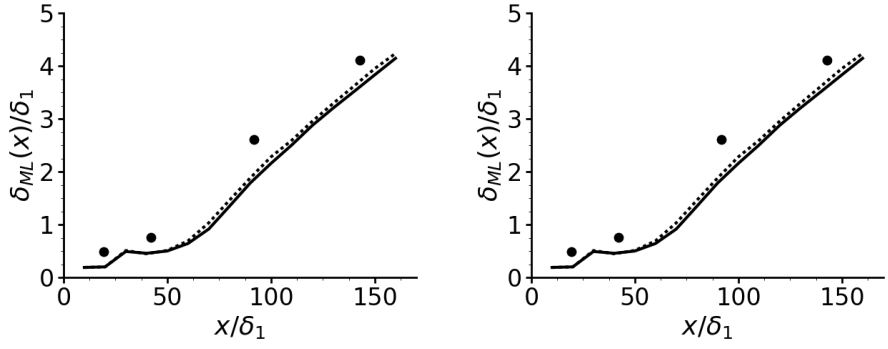

(a) **(b)**

Figure 5.19: The mixing layer growth characterized by a) mixing layer thickness, b) momentum thickness. Notations: lines DNS data, circles experiment [10]. Line styles: Solid - Case V, dotted - Case VI.

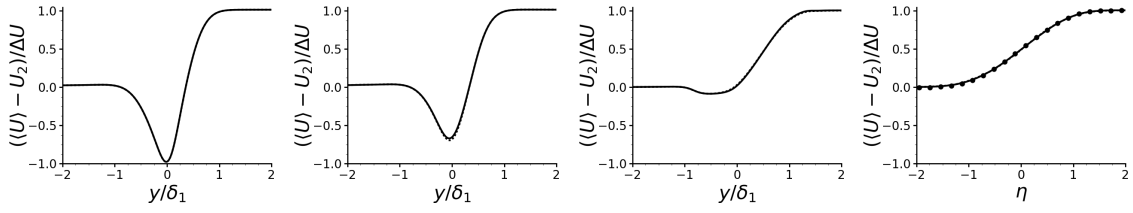

(a) **(b)** **(c)** **(d)**

Figure 5.20: Mean velocity profiles at different streamwise locations: a) $x/\delta_1 = 10$**, b)** $x/\delta_1 = 20$**, c)** $x/\delta_1 = 30$**, d)** $x/\delta_1 = 160$ **(Cases V and VI). Notations are the same as in Figure 5.19.**

effect on evolution of the integrated Reynolds stresses (Figure 5.21) is minor as well, with K_z being the mostly influenced integrated Reynolds stresses near the domain exit. Figure 5.22 confirms sensitivity of particularly $\langle w^2 \rangle$ close to the domain exit to variation of L_z. Its maximum value reduces with reducing the domain dimension in the spanwise direction. The maximum value of $\langle uv \rangle$ is also affected, but in a lesser degree and only close to the trailing edge of the splitter plate in the transitional region.

In a preliminary study conducted using simulations of mixing layers with an infinitely-thin splitter plate, results were similar to those in the current study with a thick plate. That is, from considered statistics, two Reynolds stresses were found to

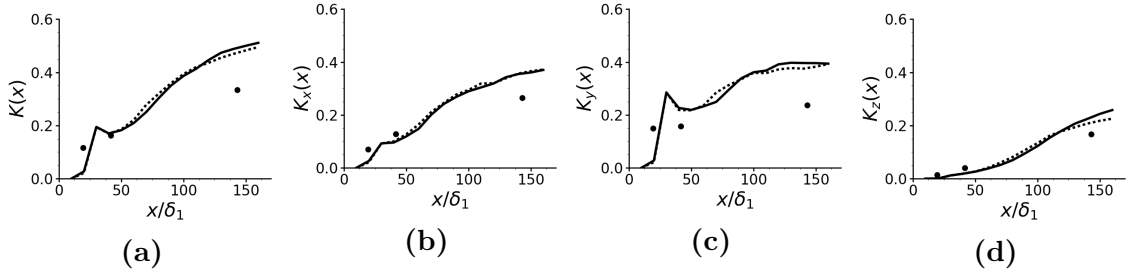

Figure 5.21: Streamwise evolution of the turbulent kinetic energy and the normal Reynolds stresses integrated across the mixing layer (Cases V and VI). Notations are the same as in Figure 5.19.

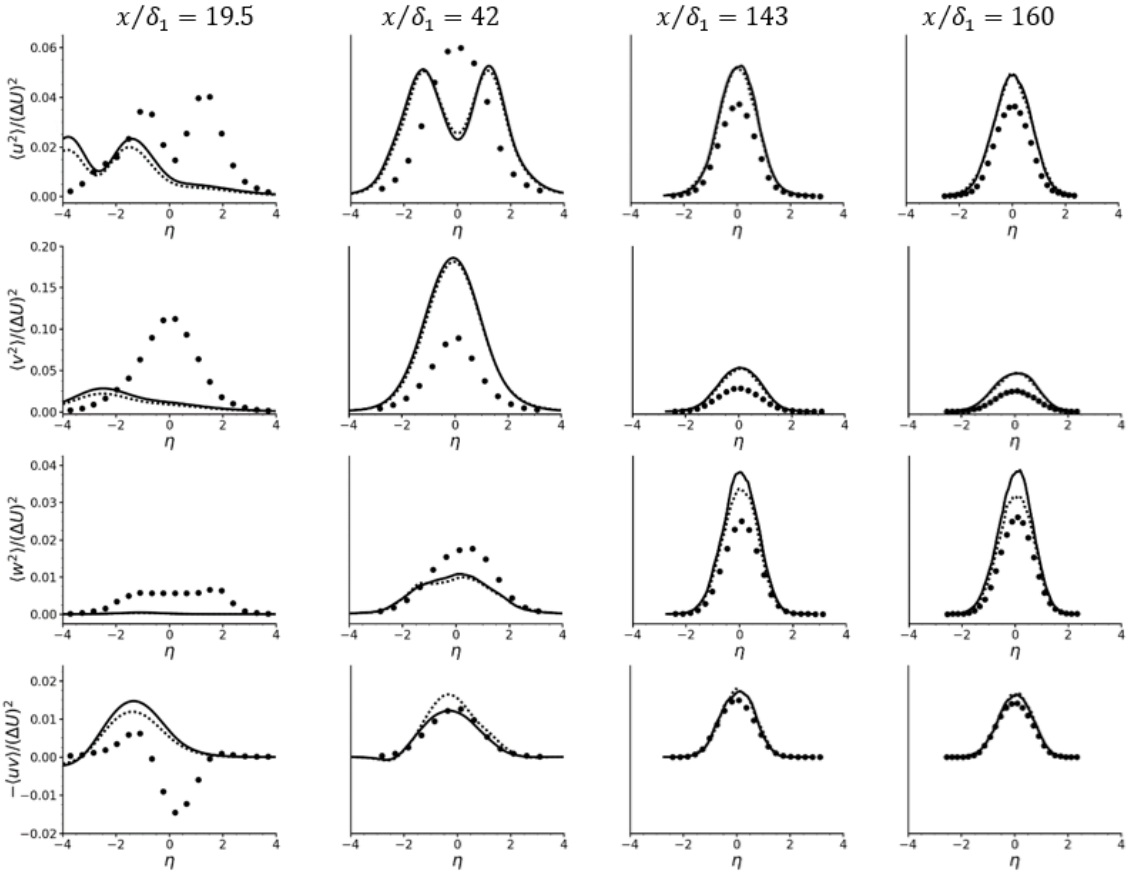

Figure 5.22: Profiles of the Reynolds stresses at different locations in the streamwise direction (Cases V and VI). First row – $\langle u^2 \rangle$, second row – $\langle v^2 \rangle$, third row – $\langle w^2 \rangle$, fourth row – $\langle uv \rangle$. Experimental data given for comparison with the simulation results at $x/\delta_1 = 160$ were obtained at the location of $x/\delta_1 = 195$. Notations are the same as in Figure 5.19.

Table 5.4: Ratios used in criterion (5.9) to evaluate the domain spanwise dimension.

	A
Case I	15.6
Case II	15.5
Case III	16.1
Case IV ($x \leq 170\delta_1$)	27.12
Case IV ($x \leq 350\delta_1$)	11.4
Case V	11.4
Case VI	24.7
Case VII	17.1

be affected: $\langle uv \rangle$, in all considered locations within the turbulent mixing layer, and $\langle w^2 \rangle$, in the area close to the domain

Overall, one can infer that effects of considered variation of the domain spanwise dimension on the statistics are negligible except for $\langle w^2 \rangle$ close to the domain exit. The splitter plate thickness has no significant influence on the observed effects.

The obtained results confirm applicability of the criterion

$$A = L_z/\theta_{max} > 10, \tag{5.9}$$

proposed in [48] for the flow to be independent of the domain size in this direction. The values of A in Cases V and VI, as well as in other cases are presented in Table 5.4.

5.7 Streamwise dimension effects

Results from the Cases IV and V simulations are compared in this subsection to analyze the impact of variation of the domain streamwise dimension or equivalently, of the domain exit location on the mixing layer development. In Case IV, the domain exit is located at $350\delta_1$ and in Case V, $L_x = 170\delta_1$. Therefore, all data are compared at $x/\delta_1 < 170$. For comparison, the size of the experimental test section in this direction was $915\delta_1$ [10]. The base grid used in the two cases is the same. However, longer simulation time and more individual flow realizations were required

in Case IV to achieve the statistics convergence comparable to that in Case V (see Section 5.3 for discussion). Parameters characterizing the mixing layer growth are shown in Figure 5.23. Solid and dashed lines correspond to Cases IV and V; symbols are experimental data. As the figure demonstrates, the effect from varying L_x is substantial. The mixing layer growth is suppressed in the longer domain (Case IV), with the parameters from the two cases starting to deviate from each other at $x/\delta_1 \sim 50$. Velocity profiles in Figure 5.24 provide an explanation for a faster growth of the mixing layer. Specifically, the wake effect of the splitter plate vanishes more rapidly in the shorter domain (Case V).That is, the flow mixing starts sooner than in Case IV. Far from the splitter plate, the typical mixing layer mean velocity profile is restored.

Increasing L_x also leads to a delayed transition to turbulence: at $x/\delta_1 \approx 25$ in Case IV and at $x/\delta_1 \approx 15$ in Case V. The ratio of these two values is practically the same as the ratio of the domain streamwise dimensions in the two cases. Once transition initiated, the integrated normal Reynolds stresses K_x and K_y (and the total turbulent kinetic energy K) grow similarly in both cases until $x/\delta_1 \sim 125$ (Figure 5.25). Then, these statistics continue to grow in Case IV, but slow down in Case V. This is an obvious effect of the flow proximity to the domain exit, which does not appear in the converged solution of Case IV. Somewhat similar effects in a lesser degree can be recognized in the K_x and K_y evolution, when the flow approaches the domain exit in the Case IV solution that is not fully converged (dotted lines in Figures 5.25a and 5.25b). The growth rate of K_z is consistently lower in Case IV than in Case V. There is no suppression of its growth in both cases (Figures 5.25c and 5.7c), when approaching the domain exit.

The Reynolds stress profiles shown in Figure 5.26 confirm conclusions made from the results presented in Figures 5.23-5.25. In particular, the transition to turbulence occurs sooner in Case V indicated by higher maximum values of $\langle u^2 \rangle$ and $\langle v^2 \rangle$ in the area close to the splitter plate. However, far away from the splitter plate, these Reynolds stresses are higher in Case IV. The Reynolds stress $\langle w^2 \rangle$ is higher in Case

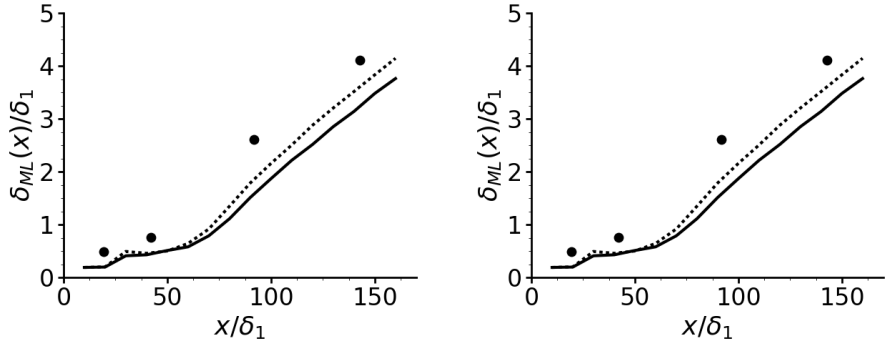

(a) **(b)**

Figure 5.23: The mixing layer growth characterized by a) mixing layer thickness, b) momentum thickness. Notations: lines DNS data, circles experiment [10]. Line styles: Solid - Case IV, dotted - Case V.

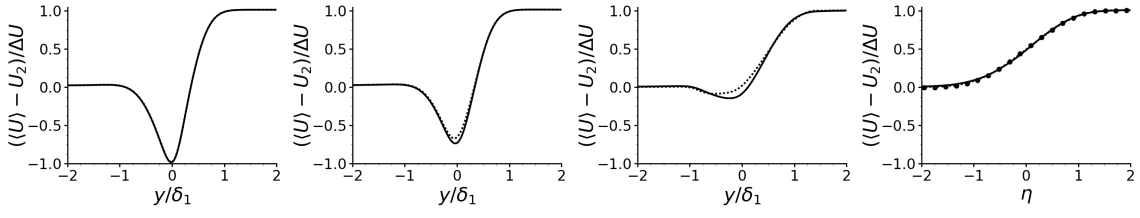

(a) **(b)** **(c)** **(d)**

Figure 5.24: Mean velocity profiles at different streamwise locations: a) $x/\delta_1 = 10$, b) $x/\delta_1 = 20$, c) $x/\delta_1 = 30$, d) $x/\delta_1 = 160$ (Cases IV and V). Notations are the same as in Figure 5.23.

V than in Case IV everywhere in the flow, where this statistics is presented. Interestingly, the shear stress is not affected by the domain streamwise dimension far away from the splitter plate, but is twice higher in Case V than in Case IV near the plate.

Overall, the domain dimension variation in the streamwise direction strongly affects all considered statistics. There could be multiple triggers for this effect, physical and numerical. For example, strong influence of the domain streamwise dimension on the mixing layer development was observed in the experiments [28], where it was suggested that large vortex structures near the experimental outlet boundary may be coupled to small structures upstream, producing a feedback mechanism between upstream and downstream flows. This makes the mixing layer structure and its de-

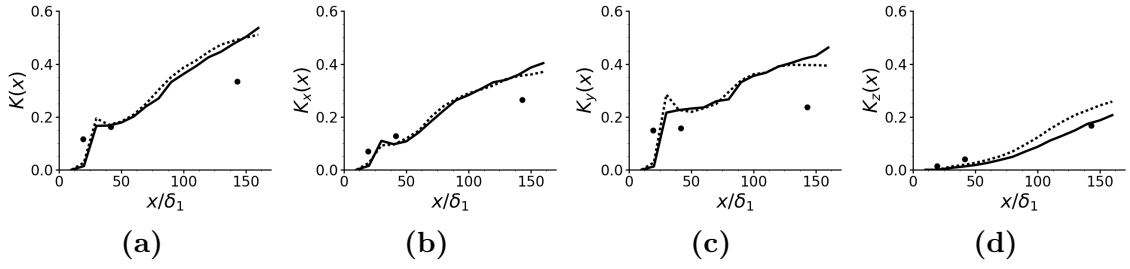

Figure 5.25: Streamwise evolution of the turbulent kinetic energy and the normal Reynolds stresses integrated across the mixing layer (Cases IV and V). Notations are the same as in Figure 5.23.

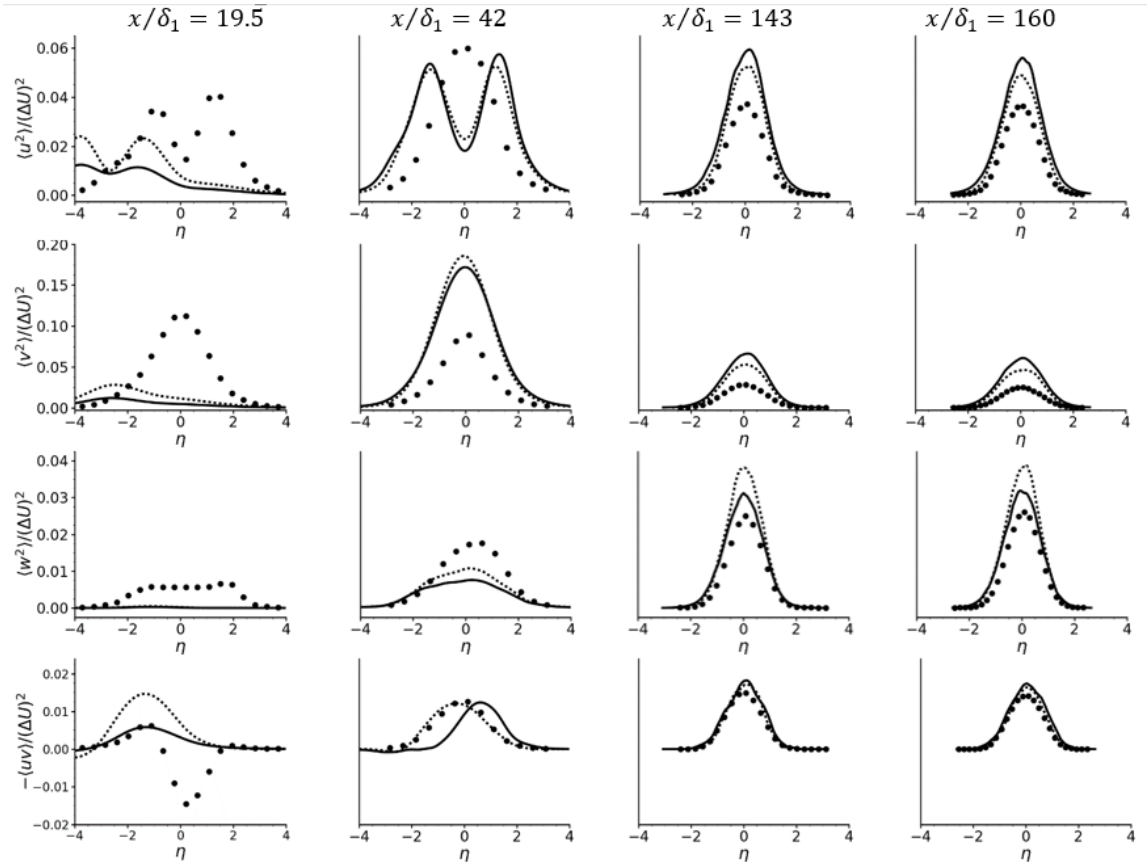

Figure 5.26: Profiles of the Reynolds stresses at different locations in the streamwise direction (Cases IV and V). First row – $\langle u^2\rangle$, second row – $\langle v^2\rangle$, third row – $\langle w^2\rangle$, fourth row – $\langle uv\rangle$. Experimental data given for comparison with the simulation results at $x/\delta_1 = 160$ were obtained at the location of $x/\delta_1 = 195$. Notations are the same as in Figure 5.23.

velopment dependent on the streamwise size of the experimental test section. Our data appear to support a possibility for such a phenomenon, but not all possible numerical causes were considered in the current study and thus, their effects cannot be eliminated. Among them are the outlet and the boundary conditions that may alter the mixing layer development. The grid effects: resolution near the domain exit and the grid stretching throughout the whole domain, in particular, have yet to be understood in full as mentioned above. In sum, with the current level of knowledge, it is unlikely to expect solutions to be independent of this simulation parameter.

5.8 Inflow boundary layer conditions

Preliminary simulations conducted using Case VII showed that inflow boundary layers on this domain were underdeveloped compared to experimental boundary layers (Table 5.2). Therefore, the development lengths on both streams were elongated resulting in the Case I domain. However, interesting results were obtained using Case VII domain, which will be presented in this and the following sections.

Results from simulations on Cases I and VII were compared to analyze sensitivity of the mixing layer development to the conditions of the laminar boundary layers at the trailing edge of the splitter plate. In Case I, these conditions are in a better agreement with the experimental data than in the Case VII simulations (Table 5.2). It means in particular that the boundary layers are faster in Case I.

The mixing layer thickness and its momentum thickness are shown in Figure 5.27. In the figure, solid lines correspond to Case I and dotted lines to Case VII; symbols are experimental data. Similar notations are used in the following figures of this sub-section. The mixing layer growth rate obtained at $x/\delta_1 > 70$ in Case I is the same as in the experiments. In the area closer to the slitter plate, a difference in the boundary layer conditions in two cases has little effect on the boundary layers mixing, which is slower than in the experiments. The opposite tendency is observed in the mean velocity (Figure 5.28). A difference in the boundary layers velocities in Cases

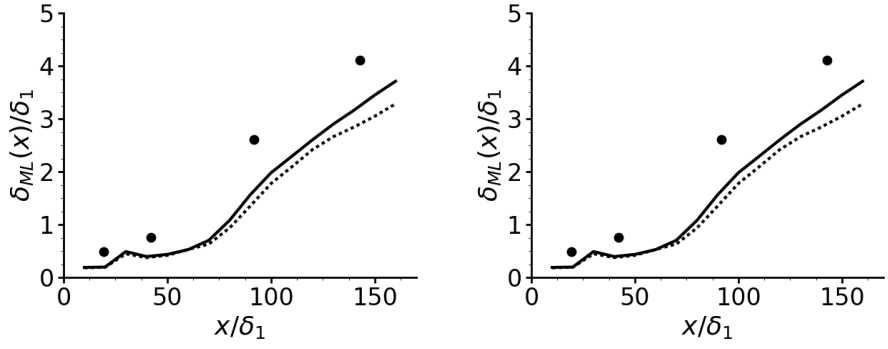

(a) **(b)**

Figure 5.27: The mixing layer growth characterized by a) mixing layer thickness, b) momentum thickness. Notations: lines DNS data, circles experiment [10]. Line styles: Solid - Case I, dotted - Case VII.

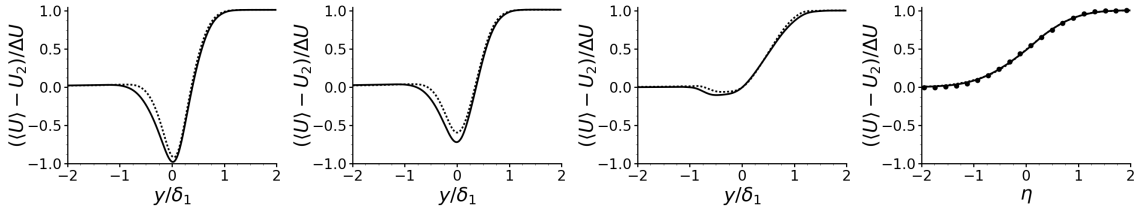

(a) **(b)** **(c)** **(d)**

Figure 5.28: Mean velocity profiles at different streamwise locations: a) $x/\delta_1 = 10$, b) $x/\delta_1 = 20$, c) $x/\delta_1 = 30$, d) $x/\delta_1 = 160$ (Cases I and VII). Notations are the same as in Figure 5.27.

I and VII is apparent in the splitter plate vicinity, but disappears far downstream from the plate.

Faster boundary layers in the Case I simulations increase the level of the turbulent kinetic energy and all of the normal Reynolds stresses integrated across the mixing layer (Figure 5.29). The values of K, K_x, and K_y are also higher than in the experiments everywhere in the flow except at $x/\delta_1 < 20$ in this case. The value of K_z is close to zero in this area and is not affected by the inflow conditions. The transition location to turbulence is also insensitive to considered variations in the boundary layer conditions.

The Reynolds stress profiles are shown in Figure 5.30. The figure confirms results

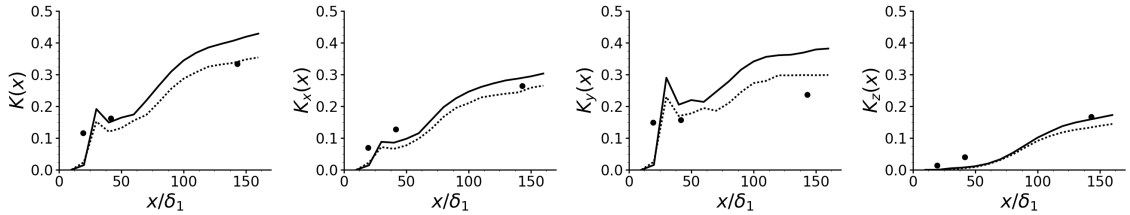

Figure 5.29: Streamwise evolution of the turbulent kinetic energy and the normal Reynolds stresses integrated across the mixing layer (Cases I and VII). Notations are the same as in Figure 5.27.

for the integrated characteristics presented in Figure 5.29. That is, the Reynolds stresses are slightly higher in the Case I simulation everywhere in the flow except for the area closest to the splitter plate. In this area, $x/\delta_1 < 20$, slower boundary layers in Case VII mix more efficiently, whereas faster boundary layers in Case I "slip" over each other until they slow down farther downstream. The simulated flow structure obtained in both Cases is different from that of observed in the experimental flow close to the splitter plate. Far away from the splitter plate, the effect from the boundary conditions is still present, but less significant.

5.9 Time step

In this section, influence of the time step in the temporal discretization scheme on the DNS results is discussed. For this analysis, simulations were conducted with two different time steps $\Delta t_1 = 0.012$ and $\Delta t_2 = 0.02$ using the computational domain and the grid for Case VII. With these time steps, the CFL values are 0.45 and 0.75, respectively. That is, the traditional stability criterion for the corresponding explicit scheme of the same order of accuracy in Nek5000, BDF3/EXT3, $CFL = 0.5$, is satisfied with Δt_1, but not with Δt_2. The OIFS scheme in Nek5000 permits such simulations and as a result, the simulation cost can be substantially reduced. On the other hand, some of smaller scales may be filtered in the process, which, depending on the filtered scales origin, physical or numerical, may or may not be beneficial for

the quality of simulation results.

Figure 5.31 compares the mixing layer thickness and its momentum thickness obtained at the two time steps. In the figure, dotted and solid lines correspond to Δt_1 and Δt_2, respectively. Experimental data are shown by circles. The figure demonstrates that the time step affects both parameters far downstream from the splitter plate, with the mixing layer growth obtained with the smaller time step being closer to the experimental data. Mean velocity profiles at four streamwise locations downstream the splitter plate are shown in Figure 5.32. In the experiments, the mean velocity profiles from different experimental sections including those close to the splitter plate collapse on the error function shown in Figure 5.32d, which is indicative of the boundary layers mixing very close to the plate trailing edge. In the simulations, the mixing is delayed, regardless the time step used. Far away from the splitter plate, the mean velocity profiles obtained with the different time steps are in agreement with the experimental data. Overall, the time step has insignificant effect on the mean velocity evolution.

Streamwise evolution of the turbulent kinetic energy and the normal Reynolds stresses, all integrated across the mixing layer, is shown in Figure 5.33. The figure demonstrates that transition to turbulence starts at $x/\delta_1 \sim 15$ in the simulations with both time steps. That is, the time step does not affect the transition location. Influence of the time step on the integrated turbulent kinetic energy and its contribution from the streamwise velocity fluctuations becomes apparent at $x/\delta_1 > 125$. The Reynolds stresses in the transverse and spanwise directions are affected everywhere in the flow: K_y is increased and K_z is reduced in simulations with the larger time step. This indicates that the scales filtered by the larger time step are responsible for the energy transfer to the spanwise velocity fluctuations. In the absence of these scales, the energy is re-directed to velocity fluctuations in the transverse direction. At $x/\delta_1 > 125$, the larger time step leads to reduced energy in velocity fluctuations in both directions tangential to the splitter plate plane: K_x and K_z, and in the turbulent kinetic energy K. The effect is beneficial for K and K_x when comparing

with the experiments, but reduced turbulent kinetic energy may be a cause of the reduced growth of the mixing layer growth seen in Figure 5.31 in simulations with Δt_2.

The simulation time step affects all non-zero Reynolds stresses (Figure 5.34, but particularly, $\langle w^2 \rangle$. A difference in the profiles obtained with different time steps reduces as the mixing layer grows. Results for all Reynolds stresses but $\langle v^2 \rangle$ tend to agree with the experimental data far downstream from the splitter plate in the simulations with the larger time step. The Reynolds stress in the transverse direction is over-predicted everywhere in the flow with both time steps.

Results show that a choice of the time step affects the mixing layer development and its structure. However, its effect on the considered flow characteristics varies. The most affected ones are those relevant to the energy re-distribution in the transverse and spanwise flow directions, with the larger time step suppressing the energy transfer in the spanwise direction and promoting it in the transverse direction. As the mixing layer grows and become fully turbulent, the time step effect on the Reynolds stress profiles diminishes. The total turbulent kinetic energy in the flow is reduced far away from the splitter plate in the simulations with the larger time step. The implication of such results is that while numerical results were not independent of time step size, the overall behavior of evaluated turbulence statistics was improved with the larger time step size when compared against experimental data, meaning that the time step size used in preceding sections was appropriate to produce physically meaningful results.

5.10 Splitter plate thickness

The effect of the splitter plate thickness is assessed in this section. For this purpose, A special grid was created based on Case VII. In the new grid, the splitter plate thickness was set to zero and the elements which were directly downstream of the plate were removed. The high-speed and low-speed boundary layers are adjacent

to each other in this case. The upper half of the domain ($y > 0$) was re-meshed using the same number of elements and growth-rates as in Case VII, resulting in Δy values that differ by less than 1% from those listed in Table 4.3 for zones A-H (Figure 4.2). Hereafter, the original Case VII grid and geometry will be referred to as **Case VII.A**, while the modified version with infinitely thin plate is referred to as **Case VII.B**. Both cases used $\Delta t = 0.012$.

The grids for both cases near the trailing edge of the splitter plate are shown on Figure 5.35. In Case VII.B, the splitter plate is introduced by imposing the no-slip boundary condition at $y = 0$ for $x < 0$. Grid for Case VII.B has 79800 elements.

Case VII.B required longer sampling time for statistics to converge to acceptable levels, compared to other cases presented in Section 5.2. Therefore, $N_s = 504$ was used for both simulations, with extended sampling period

$$T = [500, 2400].$$

Boundary layer parameters at the plate's trailing edge in both cases are the same (Case VII in Table 5.2).

Numerical results for mixing layer thickness and momentum thickness are below experimental values in both cases (Figure 5.36), but Case VII.A is in better agreement with experimental data, with the shear layer being thicker than in Case VII.B. Mean velocity profiles in Figure 5.37 were also affected by the finite plate, particularly near the splitter plate trailing edge, where the wake deficit vanished more rapidly downstream of the thick plate. The wake deficit was not as significant in experimental results from [10], therefore, it is clear that the thick splitter plate plays a role in accelerating the transition from boundary layer velocity profile to the shear layer profile. The typical shear layer mean velocity profile is recovered in both cases further downstream (Figure 5.37d).

Turbulent kinetic energy and Reynolds stress integrated across the mixing layer indicate that transition is delayed with the thin plate, with values remaining close to zero in Case VII.B up to $x/\delta_1 \approx 42$, compared to Case VII.A, which becomes non-

zero at $x/\delta_1 \approx 20$ (Figure 5.38). Further downstream, the growth rate of quantities K_x, K_y and K is higher for Case VII.B than in Case VII.A, with the latter case being closer to experimental data. Values of K_z are lower for Case VII.B, but Case VII.A results are in closer agreement with wind tunnel data. Reynolds stress profiles (Figure 5.39) confirm that the flow in Case VII.B is laminar at $x/\delta_1 < 42$. Close to the outflow boundary, peak values of $\langle u^2 \rangle$ and $\langle v^2 \rangle$ are considerably larger in Case VII.B versus Case VII.A, while profiles of $\langle w^2 \rangle$ are lower lower in the former case. Levels of $\langle uv \rangle$ are similar in both cases. For all Reynolds stresses, Case VII.A results are considerably closer to experimental data than Case VII.B.

Flow visualization using iso-surfaces of the λ_2-criterion (Figure 5.40), introduced in [34], show the coherent flow structures in Cases VII.A and VII.B. The large structures observed in figure are large-scale laminar vortex structures of spanwise vorticity. On the top figure, these structures appear at $x/\delta_1 \approx 10$ and are broken down by streamwise vortices appearing at around $x/\delta_1 = 40$, which creates small-scale turbulent structures further downstream. In the bottom figure (Case VII.B), the appearance of large-scale structures is delayed until $x/\delta_1 \approx 30$ and the flow never turns fully turbulent, but shows scattered spots of "turbulence", characterized by the presence of streamwise vortices. These images are consistent with findings from turbulence statistics, in the sense that the case with a thick plate produced more three-dimensional flow, where large spanwise vortices have broken down to small turbulent structures, while the thin plate produces a flow which is predominantly laminar with the intermittent occurrence of turbulent spots. The different nature of both flows explains the difference in growth rates (Figure 5.36) and distribution of turbulent kinetic energy (Figure 5.38).

According to experiments conducted by Dziomba & Fiedler [29], splitter plate thickness, h, has negligible effect on the mixing layer when this parameter is below 50% of the combined displacement thicknesses of the inflow boundary layers. This condition is satisfied in current simulations. However, numerical results show that the infinitely thin splitter plate represents a special case, with splitter plate thickness

playing a significant role in triggering transition and the distribution of energy among the different components of velocity fluctuations. The thin plate generates a more two-dimensional mixing layer, with most of the energy being transferred to planar components of velocity and suppresses spanwise fluctuations, while the thick splitter plate produces a more three-dimensional flow which, according to statistics evaluated in this section, is more representative of the mixing layer in wind tunnel experiments. Current results are in agreement with numerical [40] and experimental results [14] where the effect of the shape of the splitter plate trailing edge on the mixing layer was analyzed. A thick splitter plate with a blunt trailing edge produced self-excited turbulence while a beveled plate with a thin trailing edge produce a more two-dimensional flow. In such studies, however, the thickness of the plate was large relative to the thickness of the inflow boundary layers. Therefore, results presented in this paper support the notion that having a splitter plate with finite thickness, no matter how small, is beneficial for triggering self-excited turbulence which is generated in wind tunnels due to the non-zero thickness in experiments, since it is not possible to produce an infinitely thin plate physically.

Comparing the impacts of all simulation parameters considered in the work, variation of the domain streamwise direction and splitter plate thickness had the strongest effect, which influence all considered statistics including the mean velocity profiles. Next in line is the solution response to the grid changes, based on the strength of their impact and the number of affected statistics. A perspective of obtaining the solution independent of these parameters in this flow geometry requires further studies and currently, is unlikely. Initial conditions are also a factor to consider unless all simulations start from the fixed laminar solution. On the other hand, effects from the domain spanwise and transverse dimensions, as well as time step size and boundary layer parameters at the trailing edge of the plate, are easier to control to obtain the solution independent of these parameters.

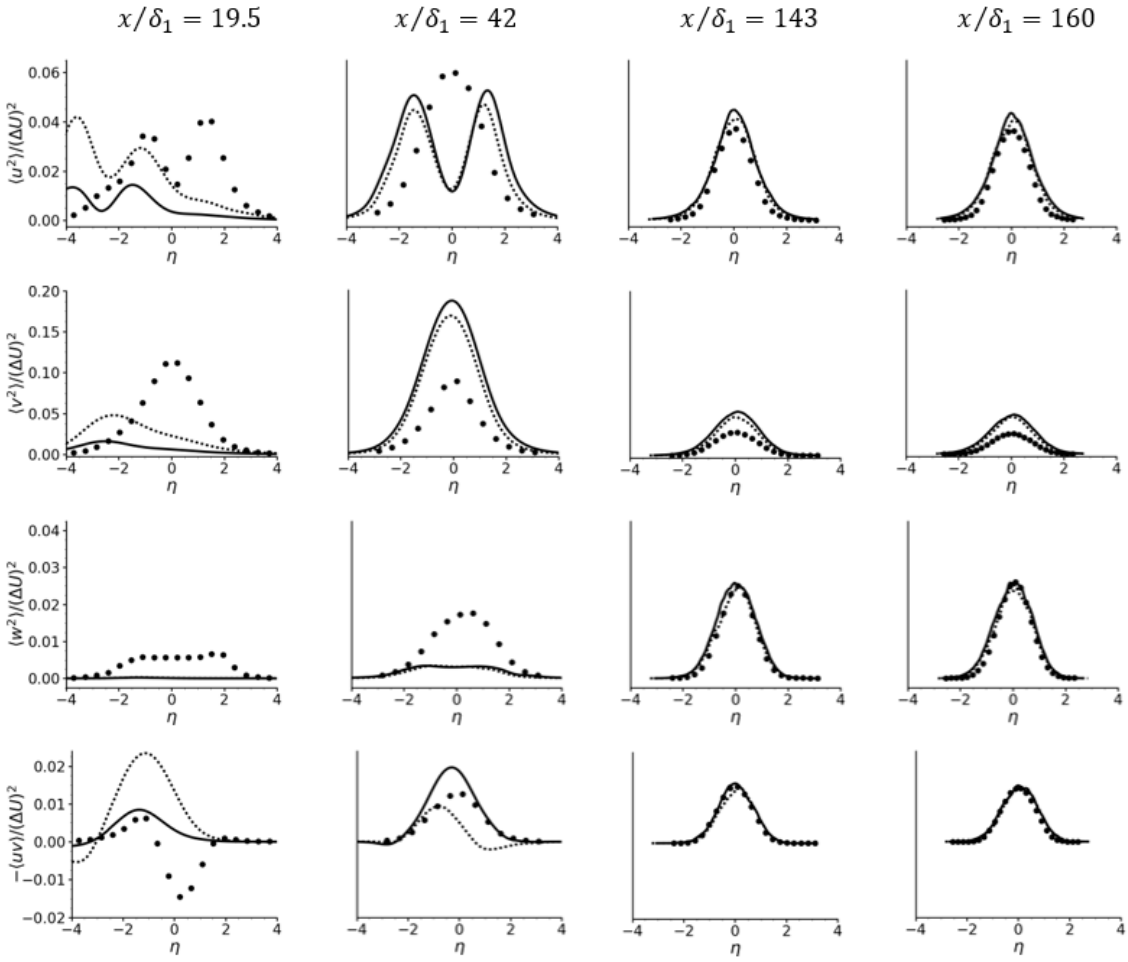

Figure 5.30: Profiles of the Reynolds stresses at different locations in the streamwise direction (Cases I and VII). First row – $\langle u^2 \rangle$, second row – $\langle v^2 \rangle$, third row – $\langle w^2 \rangle$, fourth row – $\langle uv \rangle$. Experimental data given for comparison with the simulation results at $x/\delta_1 = 160$ were obtained at the location of $x/\delta_1 = 195$. Notations are the same as in Figure 5.27.

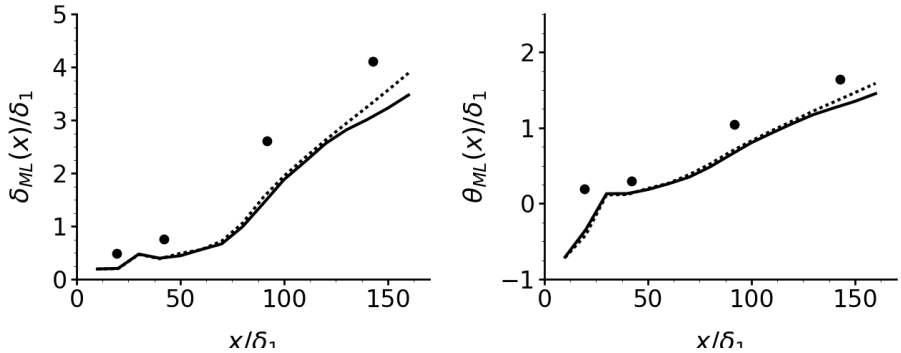

(a) (b)

Figure 5.31: The mixing layer growth characterized by a) mixing layer thickness, b) momentum thickness. Notations: lines DNS data from Case VII, circles experiment [10]. Line styles: dotted - Δt_1, solid - Δt_2.

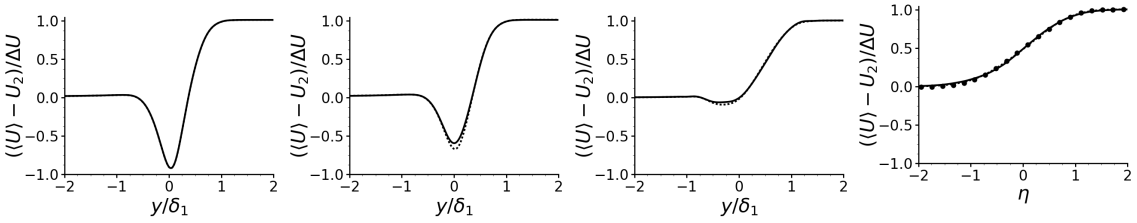

(a) (b) (c) (d)

Figure 5.32: Mean velocity profiles at different streamwise locations: a) $x/\delta_1 = 10$, b) $x/\delta_1 = 20$, c) $x/\delta_1 = 30$, d) $x/\delta_1 = 160$ (Case VII). Notations are the same as in Figure 5.31.

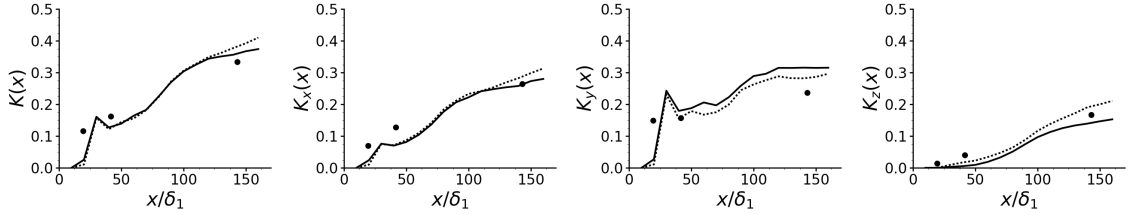

(a) (b) (c) (d)

Figure 5.33: Streamwise evolution of the turbulent kinetic energy and the normal Reynolds stresses integrated across the mixing layer (Case VII). Notations are the same as in Figure 5.31.

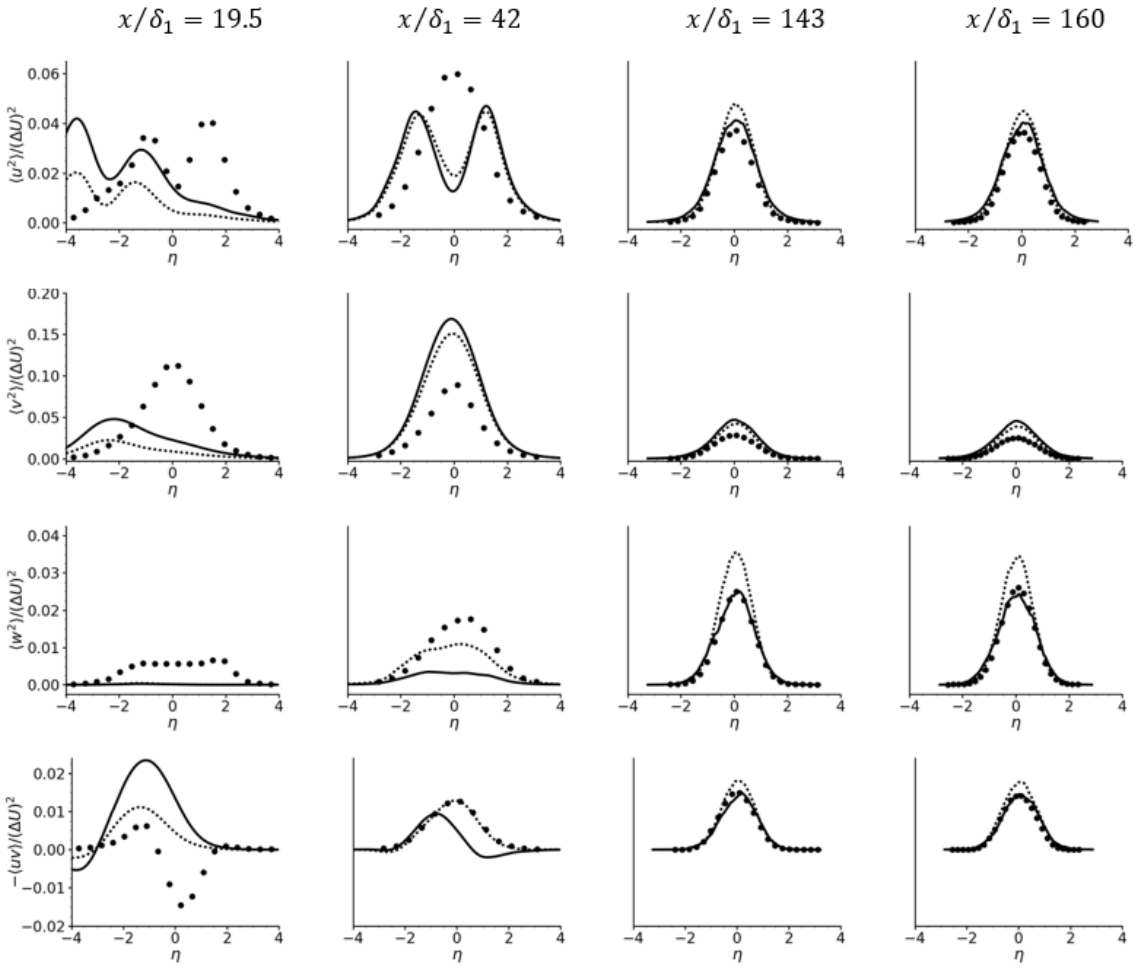

Figure 5.34: Profiles of the Reynolds stresses at different locations in the streamwise direction (Case VII). First row – $\langle u^2 \rangle$, second row – $\langle v^2 \rangle$, third row – $\langle w^2 \rangle$, fourth row – $\langle uv \rangle$. Experimental data given for comparison with the simulation results at $x/\delta_1 = 160$ were obtained at the location of $x/\delta_1 = 195$. Notations are the same as in Figure 5.31.

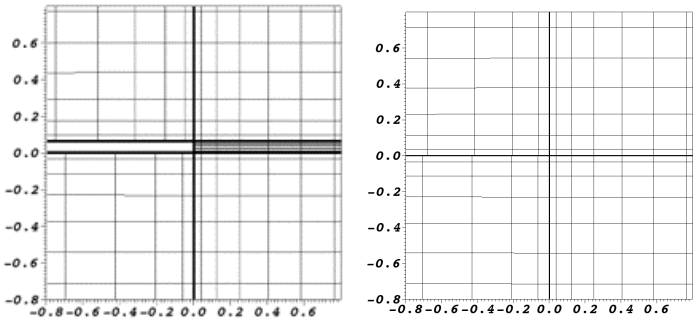

(a) (b)

Figure 5.35: Spectral element grid (thick lines) and quadrature points (intersection of thin lines) near the trailing edge of the plate in the base grids for a) Case VII.A and b) Case VII.B.

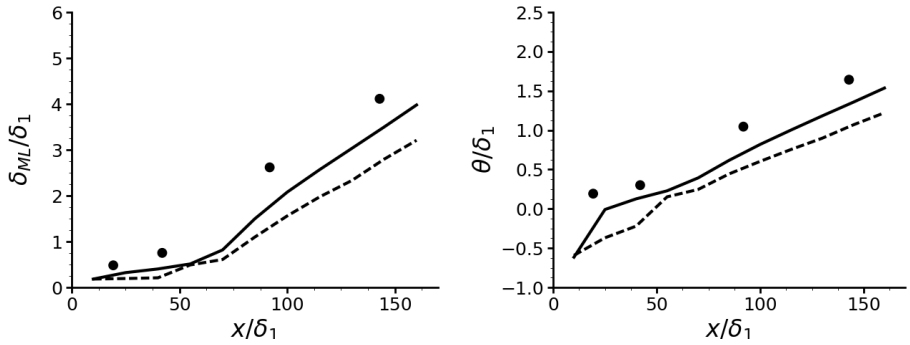

(a) (b)

Figure 5.36: The mixing layer growth characterized by a) mixing layer thickness, b) momentum thickness. Notations: lines DNS data, circles experiment [10]. Line styles: solid - Case VII.A, dashed - Case VII.B.

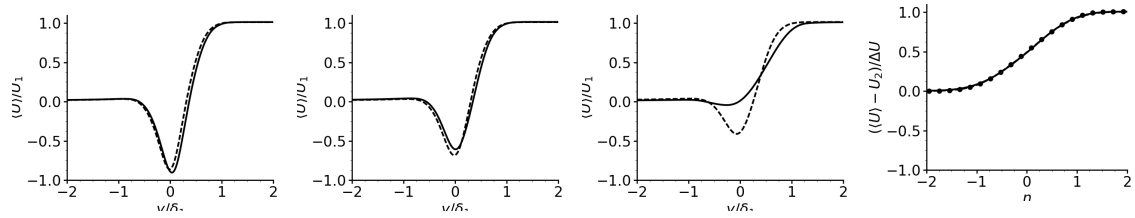

(a) (b) (c) (d)

Figure 5.37: Mean velocity profiles at different streamwise locations: a) $x/\delta_1 = 10$, b) $x/\delta_1 = 20$, c) $x/\delta_1 = 30$, d) $x/\delta_1 = 160$ (Case VII with thin and thick plate). Notations are the same as in Figure 5.36.

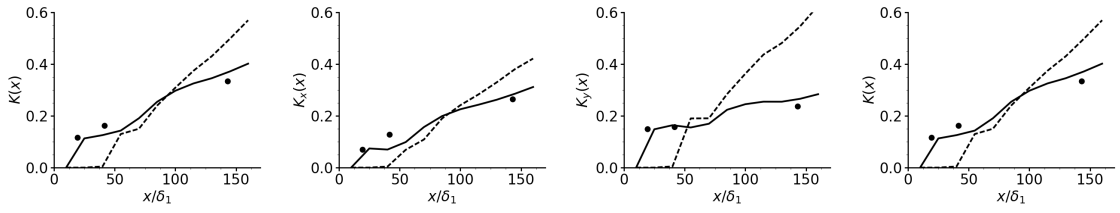

Figure 5.38: Streamwise evolution of the turbulent kinetic energy and the normal Reynolds stresses integrated across the mixing layer (Case VII with thin and thick plate). Notations are the same as in Figure 5.36.

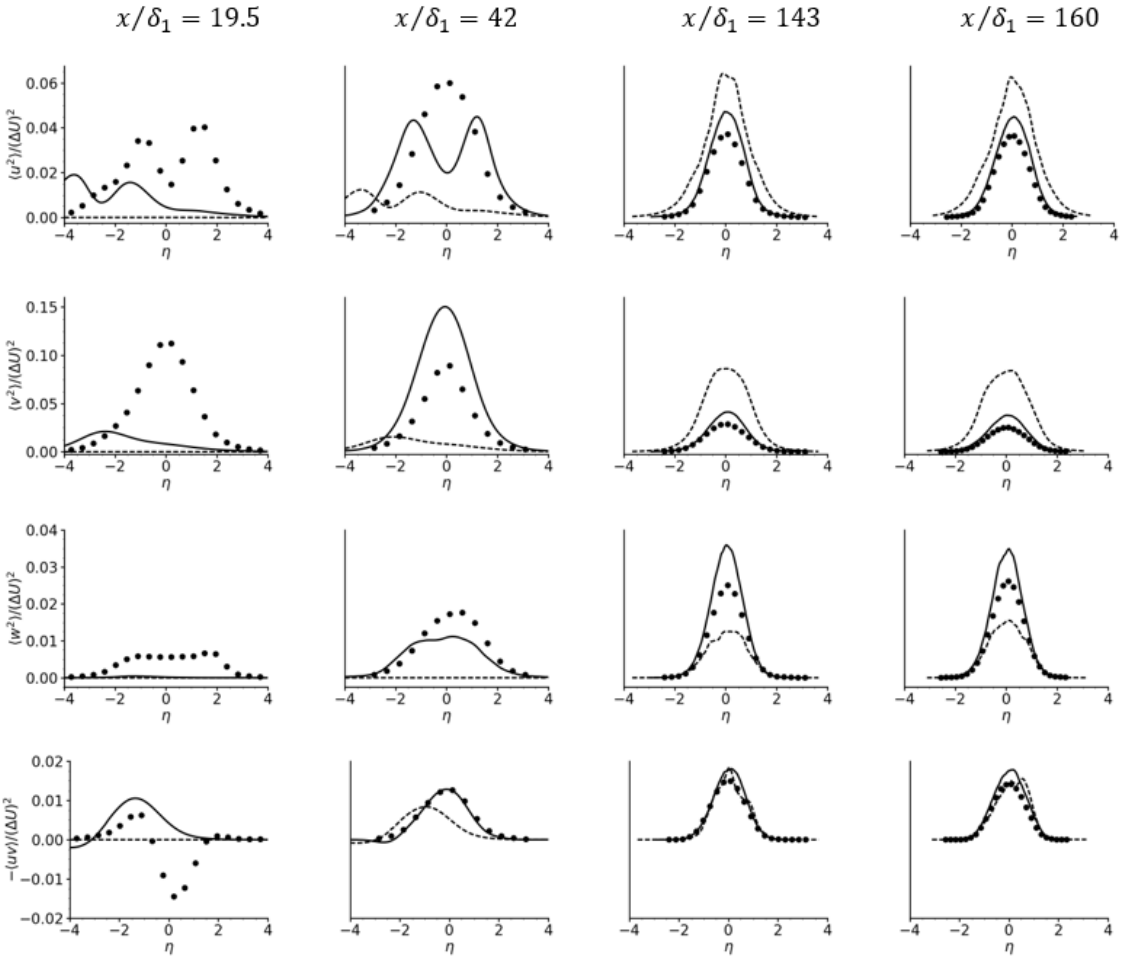

Figure 5.39: Profiles of the Reynolds stresses at different locations in the streamwise direction (Case VII with thin and thick plate). First row – $\langle u^2 \rangle$, second row – $\langle v^2 \rangle$, third row – $\langle w^2 \rangle$, fourth row – $\langle uv \rangle$. Experimental data given for comparison with the simulation results at $x/\delta_1 = 160$ were obtained at the location of $x/\delta_1 = 195$. Notations are the same as in Figure 5.36.

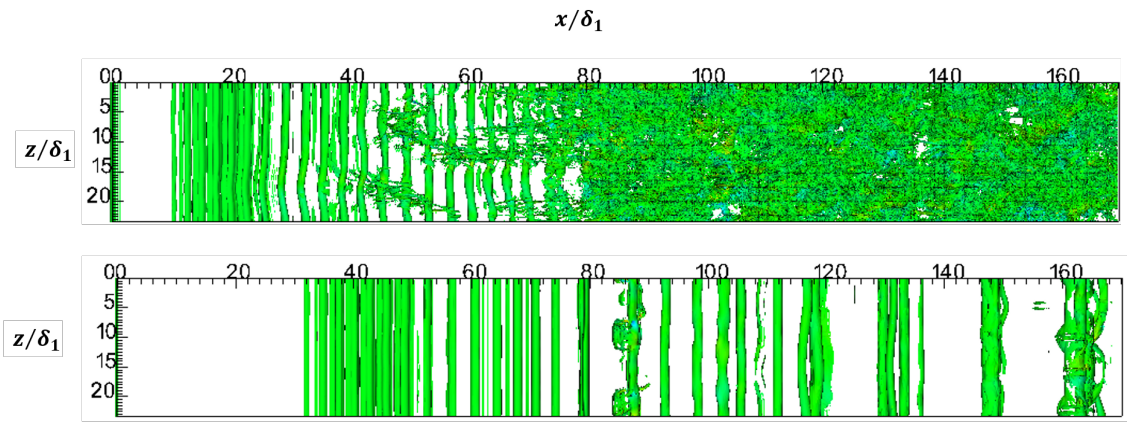

Figure 5.40: Flow visualization of vortex structures in the mixing layer using iso-surfaces of λ_2-criterion, colored by instantaneous spanwise velocity, W. View normal to the $x-z$ plane. Top – Case VII.A, bottom – Case VII.B.

Chapter 6

Mixing Layer Turbulence Statistics

The mean flow statistics of the turbulent mixing layer generated from Case IV simulations, described in Chapter 4, are presented in this chapter. Turbulence statistics considered are mean velocity field, Reynolds stresses (second-order moments), velocity moments up to fifth order and budget terms from transport equations of Reynolds stresses. Only moments necessary to solve the transport equations of the planar flow are presented. Such statistics provide a full description of the turbulent flow.

Statistics presented in this chapter were computed from "on-the-fly" statistics, meaning that statistical samples were taken at every time step, with Equation (2.4) equivalent to a time average using the trapezoidal rule for integration in time, where the time average is given by:

$$\langle Q \rangle_T = \frac{1}{T} \int_0^T Q(t) dt. \tag{6.1}$$

The non-dimensional time interval used to gather statistics was

$$\Delta T = [2530, 13130],$$

for a total period of $T = 10,600$ or $24.23\tau_f$. With a time step of $\Delta t = 0.02$, a total of 530,000 time steps or equivalently statistical samples were used. Spanwise averaging (Equation (2.5)) was also applied to statistics. This procedure yielded well-converged velocity moments up to fifth order.

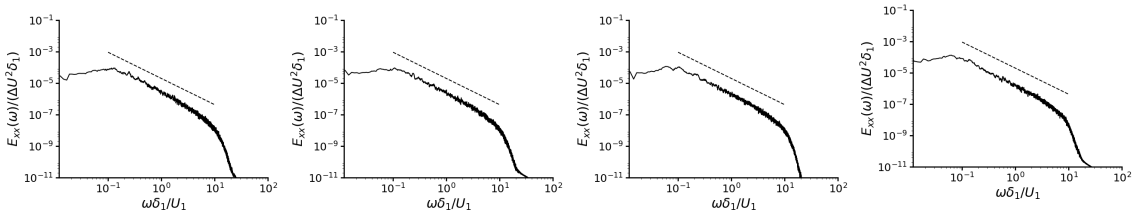

Figure 6.1: One-dimensional energy spectrum at $y = 0$ at streamwise locations: a) $x/\delta_1 = 200$, b) $x/\delta_1 = 225$, c) $x/\delta_1 = 250$, d) $x/\delta_1 = 325$. Dashed line indicates constant -5/3 slope.

6.1 Flow turbulence and self-similarity

In this section, the quality of generated turbulence in DNS is analyzed using the one-dimensional energy spectrum [64]:

$$E_{xx}(\omega) = \frac{1}{\pi}\int_{-\infty}^{\infty} e^{-i\omega\tau} R_x x(\tau) d\tau = \frac{1}{\pi}\int_{-\infty}^{\infty} e^{-i\omega\tau}\langle u(t)u(t+\tau)\rangle d\tau, \tag{6.2}$$

computed at $y = 0$ at selected locations in the streamwise direction. The simulated flow self-similarity is addressed as well.

The one-dimensional energy spectrum is shown in Figure 6.1. The constant slope of -5/3 (dashed line) corresponding to the spectrum inertial range is observed between $x/\delta_1 \approx 200 - 225$, meaning the flow is fully turbulent downstream of this location. Figure 6.1d shows that turbulence is maintained further downstream, close to the domain outlet.

The flow is also examined for self-similarity. In the experiments [10], the mixing layer self-similarity was reported around $L_x = 312.5\delta_1$. One of the mixing layer self-similarity conditions is the linear growth of its thickness. This is observed in the simulation at approximately $x/\delta_1 = 180$ as shown in Figure 6.2, where the dashed lines correspond to the constant slopes $\partial\delta_{ML}/\partial x = 0.0262$ and $\partial\theta/\partial x = 0.0103$. The slopes were calculated using a least-squares line fitting procedure with thickness values at $x/\delta_1 > 180$, which yields a goodness-of-fit measure of $R^2 = 0.998$ for both the mixing layer and momentum thicknesses, where R^2 is the coefficient of determination

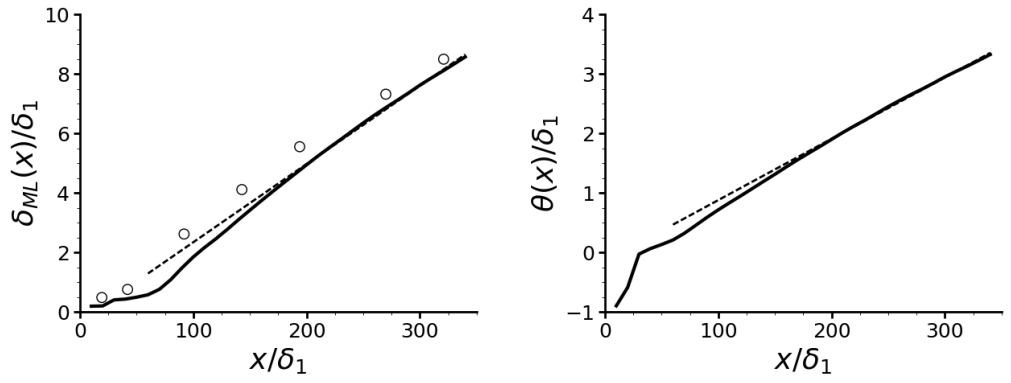

(a) **(b)**

Figure 6.2: The mixing layer growth characterized by a) mixing layer thickness, b) momentum thickness. Notations: lines DNS data (Case IV), circles experiment [10]. Line styles: solid - DNS data, dashed - constant slope line.

from the linear fit. Reported growth rate in [10] is $\partial\delta_{ML}/\partial x = 0.023$, which is about 10% lower than result from numerical simulations. These results are consistent with experimental observations [10], where untripped inflow conditions produced higher growth rate than tripped conditions, suggesting that perturbing the flow results in lower growth rate. When comparing numerical inflow conditions against wind tunnel conditions (see Section 5.1), it is clear that experimental boundary layers are more perturbed than numerical ones, which may explain why the simulated mixing layer has a slightly higher growth rate than the experimental one. It should be mentioned that there are uncertainties associated to the computation of δ_{ML} and $\partial\delta_{ML}/\partial x$ in both experimental and numerical results, and it is possible that the difference in growth rate between wind-tunnel and simulation results may be due to these uncertainties.

Another indication of self-similarity is turbulence statistics becoming independent of the streamwise location when normalized with respect to the mixing layer thickness and the velocity difference, ΔU. For the integral of the turbulent kinetic energy across the mixing layer, $K = 0.5(K_x + K_y + K_Z)$, this requirement is equivalent to the linear growth of K with the distance downstream the splitter plate [4]. Figure 6.3

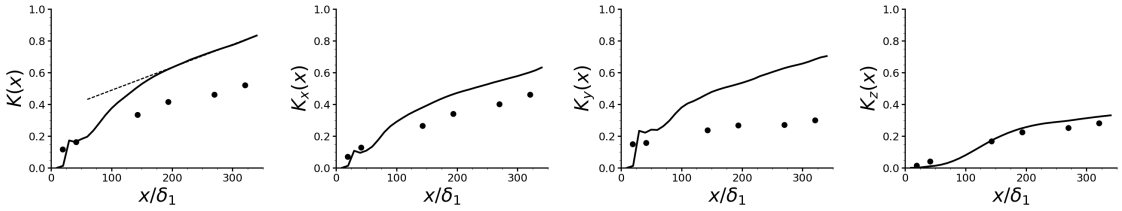

Figure 6.3: Streamwise evolution of the turbulent kinetic energy and the normal Reynolds stresses integrated across the mixing layer. Notations are the same as in Figure 6.2.

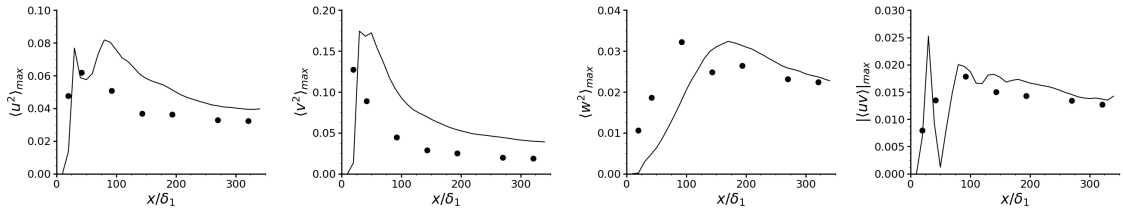

Figure 6.4: Streamwise evolution of peak values of Reynolds stresses. Notations: solid line – DNS (Case IV), circles – experiment [10].

demonstrates that this is indeed the case at $x/\delta_1 > 180$, similar to what is observed in Figure 6.2 for the mixing layer thickness, with growth rate $\partial K/\partial x = 0.0014$ given by the slope of the straight dashed line, with $R^2 = 0.997$.

Peak values of Reynolds stresses in Figure 6.4 become almost constant towards the domain outlet, achieving similar rate of decay as experimental data around $x/\delta_1 = 270$. Profiles of the Reynolds stresses $\langle u^2 \rangle$ and $\langle uv \rangle$ are well converged in the considered range between $x = 300\delta_1$ and $320\delta_1$ (Figure 6.5). The $\langle v^2 \rangle$- and $\langle w^2 \rangle$ profiles overlap with some variability at $x = 300\delta_1$ and $310\delta_1$, but peak values change by less than 3.5% in the considered range for both statistics. Overall, the analysis of the Reynolds stress profiles suggests that the location at $x = 300\delta_1$ is a suitable candidate for the flow self-similarity. This value is in a close agreement with the experimental observations ($x = 312.5\delta_1$).

A more rigorous criterion for self-similarity based on the total dissipation of the turbulent kinetic energy,

$$\mathcal{E} = \int_{-L_y/2}^{L_y/2} \varepsilon dy = \int_{-L_y/2}^{L_y/2} \left\langle \frac{\partial u_i}{\partial x_k} \frac{\partial u_i}{\partial x_k} \right\rangle dy, \tag{6.3}$$

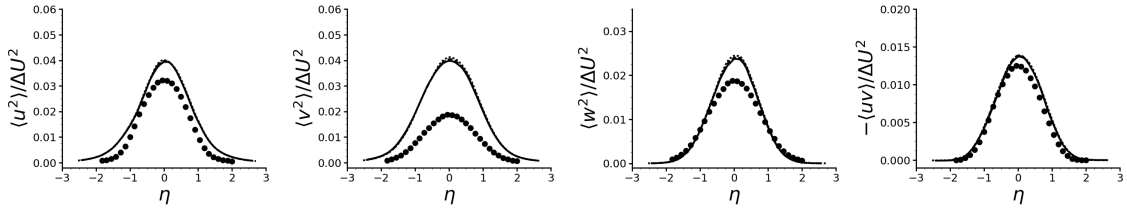

Figure 6.5: Reynolds stress profiles in the self-similar region. Notations: lines – DNS (Case IV), circles – experiment [10]. Line styles: dotted – $x/\delta_1 = 300$**, dashed** – $x/\delta_1 = 310$**, solid** – $x/\delta_1 = 320$**.**

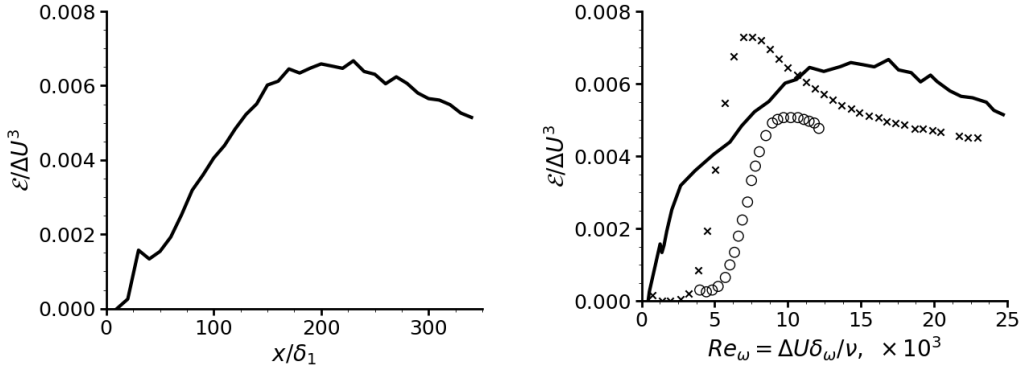

Figure 6.6: Evolution of the turbulent kinetic energy dissipation rate integrated across the mixing layer a) in the streamwise direction, b) as a function of the local Reynolds number. Notations: solid lines - current DNS data, $\times$ **– DNS data from [4],** $\circ$ **- DNS data from [68].**

was proposed in [68, 18] and requires $\mathcal{E}$ to be constant in a self-similar mixing layer. In the current simulation, $\mathcal{E}$ initially grows rapidly peaking at $x/\delta_1 \approx 180$ and reducing slowly towards the domain exit (Figure 6.6a). This location is in agreement with the beginning of the constant slope for the mixing layer thickness and the integrated turbulent kinetic energy shown in Figures 6.2 and 6.3, respectively.

In Figure 6.6b, results of the current simulation are compared against data for spatially- and temporally-developing turbulent mixing layers obtained in other DNS [4, 68]. In the figure, the normalized $\mathcal{E}$ is plotted as a function of the Reynolds number based on the vorticity thickness, $\delta_\omega = \Delta U / \left(\partial U/\partial y\right)_{max}$. The total dissipation rate behaves similarly in the three simulations, slowly converging towards

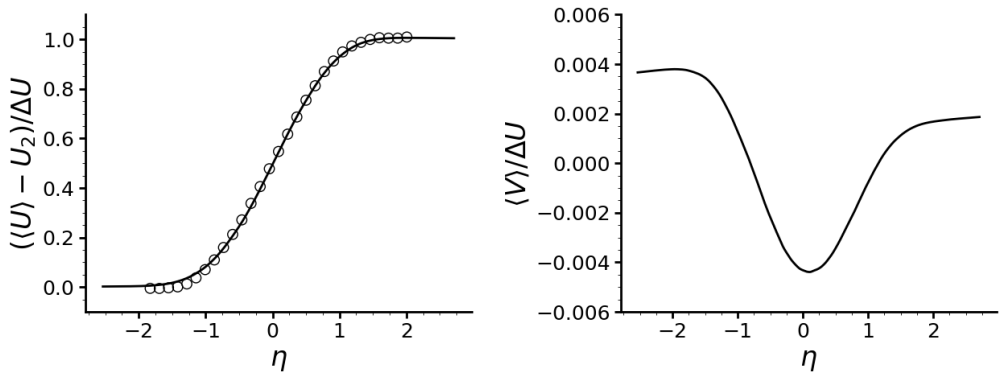

(a) **(b)**

Figure 6.7: Profiles of planar mean velocity component at $x = 300\delta_1$. a) normalized $\langle U\rangle$, b) normalized $\langle V\rangle$. Notations: solid lines - current DNS data, $\circ$ - experiment at $x = 324\delta_1$ [10].

values of $\mathcal{E} \sim 0.0045 - 0.005$. Close values of this parameter obtained in three DNS are remarkable given the simulations differences. Notice that none of the simulations achieved constant asymptotic value of $\mathcal{E}$, even though asymptotic turbulence statistics were reported in [4] and [68] as in the current study. This suggests that turbulence statistics (mean velocity and Reynolds stresses) can have an asymptotic behavior, before $\mathcal{E}$ becomes constant. The mixing layer self-similarity may also be a local phenomenon, not sustainable on a long distance.

6.2 Mean velocity and velocity moments

In this section, self-similar profiles taken at $x = 300\delta_1$ of mean velocity components and velocity moments up to fifth order are presented. Only statistics relevant to a planar flow are presented. Higher-order moments have the form $\langle u^n v^m w^k\rangle$, where $n+m+k = 2, 3, 4, 5$ for second-, third-, fourth- and fifth-order moments, respectively. Only moments with $k = 0, 2$ are considered for planar flows. While moments with $k = 4$ may be non-zero, e.g. $\langle w^4\rangle$, these are not used in the closure of RANS equations representing planar flows, and thus are not presented in this chapter.

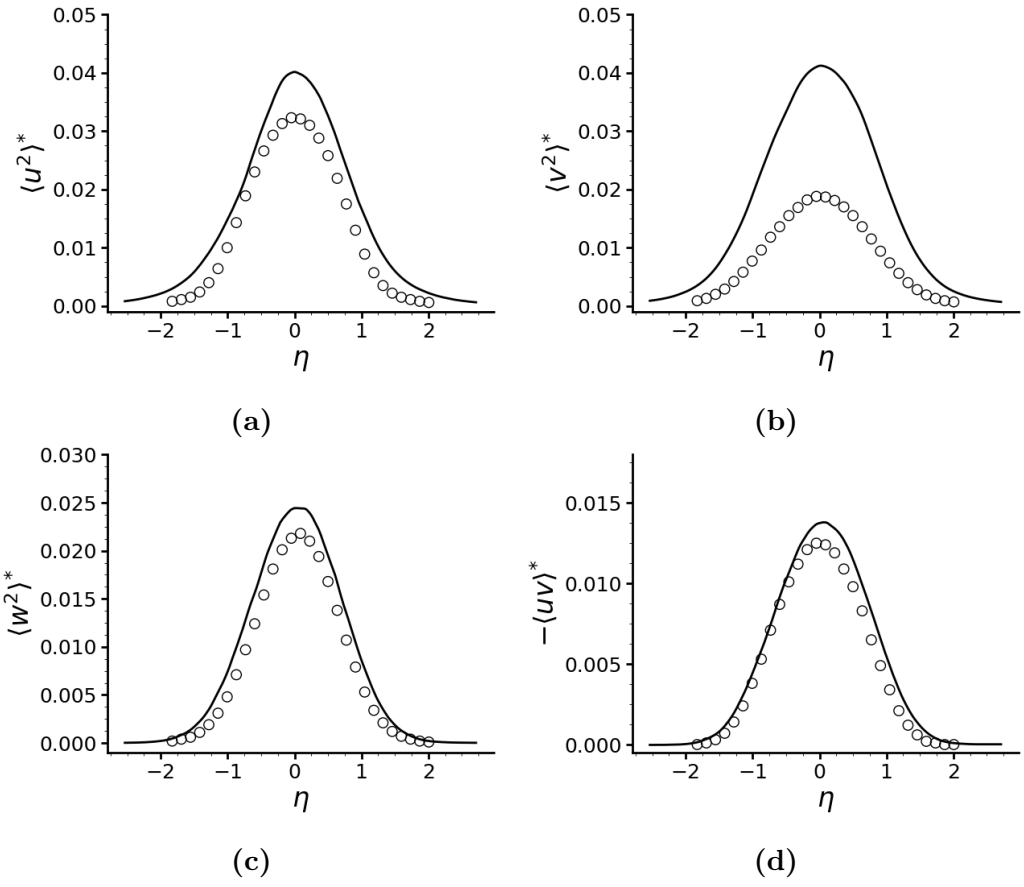

Figure 6.8: Reynolds stress profiles at $x = 300\delta_1$. a) $\langle u^2\rangle^*$, b) $\langle v^2\rangle^*$, c) $\langle w^2\rangle^*$, d) $\langle uv\rangle^*$. Notations: solid lines - current DNS data, $\circ$ - experiment at $x = 324\delta_1$ [10].

Streamwise mean velocity in Figure 6.7a shows the typical shear layer profile, which is in good agreement with experimental data. Transverse mean velocity (Figure 6.7b) is negative towards the flow centerline ($-1 < \eta < 1$), which indicates that the shear layer moves towards the slow-speed stream ($y < 0$) as it convects downstream, which is a well documented behavior of spatially developing mixing layers [42, 16, 25]. To the best of the author's knowledge, there is no experimental or numerical data available for $\langle V\rangle$ that could be compared directly with current results: publications either completely omit this statistic [17, 81, 9, 4, 80, 68, 73] or used flow conditions which significantly differ from those used in this study [42, 16, 23].

Profiles of velocity moments are shown in Figures 6.8-6.11. In the figures, $\langle ...\rangle^*$ indicates that kth-orders statistics have been normalized by dividing by $(\Delta U)^k$.

Numerical results for Reynolds stresses are higher than wind-tunnel values Figure 6.8, specially for $\langle v^2 \rangle$. Considering the analysis in Chapter 5, differences in inflow conditions (laminar boundary layers in simulation vs. "nominally laminar" boundary layers in the experiment) cause turbulence statistics to differ. Restrictions in the computational domain size, particularly in the transverse dimension (L_y), may also promote higher peak values for Reynolds stresses, as evidenced by the behavior of Case II in Section 5.4.

Figure 6.9 shows profiles of third-order moments that are anti-symmetric with respect to the flow centerline ($\eta = 0$). Experimental data is only available for moment $\langle uv^2 \rangle$ (Figure 6.9a), which seems to match numerical results. Higher-order moments are shown in Figures 6.10 and 6.11. These statistics may be used for validation of Gram-Charlier series expansion. As an example, the Gram-Charlier approximations of $\langle u^5 \rangle$ and $\langle v^5 \rangle$ are compared against computed statistics in Figure 6.12. The figure shows the potential of fifth-order moments to be modeled by Gram-Charlier series expansion and that statistics presented in this work can be used for validation of Gram-Charlier approximation in free-shear flows.

6.3 Reynolds stress transport budgets

Budget terms from transport equations of Reynolds stresses, computed using equations in Appendix B, are shown in this section.

Convection, production, turbulent diffusion and velocity/pressure-gradient terms normalized by $\delta_{ML}/\Delta U^3$ are shown in Figure 6.13. Molecular diffusion and viscous dissipation terms are shown in Figure 6.14.

Dissipation terms show spikes at the location elemental interfaces. These appear when gradients are calculated from velocity field, since continuity is not enforced across element boundaries on derivatives of velocity (the solution is C^0 continuous on the domain). According to [69], the spikes are indicative of under-resolved flow and

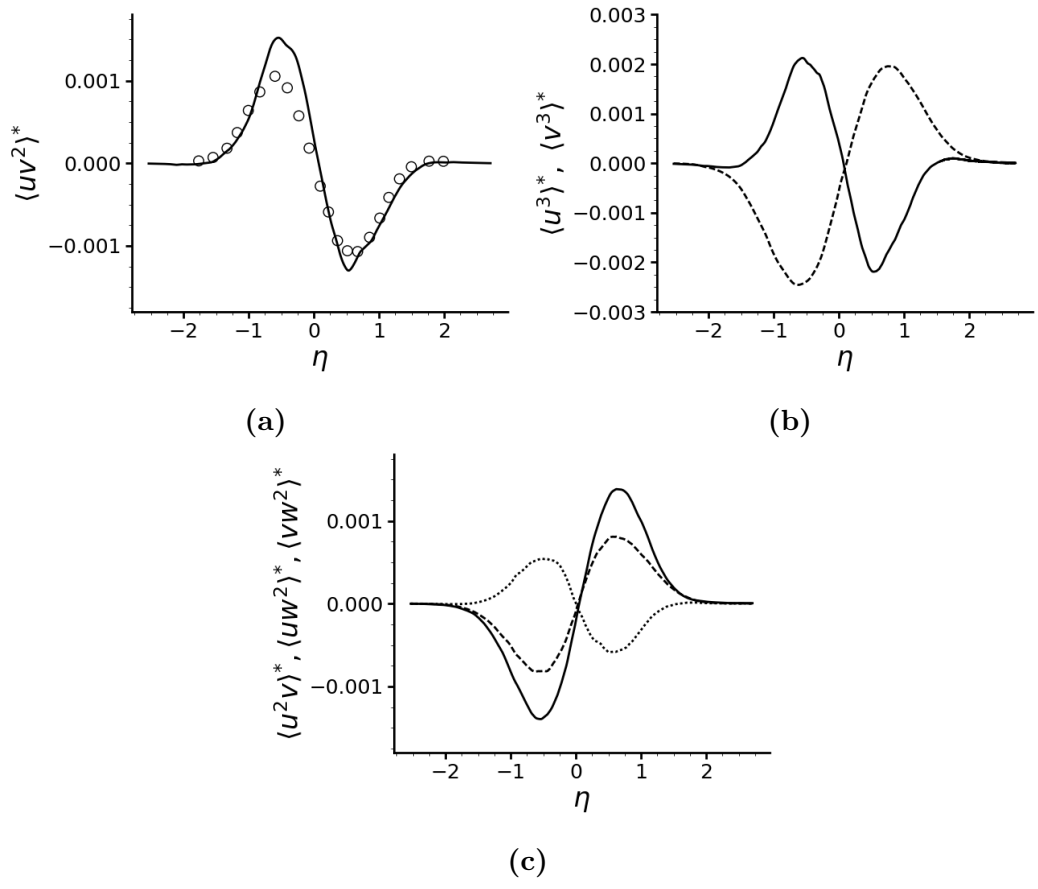

Figure 6.9: Profiles of third-order moments at $x = 300\delta_1$. a) $\langle uv^2\rangle^*$; b) solid line – $\langle u^3\rangle^*$, dashed line – $\langle v^3\rangle^*$; c) solid line – $\langle u^2v\rangle^*$, dashed line – $\langle vw^2\rangle^*$, dotted line – $\langle uw^2\rangle^*$. Notations: lines - current DNS data, ∘ - experiment [10].

should vanish by solving the flow with spectral elements of higher polynomial order. However, tests conducted for the mixing layer flow using polynomials of order $N = 13$ (compared to $N = 11$ used to produce results presented in this chapter) did not show diminished spikes in viscous dissipation terms. Results suggest that the spikes are an inherent problem of the spectral-element method, and the reason for such spikes is yet to be identified. Molecular diffusion terms also present spikes related with spatial derivatives at elemental interfaces, but these are of smaller magnitude than in viscous dissipation term. Different approaches were used to try to mitigate the effect of such spikes, but attempts were unfruitful.

The plots presented in this section imply that while spatial resolution satisfying

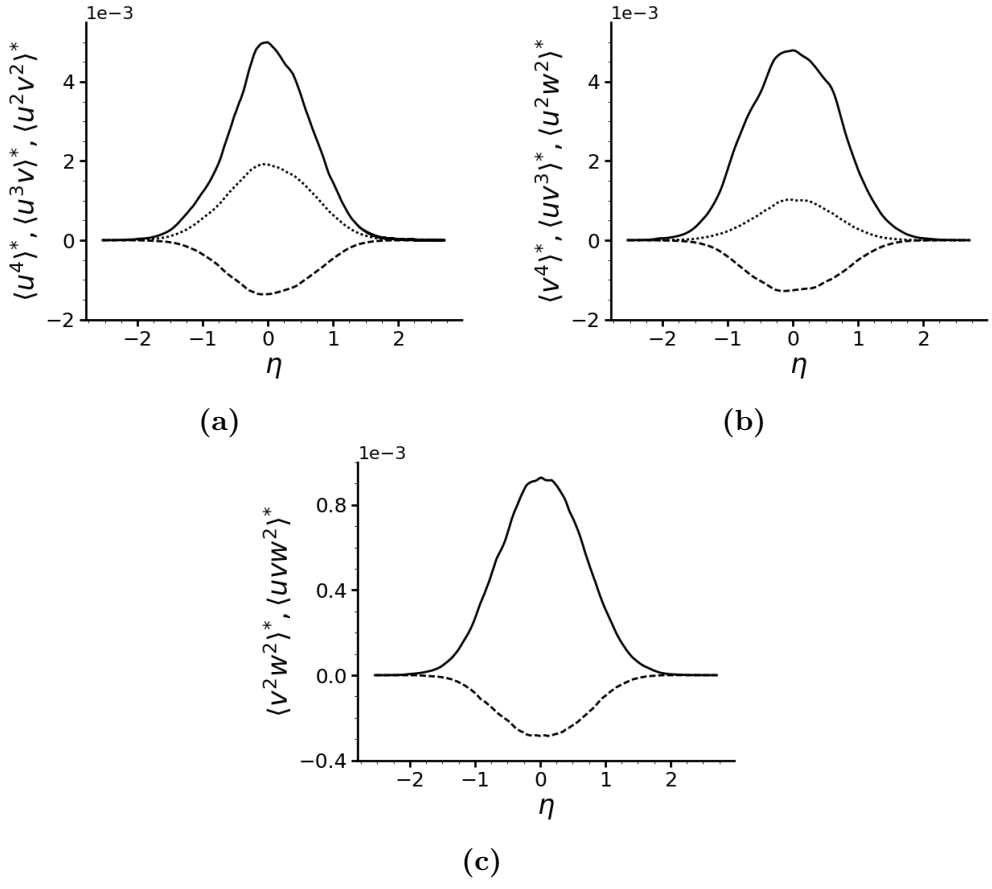

Figure 6.10: Profiles of fourth-order moments at $x = 300\delta_1$. a) solid line – $\langle u^4\rangle^*$, dashed line – $\langle u^3v\rangle^*$, dotted line – $\langle u^2v^2\rangle^*$; b) solid line – $\langle v^4\rangle^*$, dashed line – $\langle uv^3\rangle^*$, dotted line – $\langle u^2w^2\rangle^*$; c) solid line – $\langle v^2w^2\rangle^*$, dashed line – $\langle uvw^2\rangle^*$.

the criterion $(\delta x \cdot \delta y \cdot \delta z)^{1/3} < 4.9\eta_K$, proposed in Section 4.4 based on discussion in [61, 78], may be sufficient for resolution of velocity field and computation of velocity moments, it may be insufficient for computation of budget terms, specially viscous dissipation. Increasing statistical sampling by increasing simulation time did not improve current statistics for budgets. Improvement of the quality of statistics for computation of budget terms will remain a subject for future research.

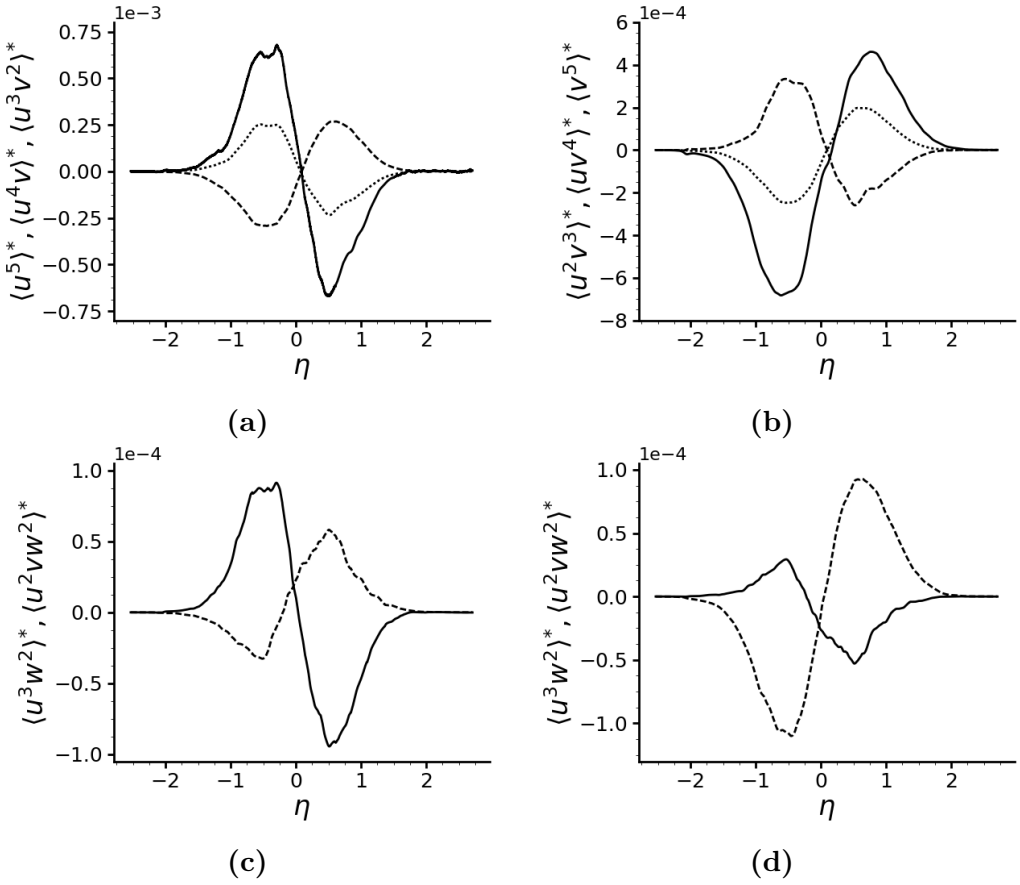

Figure 6.11: Profiles of fifth-order moments at $x = 300\delta_1$. a) Solid line – $\langle u^5\rangle^*$, dashed line – $\langle u^4v\rangle^*$, dotted line – $\langle u^3v^2\rangle^*$; b) solid line – $\langle v^5\rangle^*$, dashed line – $\langle uv^4\rangle^*$, dotted line – $\langle u^2v^3\rangle^*$; c) solid line – $\langle u^3w^2\rangle^*$, dashed line – $\langle u^2vw^2\rangle^*$; d) solid line – $\langle uv^2w^2\rangle^*$, dashed line – $\langle v^3w^2\rangle^*$.

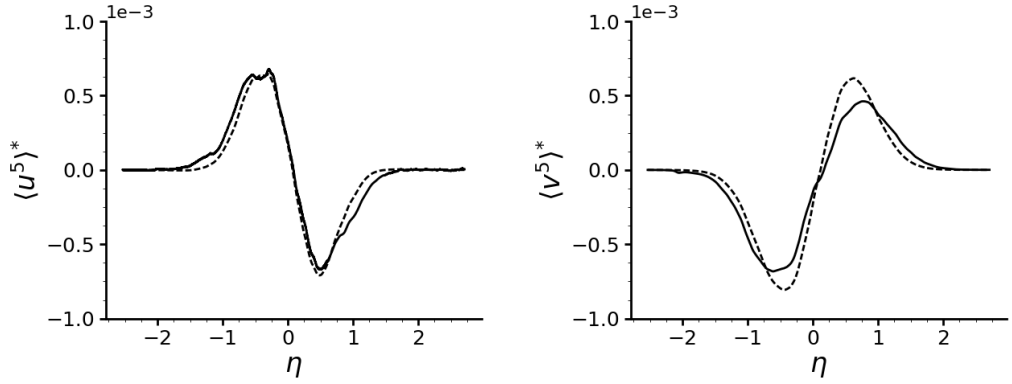

(a) **(b)**

Figure 6.12: Profiles of fifth moments and truncated Gram-Charlier series expansion computed at $x = 300\delta_1$. a) $\langle u^5 \rangle^*$; b) $\langle v^5 \rangle^*$. Notations: solid line - computed moments, dashed line - truncated Gram-Charlier series expansion.

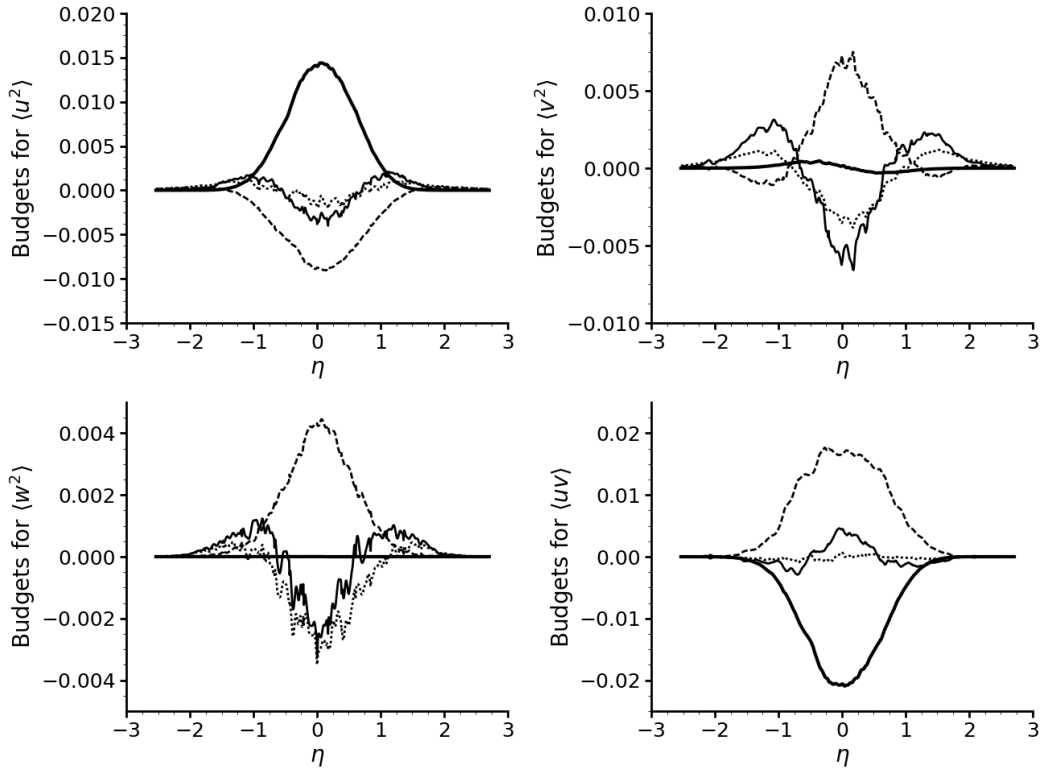

Figure 6.13: Normalized budget terms from transport equations of Reynolds stresses. Notation: thick solid line – production, thin solid line – turbulent diffusion, dotted line – convection, dashed line – velocity/pressure-gradient.

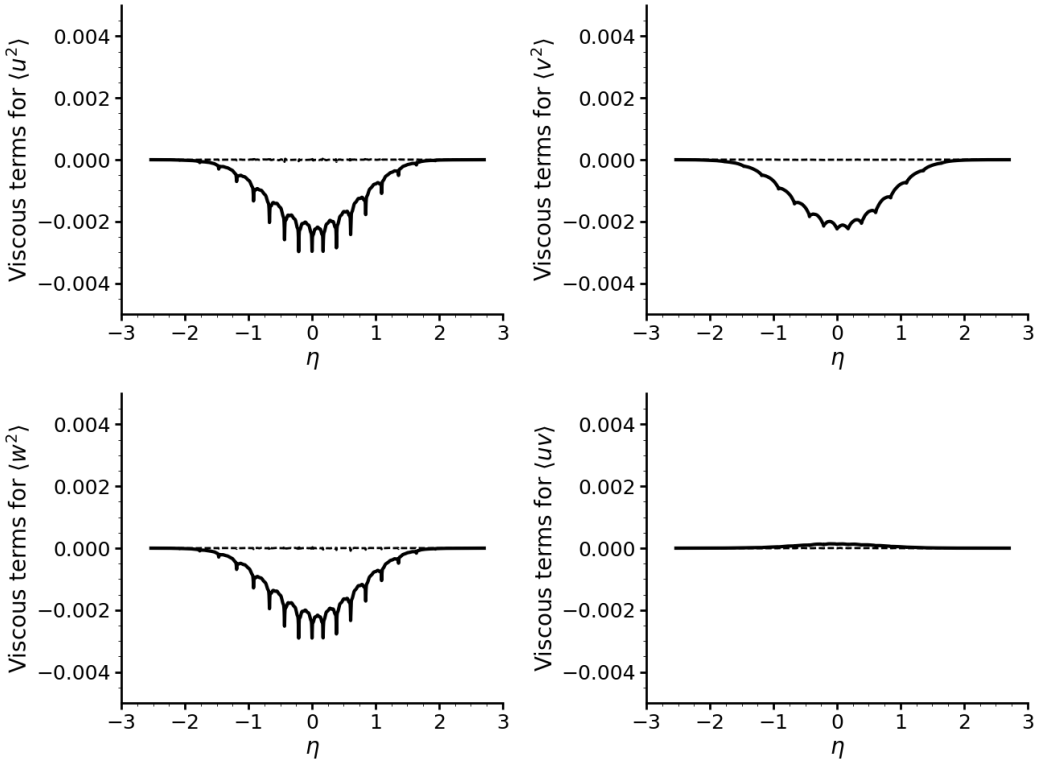

Figure 6.14: Normalized molecular diffusion and viscous dissipation terms from transport equations of Reynolds stresses. Notation: solid line – dissipation, dashed line – molecular diffusion.

Chapter 7

Conclusions

We present results of DNS of a planar spatially-developing incompressible turbulent mixing layer between two co-flowing laminar boundary layers. The purpose of the study was to generate a more complete data set of statistical parameters characterizing the flow to facilitate better understanding of the flow physics, which has been achieved by generating statistics for velocity moments up to fifth order. In addition, better understanding of the effects of simulation parameters on numerical results was achieved by conducting a sensitivity analysis of the simulation results to variations in dimensions of the computational domain with the focus on determining the domain dimensions sufficient for the mixing layer to achieve its self-similar state at an acceptable simulation cost.

Seven computational domains of similar geometry, but different dimensions were considered. Two structured grids were generated. Both grids comply with the state-of-the-art requirements for a DNS grid, but one of the grids has finer resolution in the splitter plate wake area. With respect to the domain transverse dimension, the current simulations demonstrated that the criterion for this dimension: $6.96 < L_y/\delta_{\omega,max} < 8.3$, used in the previous studies [4, 80] does not guarantee independence of all considered statistics from this simulation parameter. A new condition: $L_y/\left(\delta_{ML}\right)_{max} \geq 17.5$, is proposed to ensure the results independence from

this parameter. The insufficient domain dimension in the transverse direction leads to increase in the maximum values of the Reynolds stress profiles, particularly those including velocity fluctuations in the plane normal to the transverse direction. As a result, one can expect the turbulence level to be increased when comparing with the solution independent from this domain dimension.

The study confirmed the criterion $A = L_z/\theta_{max} > 10$ proposed in [48] to eliminate effects of the domain spanwise dimension on the simulation results. With this condition being satisfied, the maximum value of the Reynolds stress $\langle w^2 \rangle$ was found to be sensitive to variation in L_z close to the domain exit. Minor changes in the maximum value of the Reynolds stress $\langle uv \rangle$ were also observed in the vicinity of the splitter plate. Other statistics were not affected. The observed effects appear to be unrelated to the splitter plate thickness.

Variation in the domain streamwise dimension has the strongest effect on all considered statistics and everywhere in the flow. In particular, increasing the domain size in this direction delayed the flow mixing and its transition to turbulence. The level of turbulent kinetic energy was overall higher in simulations with the shorter domain, but near the shorter domain exit, the turbulent kinetic energy in streamwise and transverse directions was found to be suppressed below that level in the longer domain. Possible causes can be multiple including numerical, such as boundary conditions, for example. However, experiments also discovered that the streamwise dimension of the test section influences the measurements. If the effect is physical, then, the solution independent of this simulation parameter may not exist.

The grid effects were also found to be strong. The turbulent mixing layer growth, evolution of the normal Reynolds stresses integrated across the mixing layer (except for K_y), the Reynolds stresses in the vicinity of the splitter plate and $\langle w^2 \rangle$ everywhere in the domain were the statistics most influenced by changes in the grid. In particular, the impact of the grid stretching on the simulation results requires further examination. Similar to the domain streamwise dimension effects, it is questionable whether the grid-independent statistics can be generated from DNS in complex flow

geometries. Some effects of the simulation initial conditions were observed on all Reynolds stresses in the splitter plate vicinity. The Reynolds stress $\langle u^2 \rangle$ was influenced everywhere in the flow.

Time step size had to be considered as another factor influencing numerical solution. While decreasing time step size produced a slight increase in turbulent kinetic energy, particularly in integral quantities K_y and K_z, a larger time step size produced results in closer agreement with experimental data. This numerical parameter has the potential to dampen or trigger instabilities in the flow which affect turbulence statistics, and therefore, should be chosen so that the simulated flow appropriately represents the physical flow.

Inflow boundary layer parameters at the trailing edge of the splitter plate mostly affected the mixing layer growth rate and turbulence statistics close to the trailing edge, having less of an effect on turbulence statistics downstream.

The study also confirmed the conclusion from previous studies [39, 40, 14] about the importance of incorporating the finite splitter plate thickness into computations for matching the mixing layer growth observed in experiments. The mixing layer thickness growth and the integral values of turbulent kinetic energy across the mixing layer obtained using a thick plate are in close agreement with the experimental data without any artificial velocity perturbations being seeded into the flow to facilitate turbulence. That is not the case when using an infinitely thin plate. Dynamics of the Reynolds stresses along the flow streamwise direction is also better reproduced with a thick plate than with a thin plate.

The study determined dimensions of the computational domain suitable for the mixing layer to reach self-similarity. This domain was used for collecting self-similar high-order statistics and budget terms from Reynolds stress transport equations. Such statistics were not previously available for a spatially developing mixing layer in self-similar regime in published literature. Examples of fifth-order moments computed using Gram-Charlier series expansion show the usefulness of current statistics for the validation of this approximation. Profiles of budget terms, particularly vis-

cous dissipation, showed undesired features which may be related to poor spatial resolution. However, such features may also be associated with inherent problems in the spectral-element method for computing such terms, since velocity gradients are not continuous across the computational domain. More strict spatial resolution may be required in future studies using spectral-element method to compute reliable budget terms.

References

[1] AGARD. A selection of test cases for the validation of large-eddy simulations of turbulent flows. *AGARD Advisory Report 345* (1998).

[2] Ahmed, S. F., Ledezma, I., and Mastorakos, E. Spark ignition in a turbulent shearless fuel-air mixing layer: Average flame growth rates. *47th AIAA Aerospace Sciences Meeting including the New Horizons Forum and Aerospace Exposition*, January (2009), 1–12.

[3] Argonne National Laboratory, Illinois. Nek5000: a fast and scalable high-order solver for computational fluid dynamics. https://nek5000.mcs.anl.gov.

[4] Attili, A., and Bisetti, F. Statistics and scaling of turbulence in a spatially developing mixing layer at $Re_\lambda = 250$. *Physics of Fluids 24*, 3 (2012), 035109.

[5] Attili, A., and Bisetti, F. Fluctuations of a passive scalar in a turbulent mixing layer. *Physical Review E 033013*, July (2013), 0526.

[6] Attili, A., Cristancho, J. C., and Bisetti, F. Statistics of the turbulent/non-turbulent interface in a spatially developing mixing layer. *Journal of Turbulence 15*, October (2014), 555–568.

[7] Balaras, E., Piomelli, U., and Wallace, J. M. Self-similar states in turbulent mixing layers. *Journal of Fluid Mechanics 446* (2001), 1–24.

[8] Bastankhah, M., and Porté-Agel, F. A new analytical model for wind-turbine wakes. *Renewable Energy 70* (2014), 116–123.

[9] Bell, J. H., and Mehta, R. D. Design and calibration of the mixing layer and wind tunnel. Tech. Rep. JIAA-TR-89, 1989.

[10] Bell, J. H., and Mehta, R. D. Development of a two-stream mixing layer from tripped and untripped boundary layers. *AIAA Journal 28*, 12 (1990), 2034–2042.

[11] Bernal, L. P., Breidenthal, R. E., Brown, G. L., Konrad, J. H., and Roshko, A. On the development of three dimensional small scales in turbulent mixing layers. In *2nd Symposium on Turbulent Shear Flows* (1979), pp. 8.1–8.6.

[12] Bernal, L. P., and Roshko, A. Streamwise vortex structure in plane mixing layers. *Journal of Fluid Mechanics 170* (1986), 499–525.

[13] Biancofiore, L. Crossover between two- and three-dimensional turbulence in spatial mixing layers. *Journal of Fluid Mechanics 745* (2014), 164–179.

[14] Braud, C., Heitz, D., Arroyo, G., Perret, L., Delville, J., and Bonnet, J. P. Low-dimensional analysis, using POD, for two mixing layer-wake interactions. *International Journal of Heat and Fluid Flow 25*, 3 (2004), 351–363.

[15] Breidenthal, R. Structure in turbulent mixing layers and wakes using a chemical reaction. *Journal of Fluid Mechanics 109*, 6 (1981), 1–24.

[16] Browand, F., and Latigo, B. Growth of the two dimensional mixing layer from a turbulent and nonturbulent boundary layer. *Physics of Fluids (1958-1988) 22*, 6 (1979), 1011.

[17] Brown, G. L., and Roshko, A. On density effects and large structure in turbulent mixing layers. *J . Fluid Meeh 64*, 4 (1974), 775–816.

[18] Clark, T. T., and Zhou, Y. Self-similarity of two flows induced by instabilities. *Physical Review E - Statistical Physics, Plasmas, Fluids, and Related Interdisciplinary Topics 68*, 6 (2003), 1–16.

[19] Comte, P., Lesieur, M., and Lamballais, E. Large- and small-scale stirring of vorticity and a passive scalar in a 3-D temporal mixing layer. *Physics of Fluids A: Fluid Dynamics 4*, 12 (1992), 2761.

[20] Currie, I. *Fundamental Mechanics of Fluids, Fourth Edition*. Civil and mechanical engineering. Taylor & Francis, 2012.

[21] De Feriet, J. K. The gram-charlier approximation of the normal law and the statistical description of homogeneous turbulent flow near statistical equilibrium. Tech. Rep. 2013, David Taylor Model Basin, Applied Mathematics Lab, 1966.

[22] Delville, J., Bellin, S., Garem, J. H., and Bonnet, J. P. Analysis of structures in a turbulent, plane mixing layer by use of a pseudo flow visualization method based on hot-wire anemometry. In *Advances in turbulence 2: proceedings from the Second European Turbulence Conference* (Berlin, 1989), pp. 251–256.

[23] Delville, J., Ukeiley, L., Cordier, L., Bonnet, J. P., and Glauser, M. Examination of large-scale structures in a turbulent plane mixing layer. Part 1. Proper orthogonal decomposition. *Journal of Fluid Mechanics 391* (1999), 91–122.

[24] Deville, M. O., Fischer, P. F., and Mund, E. H. *High-Order Methods for Incompressible Fluid Flow*. Cambridge Monographs on Applied and Computational Mathematics. Cambridge University Press, 2002.

[25] Dimotakis, P. E. Two-dimensional shear layer entrainment. *AIAA 24*, 11 (1986), 1791–1796.

[26] Dimotakis, P. E. Turbulent free shear layer mixing and combustion. *Progress in Astronautics and Aeronautics 137* (1991), 265–340.

[27] Dimotakis, P. E. The mixing transition in turbulent flows. *Journal of Fluid Mechanics 409*, 4 (2000), 69–98.

[28] Dimotakis, P. E., and Brown, G. L. The mixing layer at high Reynolds number: large-structure dynamics and entrainment. *Journal of Fluid Mechanics 78*, 03 (1976), 535.

[29] Dziomba, B., and Fiedler, H. E. Effect of initial conditions on two-dimensional free shear layers. *Journal of Fluid Mechanics 152* (1985), 419442.

[30] Galperin, B., and Orszag, S. *Large Eddy Simulation of Complex Engineering and Geophysical Flows*. Cambridge University Press, 1993.

[31] Hanjali, K., and Launder, B. *Modelling Turbulence in Engineering and the Environment: Second-Moment Routes to Closure*. Cambridge University Press, 2011.

[32] Ho, C., and Huerre, P. Perturbed free shear layers. *Annual Review Fluid Mechanics 16* (1984), 365–422.

[33] Huang, L.-S., and Ho, C.-M. Small scale transition in a plane mixing layer. *J. Fluid Mech. 210* (1990), 475–500.

[34] Jeong, J., and Hussain, F. On the identification of a vortex. *Journal of Fluid Mechanics 285*, February 1995 (1995), 69–94.

[35] Jeyapaul, E., Coleman, G. N., and Rumsey, C. L. Assessment of Higher-order RANS Closures in a Decelerated Planar Wall-bounded Turbulent Flow. *44th AIAA Fluid Dynamics Conference, AIAA AVIATION Forum*, AIAA 2014-2088 (2014), 1–27.

[36] Jimenez, J., Martinez-Val, R., and Rebollo, M. On the Origin and Evolution of Three Dimensional Effects in the Mixing Layer. Tech. rep., 1979.

[37] Konrad, J. H. *An Experimental Investigation of Mixing in Two-Dimensional Turbulent Shear Flows with Applications to Diffusion-Limited Chemical Reactions*. Dissertation (Ph.D.), California Institute of Technology, 1977.

[38] Koochesfahani, M. M., and Dimotakis, P. E. Mixing and chemical reactions in a turbulent liquid mixing layer. *Journal of Fluid Mechanics 170* (1986), 83–112.

[39] Laizet, S., and Lamballais, E. Direct numerical simulation of a spatially evolving flow from an asymmetric wake to a mixing layer. *Direct and Large-Eddy Simulation VI 10* (2006), 467–474.

[40] Laizet, S., Lardeau, S., and Lamballais, E. Direct numerical simulation of a mixing layer downstream a thick splitter plate. *Physics of Fluids* (2010).

[41] LeBoeuf, R. L., and Mehta, R. D. Streamwise vortex meander in a plane mixing layer. *Physics of Fluids A: Fluid Dynamics 5*, 8 (1993), 1983.

[42] Liepmann, H. W., and Laufer, J. Investigations of free turbulent mixing. Tech. Rep. 1257, NACA, 1947.

[43] Lilly, K. The representation of small-scale turbulence in numerical simulation experiments.

[44] Liu, Y., Sun, X., Sethi, V., Nalianda, D., Li, Y. G., and Wang, L. Review of modern low emissions combustion technologies for aero gas turbine engines. *Progress in Aerospace Sciences 94*, September (2017), 12–45.

[45] Maday, Y., Patera, A. T., and Rønquist, E. M. An operator-integration-factor splitting method for time-dependent problems: Application to incompressible fluid flow. *Journal of Scientific Computing 5*, 4 (Dec 1990), 263–292.

[46] Maly, R. State of the art and future needs in s.i. engine combustion.

[47] Mansour, N., Ferziger, J., and Reynolds, W. *Large-eddy Simulation of a Turbulent Mixing Layer*. Technical report (Stanford University. Thermosciences Division). Department of Mechanical Engineering, Stanford University., 1978.

[48] McMullan, W. Spanwise domain effects on the evolution of the plane turbulent mixing layer. *International Journal of Computational Fluid Dynamics 29*, 6-8 (2015), 333–345.

[49] McMullan, W. a., Gao, S., and Coats, C. M. The effect of inflow conditions on the transition to turbulence in large eddy simulations of spatially developing mixing layers. *International Journal of Heat and Fluid Flow 30*, 6 (2009), 1054–1066.

[50] McMullan, W. A., and Garrett, S. J. Initial condition effects on large scale structure in numerical simulations of plane mixing layers. *Physics of Fluids 28*, 1 (2016), 015111.

[51] Mehta, R. Effect of velocity ratio on plane mixing layer development: Influence of the splitter plate wake. *Experiments in Fluids 204* (1991), 194–204.

[52] Mehta, R. D., and Westphal, R. V. Near-field turbulence properties of single- and two-stream plane mixing layers. *Experiments in Fluids 4*, 5 (1986), 257–266.

[53] Michalke, A. On the inviscid instability of the hyperbolictangent velocity profile. *Journal of Fluid Mechanics 19*, 4 (1964), 543556.

[54] Miksad, R. W. Experiments on the nonlinear stages of free-shear-layer transition. *Journal of Fluid Mechanics 56*, 4 (1972), 695719.

[55] Moin, P., and Mahesh, K. DIRECT NUMERICAL SIMULATION: A Tool in Turbulence Research. *Annual Review of Fluid Mechanics 30* (1998), 539–578.

[56] Monkewitz, P. A., and Huerre, P. Influence of the velocity ratio on the spatial instability of mixing layers. *The Physics of Fluids 25*, 7 (1982), 1137–1143.

[57] Moser, R. D., and Rogers, M. M. The three-dimensional evolution of a plane mixing layer: pairing and transition to turbulence. *Journal of Fluid Mechanics 247* (1993), 275320.

[58] Narayanan, S., and Hussain, F. Measurements of spatiotemporal dynamics in a forced plane mixing layer. *Journal of Fluid Mechanics 320* (1996), 71115.

[59] NASA Advanced Supercomputing Division. Pleiades Supercomputer. https://www.nas.nasa.gov/hecc/resources/pleiades.html. Accessed: 2018-Mar-16.

[60] Offermans, N., Marin, O., Schanen, M., Gong, J., Fischer, P. F., Schlatter, P., Obabko, A., Peplinski, A., Hutchinson, M., and Merzari, E. On the Strong Scaling of the Spectral Element Solver Nek5000 on Petascale Systems.

[61] Ohlsson, J., Schlatter, P., Fischer, P. F., and Henningson, D. S. Direct numerical simulation of separated flow in a three-dimensional diffuser. *Journal of Fluid Mechanics 650* (2010), 307.

[62] Patel, R. P. Effects of stream turbulence on free shear flows. *Aeronautical Quarterly 29* (1978), 33–43.

[63] Patera, A. T. A spectral element method for fluid dynamics: Laminar flow in a channel expansion. *Journal of Computational Physics 54*, 3 (1984), 468–488.

[64] Pope, S. *Turbulent Flows*. Cambridge University Press, 2000.

[65] Poroseva, S. V., Kaiser, B. E., Sillero, J. A., and Murman, S. M. Validation of a closing procedure for fourth-order RANS turbulence models with DNS data in an incompressible zero-pressure-gradient turbulent boundary layer. *International Journal of Heat and Fluid Flow 56* (2015), 71–79.

[66] Prandtl, L. Ueber die ausgebildete turbulenz. *Proceedings of the 2nd International Congress for Applied Mechanics* (1926).

[67] Rogers, M. M., and Moser, R. D. The three-dimensional evolution of a plane mixing layer: the kelvinhelmholtz rollup. *Journal of Fluid Mechanics 243* (1992), 183226.

[68] Rogers, M. M., and Moser, R. D. Direct simulation of a self-similar turbulent mixing layer. *Physics of Fluids 6*, 2 (1994), 903.

[69] Scheel, J. D., Emran, M. S., and Schumacher, J. Resolving the fine-scale structure in turbulent Rayleigh-Bénard convection. *New Journal of Physics 15* (2013), 113063.

[70] Slessor, M. D., Bond, C. L., and Dimotakis, P. E. Turbulent shear-layer mixing at high Reynolds numbers: effects of inflow conditions. *Journal of Fluid Mechanics 376* (1998), 115–138.

[71] Smagorinsky, J. General circulation experiments with the primitive equations. *Monthly Weather Review 91*, 3 (1963), 99–164.

[72] Spalart, P. Direct simulation of a turbulent boundary layer up to R_θ= 1410. *Journal of Fluid Mechanics*, December (1988).

[73] Takamure, K., Ito, Y., Sakai, Y., Iwano, K., Hayase, T., Takamure, K., Ito, Y., Sakai, Y., Iwano, K., and Hayase, T. Momentum transport process in the quasi self-similar region of free shear mixing layer. *Physics of Fluids 30* (2018), 015109.

[74] Tao, T. Finite time blowup for an averaged three-dimensional navier-stokes equation. *Journal of the American Mathematical Society*, 3 (2016), 601.

[75] Tenaud, C., Pellerin, S., Dulieu, a., and Ta Phuoc, L. Large Eddy Simulations of a spatially developing incompressible 3D mixing layer using the v-ω formulation. *Computers and Fluids 34* (2005), 67–96.

[76] Tomboulides, A., Lee, J., and Orszag, S. Numerical simulation of low Mach number reactive flows. *Journal of Scientific Computing 12*, 2 (1997), 139–167.

[77] Townsend, A. *The Structure of Turbulent Shear Flow*. Cambridge Monographs on Mechanics. Cambridge University Press, 1980.

[78] Vinuesa, R., Hosseini, S. M., Hanifi, A., Henningson, D. S., and Schlatter, P. Direct numerical simulation of the flow around a wing section using high-order parallel spectral methods. No. 2B-3, pp. 1–6.

[79] Vreman, B., Guerts, B., and Kuerten, H. Large-eddy simulation of the turbulent mixing layer. *Journal of Fluid Mechanics 339* (1997), 357–390.

[80] Wang, Y., Tanahashi, M., and Miyauchi, T. Coherent fine scale eddies in turbulence transition of spatially-developing mixing layer. *International Journal of Heat and Fluid Flow 28* (2007), 1280–1290.

[81] Winant, C. D., and Browand, F. K. Vortex pairing : the mechanism of turbulent mixing-layer growth at moderate Reynolds number. *Journal of Fluid Mechanics 63* (1974), 237.

[82] Wygnanski, I., and Fiedler, H. E. The two-dimensional mixing region. *Journal of Fluid Mechanics 41* (1970), 327–361.

[83] Xiao, F., Dianat, M., and McGuirk, J. J. An les turbulent inflow generator using a recycling and rescaling method. *Flow, Turbulence and Combustion 98*, 3 (Apr 2017), 663–695.

[84] Yoder, D., DeBonis, J., and Georgiadis, N. Modeling of Turbulent Free Shear Flows. *Computers & Fluids 117* (2015), 212–232.

Appendices

Appendix A

Computation of Velocity Moments

High-order moments may be calculated from mean velocity components and raw moments using the following equations:

$$\langle u_i u_j \rangle = \langle U_i U_j \rangle - \langle U_i \rangle \langle U_j \rangle \tag{A.1}$$

$$\begin{aligned} \langle u_i u_j u_l \rangle = {} & \langle U_i U_j U_l \rangle - \langle U_i \rangle \langle U_j U_l \rangle - \langle U_j \rangle \langle U_i U_l \rangle - \langle U_l \rangle \langle U_i U_j \rangle \\ & + 2 \langle U_i \rangle \langle U_j \rangle \langle U_l \rangle, \end{aligned} \tag{A.2}$$

$$\begin{aligned} \langle u_i u_j u_l u_m \rangle = {} & \langle U_i U_j U_l U_m \rangle - \langle U_i \rangle \langle U_j U_l U_m \rangle - \langle U_j \rangle \langle U_i U_l U_m \rangle \\ & - \langle U_l \rangle \langle U_i U_j U_m \rangle - \langle U_m \rangle \langle U_i U_j U_l \rangle + \langle U_i \rangle \langle U_j \rangle \langle U_l U_m \rangle \\ & + \langle U_i \rangle \langle U_l \rangle \langle U_j U_m \rangle + \langle U_i \rangle \langle U_m \rangle \langle U_j U_l \rangle + \langle U_j \rangle \langle U_l \rangle \langle U_i U_m \rangle \\ & + \langle U_j \rangle \langle U_m \rangle \langle U_i U_l \rangle + \langle U_l \rangle \langle U_m \rangle \langle U_i U_j \rangle - 3 \langle U_i \rangle \langle U_j \rangle \langle U_l \rangle \langle U_m \rangle \end{aligned} \tag{A.3}$$

$$\begin{aligned}\langle u_i u_j u_l u_m u_n\rangle &= \langle U_i U_j U_l U_m U_n\rangle - \langle U_i\rangle\langle U_j U_l U_m U_n\rangle - \langle U_j\rangle\langle U_i U_l U_m U_n\rangle \\ &\quad - \langle U_l\rangle\langle U_i U_j U_m U_n\rangle - \langle U_m\rangle\langle U_i U_j U_l U_n\rangle - \langle U_n\rangle\langle U_i U_j U_l U_m\rangle \\ &\quad + \langle U_i\rangle\langle U_j\rangle\langle U_l U_m U_n\rangle + \langle U_i\rangle\langle U_l\rangle\langle U_j U_m U_n\rangle + \langle U_i\rangle\langle U_m\rangle\langle U_j U_l U_n\rangle \\ &\quad + \langle U_i\rangle\langle U_n\rangle\langle U_j U_l U_m\rangle + \langle U_j\rangle\langle U_l\rangle\langle U_i U_m U_n\rangle + \langle U_j\rangle\langle U_m\rangle\langle U_i U_l U_n\rangle \\ &\quad + \langle U_j\rangle\langle U_n\rangle\langle U_i U_l U_m\rangle + \langle U_l\rangle\langle U_m\rangle\langle U_i U_j U_n\rangle + \langle U_l\rangle\langle U_n\rangle\langle U_i U_j U_m\rangle \\ &\quad + \langle U_m\rangle\langle U_n\rangle\langle U_i U_j U_l\rangle - \langle U_i U_j\rangle\langle U_l\rangle\langle U_m\rangle\langle U_n\rangle - \langle U_i U_l\rangle\langle U_j\rangle\langle U_m\rangle\langle U_n\rangle \\ &\quad - \langle U_i U_m\rangle\langle U_j\rangle\langle U_l\rangle\langle U_n\rangle - \langle U_i U_n\rangle\langle U_j\rangle\langle U_l\rangle\langle U_m\rangle - \langle U_j U_l\rangle\langle U_i\rangle\langle U_m\rangle\langle U_n\rangle \\ &\quad - \langle U_j U_m\rangle\langle U_i\rangle\langle U_l\rangle\langle U_n\rangle - \langle U_j U_n\rangle\langle U_i\rangle\langle U_l\rangle\langle U_m\rangle - \langle U_l U_m\rangle\langle U_i\rangle\langle U_j\rangle\langle U_n\rangle \\ &\quad - \langle U_l U_n\rangle\langle U_i\rangle\langle U_j\rangle\langle U_m\rangle - \langle U_m U_n\rangle\langle U_i\rangle\langle U_j\rangle\langle U_l\rangle \\ &\quad + 4\langle U_i\rangle\langle U_j\rangle\langle U_l\rangle\langle U_m\rangle\langle U_n\rangle. \end{aligned} \tag{A.4}$$

Appendix B

Transport Equations of Velocity Moments

Transport equations for the Reynolds stresses are given by:

$$\frac{\partial \langle u_i u_j \rangle}{\partial t} + C_{ij} = P_{ij} + T_{ij} + \Pi_{ij} + \varepsilon_{ij} + D_{ij} \tag{B.1}$$

where the budget terms

$$\begin{aligned}
C_{ij} &= \langle U_k \rangle \frac{\partial \langle u_i u_j \rangle}{\partial x_k}, \\
P_{ij} &= -\langle u_i u_k \rangle \frac{\partial \langle U_j \rangle}{\partial x_k} - \langle u_j u_k \rangle \frac{\partial \langle U_i \rangle}{\partial x_k} \\
T_{ij} &= -\frac{\partial \langle u_i u_j u_k \rangle}{\partial x_k} \\
\Pi_{ij} &= -\frac{1}{\rho} \left(\left\langle u_i \frac{\partial p}{\partial x_j} \right\rangle + \left\langle u_j \frac{\partial p}{\partial x_i} \right\rangle \right) \\
\varepsilon_{ij} &= -2\nu \left\langle \frac{\partial u_i}{\partial x_k} \frac{\partial u_j}{\partial x_k} \right\rangle \\
D_{ij} &= \nu \frac{\partial^2 \langle u_i u_j \rangle}{\partial x_k \partial x_k}
\end{aligned}$$

are known as convection, production, turbulent diffusion, velocity/pressure-gradient, viscous dissipation and viscous (molecular) diffusion terms. For a statistically stationary flow, the time-derivative term is equal to zero. In the direction of homogeneous flow, derivatives of mean values are zero, i.e. $\partial \langle . \rangle / \partial z = 0$.

Transport equations of third-order moments are given by:

$$\frac{\partial \langle u_i u_j u_l \rangle}{\partial t} + C_{ijl} = P_{ijl}^{(S)} + P_{ijl}^{(T)} + T_{ijl} + \Pi_{ijl} + \varepsilon_{ijl} + D_{ijl} \tag{B.2}$$

where

$$\begin{aligned}
C_{ijl} &= \langle U_k \rangle \frac{\partial \langle u_i u_j u_l \rangle}{\partial x_k}, \\
P_{ijl}^{(S)} &= -\langle u_i u_j u_k \rangle \frac{\partial \langle U_l \rangle}{\partial x_k} - \langle u_i u_l u_k \rangle \frac{\partial \langle U_j \rangle}{\partial x_k} - \langle u_j u_l u_k \rangle \frac{\partial \langle U_i \rangle}{\partial x_k} \\
P_{ijl}^{(T)} &= \langle u_i u_j \rangle \frac{\partial \langle u_l u_k \rangle}{\partial x_k} + \langle u_i u_l \rangle \frac{\partial \langle u_j u_k \rangle}{\partial x_k} + \langle u_j u_l \rangle \frac{\partial \langle u_i u_k \rangle}{\partial x_k} \\
T_{ijl} &= -\frac{\partial \langle u_i u_j u_l u_k \rangle}{\partial x_k} \\
\Pi_{ijl} &= -\frac{1}{\rho} \left(\left\langle u_i u_j \frac{\partial p}{\partial x_l} \right\rangle + \left\langle u_i u_l \frac{\partial p}{\partial x_j} \right\rangle + \left\langle u_j u_l \frac{\partial p}{\partial x_i} \right\rangle \right) \\
\varepsilon_{ijl} &= -2\nu \left(\left\langle u_i \frac{\partial u_j}{\partial x_k} \frac{\partial u_l}{\partial x_k} \right\rangle + \left\langle u_j \frac{\partial u_i}{\partial x_k} \frac{\partial u_l}{\partial x_k} \right\rangle + \left\langle u_l \frac{\partial u_i}{\partial x_k} \frac{\partial u_j}{\partial x_k} \right\rangle \right) \\
D_{ijl} &= \nu \frac{\partial^2 \langle u_i u_j u_l \rangle}{\partial x_k \partial x_k}.
\end{aligned}$$

Transport equations of fourth-order moments are given by:

$$\frac{\partial\langle u_i u_j u_l u_m\rangle}{\partial t} + C_{ijlm} = P^{(S)}_{ijlm} + P^{(T)}_{ijlm} + T_{ijlm} + \Pi_{ijlm} + \varepsilon_{ijlm} + D_{ijlm} \tag{B.3}$$

where

$$\begin{aligned}
C_{ijlm} =& \langle U_k\rangle \frac{\partial\langle u_i u_j u_l u_m\rangle}{\partial x_k},\\
P^{(S)}_{ijlm} =& -\langle u_i u_j u_l u_k\rangle \frac{\partial\langle U_m\rangle}{\partial x_k} - \langle u_j u_l u_m u_k\rangle \frac{\partial\langle U_i\rangle}{\partial x_k} - \langle u_i u_l u_m u_k\rangle \frac{\partial\langle U_j\rangle}{\partial x_k}\\
& - \langle u_i u_j u_m u_k\rangle \frac{\partial\langle U_l\rangle}{\partial x_k}\\
P^{(T)}_{ijlm} =& \langle u_i u_j u_l\rangle \frac{\partial\langle u_m u_k\rangle}{\partial x_k} + \langle u_j u_l u_m\rangle \frac{\partial\langle u_i u_k\rangle}{\partial x_k} + \langle u_i u_l u_m\rangle \frac{\partial\langle u_j u_k\rangle}{\partial x_k}\\
& + \langle u_i u_j u_m\rangle \frac{\partial\langle u_l u_k\rangle}{\partial x_k}\\
T_{ijlm} =& -\frac{\partial\langle u_i u_j u_l u_m u_k\rangle}{\partial x_k}\\
\Pi_{ijlm} =& -\frac{1}{\rho}\left(\left\langle u_i u_j u_l \frac{\partial p}{\partial x_m}\right\rangle + \left\langle u_j u_l u_m \frac{\partial p}{\partial x_i}\right\rangle + \left\langle u_i u_l u_m \frac{\partial p}{\partial x_j}\right\rangle\right.\\
& \left. + \left\langle u_i u_j u_m \frac{\partial p}{\partial x_l}\right\rangle\right)\\
\varepsilon_{ijlm} =& -2\nu\left(\left\langle u_i u_j \frac{\partial u_l}{\partial x_k}\frac{\partial u_m}{\partial x_k}\right\rangle + \left\langle u_j u_l \frac{\partial u_i}{\partial x_k}\frac{\partial u_m}{\partial x_k}\right\rangle + \left\langle u_l u_m \frac{\partial u_i}{\partial x_k}\frac{\partial u_j}{\partial x_k}\right\rangle\right.\\
& + \left\langle u_i u_m \frac{\partial u_j}{\partial x_k}\frac{\partial u_l}{\partial x_k}\right\rangle \left\langle u_i u_l \frac{\partial u_j}{\partial x_k}\frac{\partial u_m}{\partial x_k}\right\rangle + \left\langle u_j u_m \frac{\partial u_i}{\partial x_k}\frac{\partial u_l}{\partial x_k}\right\rangle\Bigg)\\
D_{ijlm} =& \nu\frac{\partial^2\langle u_i u_j u_l u_m\rangle}{\partial x_k \partial x_k}.
\end{aligned}$$

As mentioned before, for a statistically stationary flow, the time-derivative term is equal to zero. In the direction of homogeneous flow, derivatives of mean values are zero, i.e. $\partial\langle . \rangle/\partial z = 0$

Appendix C

Approximation of Fifth-Order Moments

In Gram-Charlier series expansions, a non-Gaussian probability density function is given in the form of a series of Hermite polynomials for two variables with respect to the Gaussian distribution. By truncating the series expansion to the fourth order, the following expressions for fifth-order velocity moments are obtained:

$$\langle u_i^5 \rangle = 10 \langle u_i^2 \rangle \langle u_i^3 \rangle, \tag{C.1}$$

$$\langle u_i^4 u_j \rangle = 6 \langle u_i^2 \rangle \langle u_i^2 u_j \rangle + 4 \langle u_i^3 \rangle \langle u_i u_j \rangle, \tag{C.2}$$

$$\langle u_i^2 u_j^3 \rangle = 6 \langle u_i u_j \rangle \langle u_i u_j^2 \rangle + \langle u_i^2 \rangle \langle u_j^3 \rangle + 3 \langle u_i^2 u_j \rangle \langle u_j^2 \rangle. \tag{C.3}$$

Currently, only models of fifth-order velocity moments with up to two variables (Equations. (C.1)-(C.3)) have been developed. However, these should be enough for modeling dissipation processes and velocity/pressure-gradient correlations in transport equations for planar flows.